CR 128658

REPORT NO. GDCA-DDB72-005
CONTRACT NAS 9-11992

OPTIMIZATION OF THERMAL PROTECTION SYSTEMS FOR THE SPACE SHUTTLE VEHICLE

VOLUME I • FINAL REPORT

GENERAL DYNAMICS
Convair Aerospace Division

148 pp

REPORT NO. GDCA-DDB72-005

OPTIMIZATION OF THERMAL PROTECTION SYSTEMS FOR THE SPACE SHUTTLE VEHICLE

VOLUME I ✦ FINAL REPORT

30 October 1972

Prepared Under
Contract NAS9-11992

Submitted to
National Aeronautics and Space Administration
MANNED SPACECRAFT CENTER
Houston, Texas

Prepared by
CONVAIR AEROSPACE DIVISION OF GENERAL DYNAMICS
San Diego, California

C

FOREWORD

This investigation was performed for the NASA Manned Spacecraft Center's Structures and Mechanics Division. Dr. Donald M. Curry was the technical monitor, and Dr. Kenton D. Whitehead was the project manager. The study was conducted by a project team consisting of Drs. K. T. Shih, A. Gay, and O. Brevig, and Mr. R. C. Day - Thermodynamics, Messrs. R. S. Wilson and P. T. Thorndyke - Stress, S. T. Hitchcock - Weights, and T. C. Johnson - Costs. Programming and computer coordination was performed by Ms. E. R. Neuharth. All work was done at the San Diego Operation of the Convair Aerospace division of General Dynamics. Results of the study are published in two volumes: the Final Report (Volume I) and the User's Manual (Volume II).

TABLE OF CONTENTS

LIST OF FIGURES

LIST OF FIGURES, Contd

LIST OF FIGURES, Contd

LIST OF TABLES

LIST OF TABLES, Contd

SUMMARY

A study was performed to continue development of computational techniques initiated under Contract NAS9-10956, "Computational Techniques for Design Optimization of Thermal Protection Systems for the Space Shuttle Vehicle," to be used in the studies for the Space Shuttle Thermal Protection System. The resulting computer code was then used to perform some additional optimization studies on several TPS configurations. The program was developed in Fortran IV for the CDC 6400, and it was converted to Fortran V to be used for the Univac 1108. Documentation of the study consists of the user's manual and the final report.

The computational methodology is developed in modular fashion to facilitate changes and updating of the techniques and to allow overlaying the computer code to fit into approximately 131,000 octal words of core storage. The program logic involves subroutines which handle input and output of information between computer and user, thermodynamic, stress, dynamic, and weight/estimate analyses of a variety of panel configurations. These include metallic, ablative, RSI (with and without an underlying phase change material), and a thermodynamic analysis only of carbon-carbon systems applied to the leading edge and flat cover panels. Two different thermodynamic analyses are used. The first is a two-dimensional, explicit procedure with variable time steps which is used to describe the behavior of metallic and carbon-carbon leading edges. The second is a one-dimensional implicit technique used to predict temperature in the charring ablator and the non-charring RSI. The latter analysis is performed simply by suppressing the chemical reactions and pyrolysis of the TPS material.

Two types of stress analysis are also performed. A discrete element technique describes all of the configurations (with the exception of the carbon-carbon leading edge) and a more rigorous finite element analysis is used to solve the case for the large deflections of the RSI and its accompanying glue line. A dynamic routine predicts not only the noise excitation due to a number of external sources and the fatigue life of a number of simple panels but also a panel flutter analyses for the same simplified configuration. The weights of all configurations were determined by a unique new method in which total system weight per unit area is determined as the sum of the weights of component parts. Two cost analyses are provided: in the first, manufacturing costs are prescribed as the sum of the costs needed to fabricate and assemble all of the component parts utilized in the weight model. In the second technique, the total program costs are predicted based on historical data for simpler systems.

Two basic types of input data are provided based on trajectory data: the first includes vehicle attitude from which aerodynamic heating rates and pressures are predicted. In the other heating rates and pressures are given as a function of time. The former

values are given in both hot wall and cold wall terms as options for the ablation routine. Standard program output includes heating rates, temperature, and stresses for discrete elements of the TPS analyzed as well as dynamic stresses and the panel weight and cost.

Optimization and sensitivity studies are performed by the user by varying panel size, material properties, and configuration in a series of computer runs. The program sizes panel and insulation thicknesses. An optimum design is then identified as the one giving either minimum weight or cost as a function of the parameters being varied for the investigation. Sensitivity studies are performed by noting the change in system weight or cost due to the variation in some independent variable such as trajectory or heating prediction method for an optimum panel configuration.

SECTION 1

INTRODUCTION

The study performed under this contract was a follow-on to that accomplished on Contract NAS9-10956, "Computational Techniques for Design Optimization of Thermal Protection Systems for the Space Shuttle Vehicle." The output of the former study was a computer program which sizes a number of different configurations of metallic re-radiative thermal protection system (TPS) panels and supports to stipulated constraints of stress values, sub-structure allowable temperatures, and acoustic fatigue, among others. The development methodology is reported in Reference 1, and the detailed program description and user's instructions in Reference 2.

As a result of the continuing space shuttle systems studies pursued by NASA and Aerospace Industry Contractors, the interest in metallic re-radiative TPS waned, and was replaced by concepts employing carbon-carbon, Reusable Surface Insulation (RSI), or charring ablators. The follow-on study concentrated on these latter concepts, and also included study and implementation of improvements to the basic computer program to reduce computational time and to incorporate the latest aerothermodynamic methods recommended by the Thermo Panel of the Space Shuttle Aerothermodynamic/ Configurations Working Group, noted in Reference 16.

Portions of the development of the analytic methods, equations and data banks were generated under Company sponsored activities. These were made available to be programmed and incorporated into the TPS computer program. The results are included in this report because of their applicability and interest to NASA.

The study was performed in a series of related tasks. These investigations included: (1) the improvement of existing analyses already developed for metallic thermal protection system cover panels and the development of four subroutines for treating passive and active TPS's, including carbon-carbon composites, RSI, charring ablators, and a heat sink substrate using phase change material (PCM), (2) computer program applications which include both short term improvements to speed the computer use and improve its efficiency as well as investigations to assess the desirability of incorporating formalized optimization procedures into the system sizing routines, (3) performance of preliminary optimization and sensitivity studies to demonstrate use of the techniques, and (4) the documentation of the results of the studies and the improved computer program.

SECTION 2

COMPUTER PROGRAM REFINEMENTS

The prediction methods and analyses developed for use in the TPS sizing computer program as part of this year's effort are described and discussed in this section. The complete computer program, including those sections developed under last year's effort which remain unchanged, is presented in a companion volume entitled "User's Manual" which contains the listing and operating instructions.

2.1 MATHEMATICAL AND NUMERICAL METHODS

2.1.1 THERMODYNAMIC ANALYSIS. For the case of the metallic cover panel, heat transfer is determined two-dimensionally. The temperature at any point in the structure is a function of external and internal convection and radiation rates and the conductivity and thermal inertia properties of the structure itself. In this program, structural temperature distributions are evaluated through use of the lumped parameter method of finite differences.

The surface and/or structure is divided into an arbitrary number of small segments. The segments are arranged in rows parallel and columns perpendicular to the surface as shown in Figure 2-1.

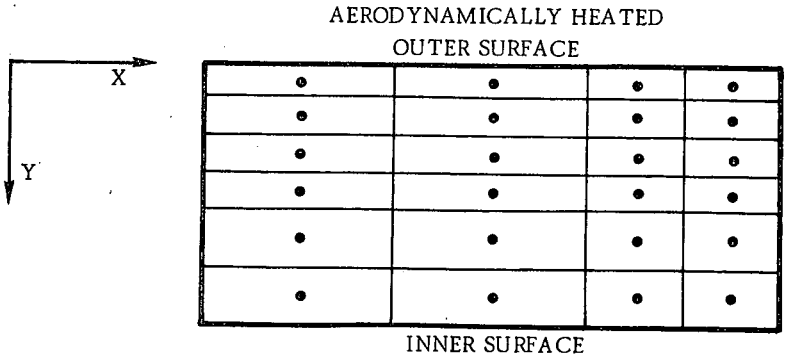

Figure 2-1. Surface/Structure Segmentation

Then, for some small time increment (Δt), the net heat flux to each surface segment is determined. For a segment i, then, the temperature change from time to time, $t + \Delta t$, is

$$T_i(t+\Delta t) - T_i(t) = \left[q_{net} A_{BL} - (qA)_{INSD} - \Sigma \left(kA \frac{\Delta T}{X}\right)_N - \Sigma (q_{rad} A)_N \right] \frac{\Delta t}{(WC_p)_i} \quad (2\text{-}1)$$

where

A_N = area perpendicular to direction N

k_N = effective thermal conductivity in direction N

X_N = length of conduction path in direction N

ΔT_N = temperature difference between adjacent elements in direction N at time t

q_{rad} = heat transfer by radiation between nodes

W = weight of element i

C_p = specific heat of element i

It is assumed that all the mass is concentrated in a point at the centroid of the segment, A_N is equal to the segment interface area, and X_N is equal to the distance between centroids in direction N.

The net heat transfer is given by

$$q_{net} = q_{cons}\, q_i - q_{rad} \qquad (2\text{-}2)$$

where q_i is the boundary layer convective heat transfer rate, q_{rad} represents the energy loss due to surface radiation, and q_{cons} is an optional multiplying factor. This factor may be used to approximately allow for the effects of shock wave interactions, flow divergence, etc.

The term $(qA)_{INSD}$ provides an optional capacity to include internal convective cooling of the structure. The cooling occurs on the backface of the last segment.

Terms in Equation 2-1 which do not apply to a given element are dropped out for that element. Thus, the q_{net} applies only to elements of the first row, i.e., those representing the surface, and the $(qA)_{INSD}$ term applies only to elements of the last row, i.e., those representing the backface. Internal radiation heat transfer is also taken into account in this program. The accuracy of Equation 2-1 is dependent upon the size of the segments and the computation interval and improves as these parameters are decreased. The program may be used for either one-dimensional or two-dimensional arrays of segments.

In the following, the two-dimensional case is discussed; the one-dimensional problem is treated as a special case of a single column. The structure is set up in a matrix shown in Figure 2-2. The material may not be homogeneous in either the x-direction or the y-direction. The maximum number of rows and columns is nine each. Configurations

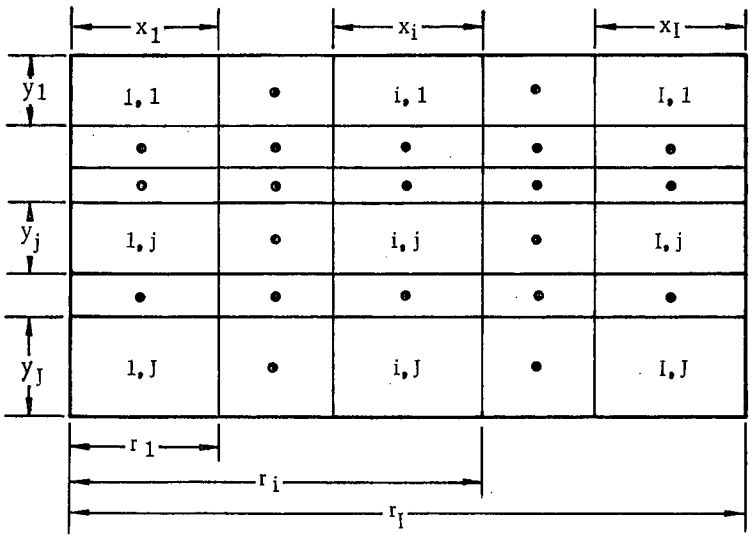

(a) STRUCTURE ARRAY

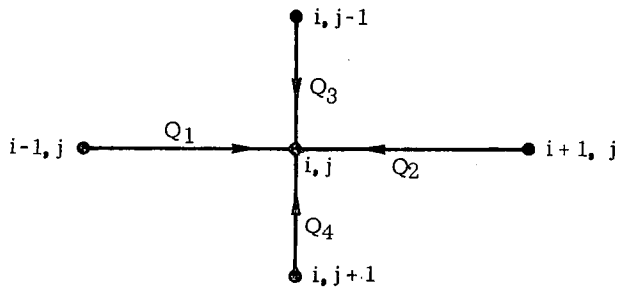

(b) TYPICAL NODES

Figure 2-2. Structure Heat Transfer Matrix

are given in Figure 2-3, and nodal breakdowns for the thermodynamic and stress analyses are given in Figure 2-4.

The temperature at any segment at time $t + \Delta t$ is dependent upon the summation of direction heat transfer rates at time t. The general equation is given by Equation 2-1. From Figure 2-2, for a typical node, the temperature, T, changes from time t to $t + \Delta t$ by

$$T_{ij}\,(t + \Delta t) = T_{ij}\,(t) + \frac{\Delta t}{A_{ij}} \sum_{k=1}^{4} Q_K \qquad (2\text{-}3)$$

A_{ij} is the thermal mass of the node as defined in Table 2-1, together with other parameters. The equations for computing Q_K's are listed in the following:

a. Conduction heat transfer

$$Q_1 = (T_{i-1,\,j} - T_{i,\,j}) / E_{i-1,\,j} \qquad (2\text{-}4)$$

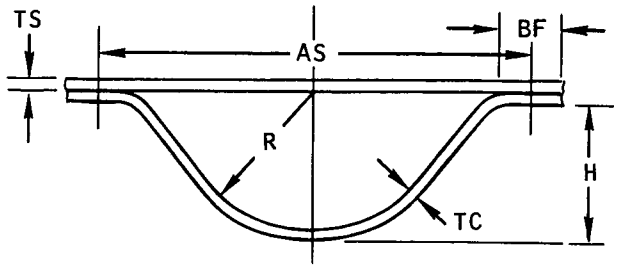

1. CONVAIR TRAPEZOIDAL

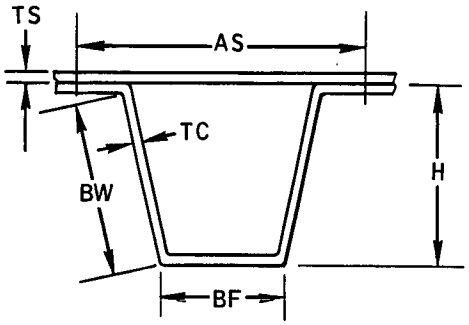

2. FLAT CORRUGATION WITH SKIN

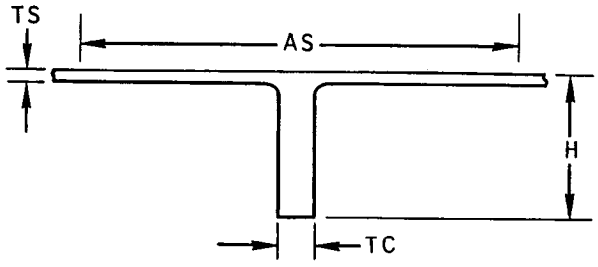

3. RIB-STIFFENED PANEL

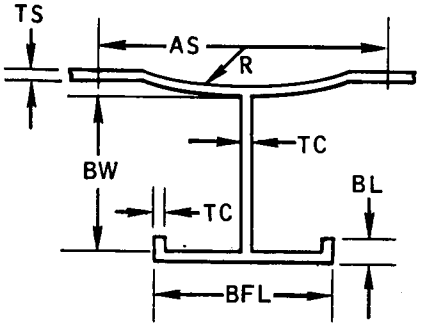

4. SKIN-STRINGER

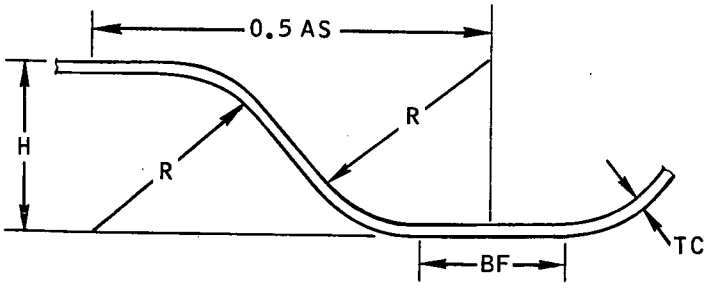

5. OPEN CORRUGATION

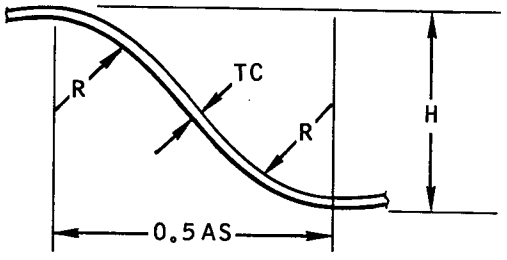

6. OPEN CORRUGATION
(CIRCULAR ARC CORRUGATION)

Figure 2-3. Panel Geometries

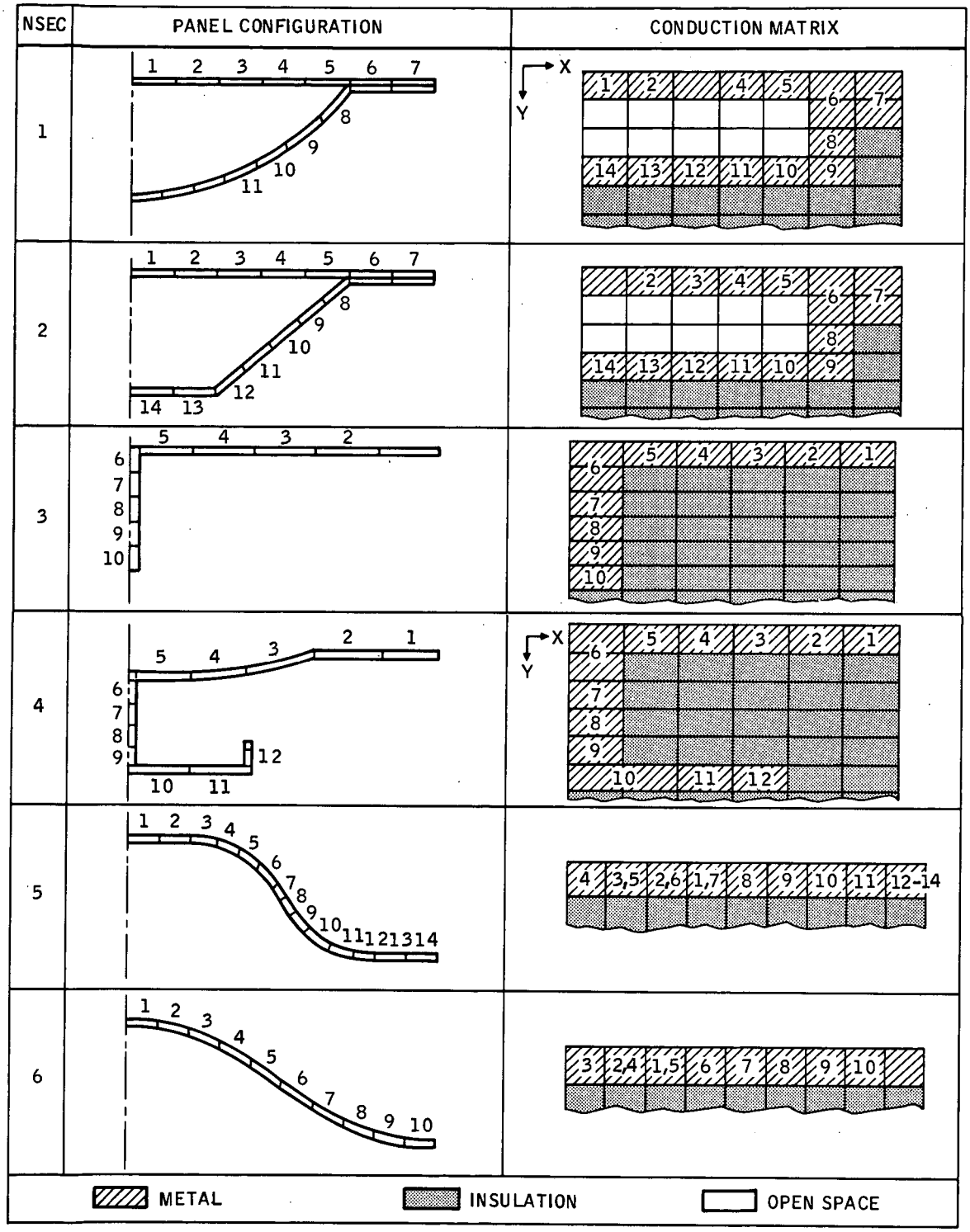

Figure 2-4. Configurations for Thermodynamic and Stress Analysis

Table 2-1. Notations for Heat Transfer Calculations

Symbol	Calculated Term	Symbol	Calculated Term
x'_i	x_i	$C_{i,j}$	$y_j/(2K_{i,j}x_i)$
$y'_{i,j}$	y_j	$D_{i,j}$	-
$A_{i,j}$	$(\rho c_p)_{i,j}\, x'_j\, y_j$	$E_{i,j}$	$B_{i,j} + B_{i+1,j}$
$B_{i,j}$	$x'_i/(2K_{i,j}y_j)$	$F_{i,j}$	$C_{i,j} + C_{i,j+1}$

$$Q_2 = (T_{i+1,j} - T_{ij})/E_{i,j} \tag{2-5}$$

$$Q_3 = (T_{i,j-1} - T_{ij})/F_{i,j-1} \tag{2-6}$$

$$Q_4 = (T_{i,j+1} - T_{i,j})/F_{i,j} \tag{2-7}$$

b. Radiation heat transfer

$$Q_K = \sigma \Sigma L\, \Im_{a,b}\, (T^4_{m,n} - T^4_{i,j}) \tag{2-8}$$

where

$L = x'_i$ (for $k = 3, 4$)

$= y'_{ij}$ (for $k = 1, 2$)

c. Nodes on the first column

$$Q_1 = 0$$

d. Nodes on the last column

$$Q_2 = 0$$

e. Nodes on the first row

$$Q_3 = x'_i\, q_{net_i}$$

f. Nodes on the last row

$$Q_4 = h_{ins}\, x'_i\, (T_{ins} - T_{ij})$$

One particular improvement which was made to the heat transfer calculations of the metallic TPS's was the adoption of a time step variation. Since the numerical technique for solution is explicit, small time steps must be taken at various times during the trajectory to avoid numerical instability. However, at other times, conditions are changing so slowly that small time step sizes are prohibitively expensive. The temperatures of each node are now monitored throughout the calculations, and when it is determined the largest temperature change is small, the time step size is lengthened still however being maintained within a theoretically established stability criterion. The converse is also true. When temperatures change rapidly, the step size is decreased. Such variations lead to a 39% savings in computer time with no noticeable loss of temperature accuracy.

For the case of the thermodynamic analysis of the ablator and RSI TPS's, the one-dimensional heat transfer computations are performed by an implicit technique which avoids the difficulties of numerical instability. Since this technique was adopted almost in total from an existing computer program, the reader is referred to the original reference by Curry for details (Ref. 3).

2.1.2 STRUCTURAL ANALYSIS. During early stages of the contract, a separate structural analysis was performed on the supporting heat posts which attach the simply supported cover panels to the primary structure of the space shuttle vehicle. Results of a parametric study of various loading conditions described below, demonstrated that for the flexural rigidity established by acoustic test, the design point for this part of the structure is minimum gauge. Hence, for the remainder of the effort, these values were used.

Analyses of Supporting Structure

Sizing of the tubular supports for both static and dynamic loads of the existing metallic TPS support configurations is not performed by Program P5490. However, an existing computer subroutine was adapted to conduct this analysis. As is the case for the TPS panel, the posts are sized for both static strength for aerodynamic loads and dynamic response due to the acoustic environment. The vibrations induced by the engines, which are transmitted mechanically through the shuttle structure, are omitted in the analysis because the excitations are attenuated rapidly except in the immediate area of the thrust structure. The dynamic response of the post, however, to the acoustic environment is important because it has been demonstrated at Convair Aerospace in the design of TPS supports that the dynamic stress can be a critical item (Reference 4).

The design requirements applied to this analysis are:

1. The applied ultimate 3-σ stress on the tube wall must not exceed a specified cut-off value (examples are 78,000 psi for TDNiCr and 120,000 psi for titanium).

2. The applied 3-σ stress must not exceed the crippling stress of the tube walls.

3. The applied limit 1-σ stress must not exceed the allowable fatigue stress determined from the random S-N fatigue curve for an input required panel life.

4. The post must have a critical column buckling load greater than the applied ultimate axial load acting alone.

5. The post wall thickness must be greater than input minimum gauges.

The input data to this particular post sizing analysis includes

post length
weight of the dynamic forcing function
pressure force
ultimate factor
S - the sigma factor
K - buckling constant
vibration environment (power spectral density as a function of frequency)
S-N data for the post material

The heat shield support posts are represented as a single degree of freedom system whose natural frequency is idealized as that of a massless uniform cantilever beam with a concentrated mass at the free end (Figure 2-5). The loads on the post include an applied axial load P and a lateral load Q_{rms}. The former is due to the differential pressure between the external aerodynamic load and the internal pressure behind the TPS. The applied lateral load W (transferred to the TPS panel and post by the acoustic environment) is a function of panel weight subject to a specified rms acceleration at the system's fundamental frequency

$$f_n = \frac{1}{2\pi} \sqrt{(1158\ EI)/(L^3 W)} \qquad (2\text{-}9)$$

A power spectral density curve specified to describe the environment (a typical one is illustrated in Figure 2-6) then gives the rms acceleration as

$$g_{rms} = \sqrt{\frac{\pi}{4} f_n \frac{S_n}{\zeta}} \qquad (2\text{-}10)$$

where

E = modulus of elasticity

I = moment of inertia

L = tube length

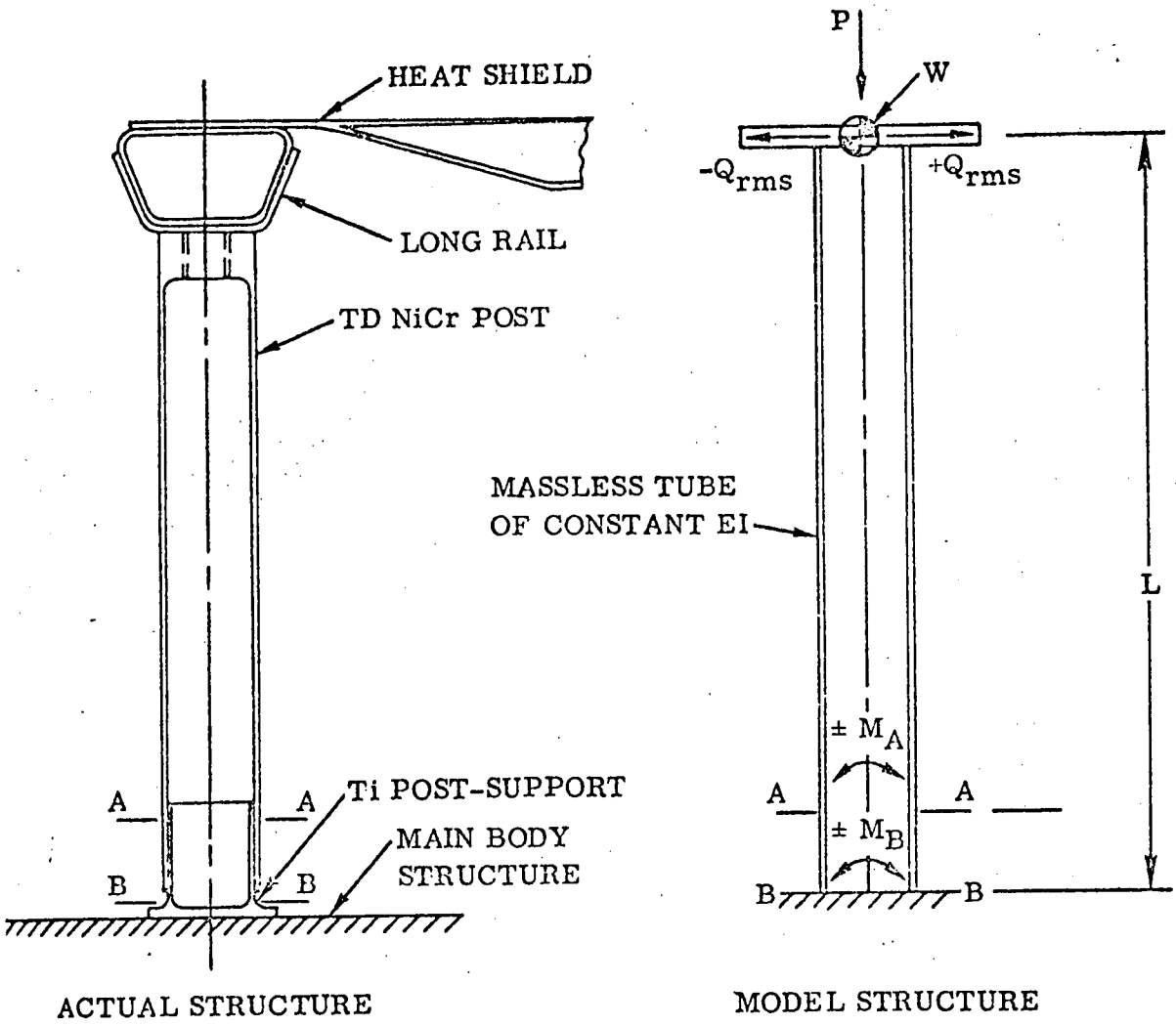

Figure 2-5. Support Post Structures

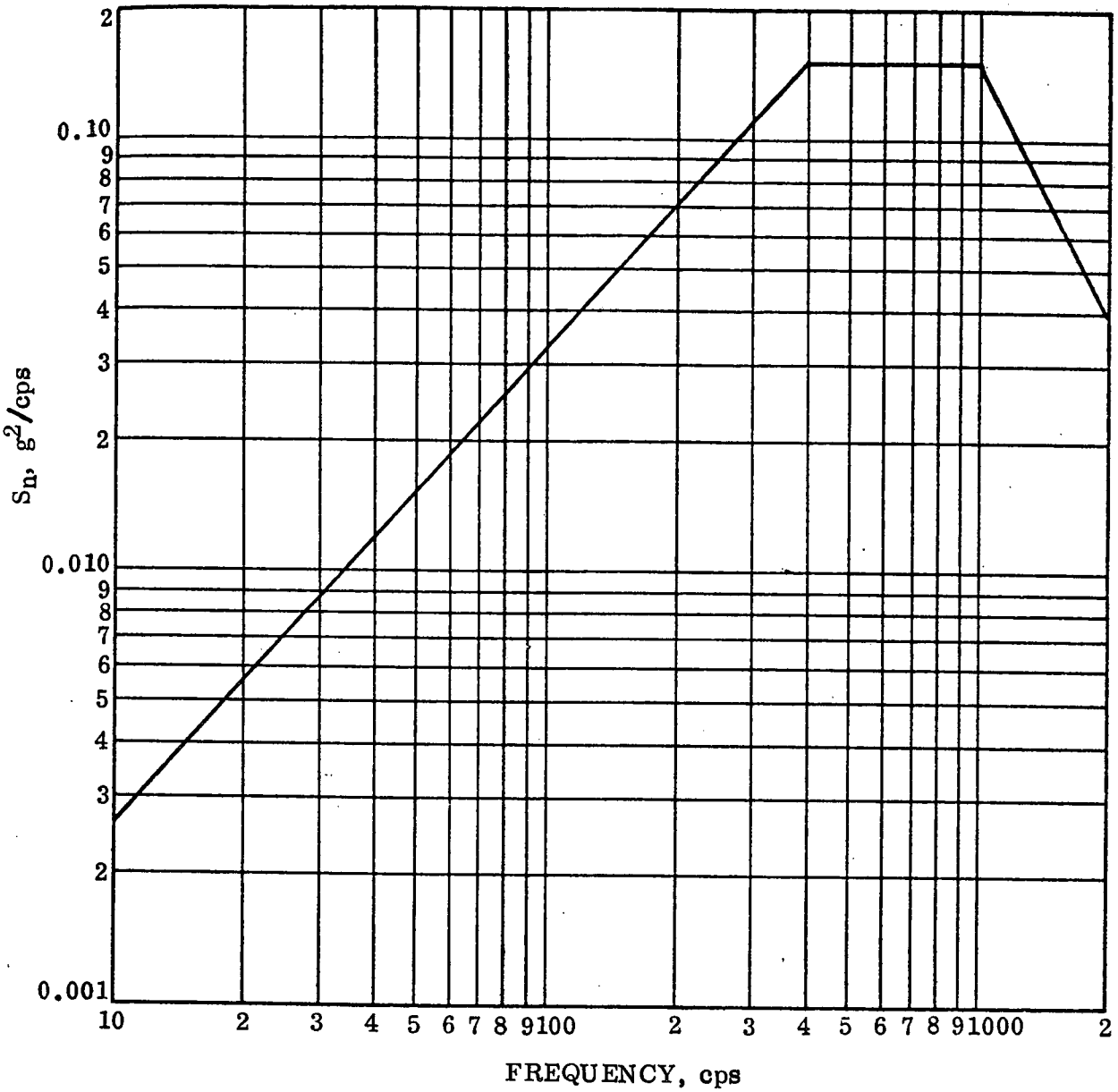

Figure 2-6. Typical Interface Liftoff Vibration Specification

S_n = amplitude of the power spectral density function in g^2/cps at the frequency f_n

ζ = damping ratio

The rms lateral load then becomes simply

$$Q_{rms} = \pm g_{rms} \cdot W \tag{2-11}$$

In order to size the uniform tubular post at its base, the rms bending moment is given by beam column analysis as

$$M = QJ \tan (L/J) \tag{2-12}$$

where

Q = lateral load

$J = \sqrt{(\eta EI)/(UF\ P)}$

η = plasticity correction factor

$$= \sqrt{\frac{1}{1 + \frac{3}{7} n \left(S_{max}/S_o\right)^{n-1}}} \tag{2-13}$$

n = slope of the plastic stress-strain curve

S_{max} = specified cut-off value for maximum stress

S_o = specified base stress

UF = ultimate factor (e.g., 1.4 to 1.5)

The maximum applied stress σ_{max} for the applied 3-σ stress is given by

$$\sigma_{max} = \frac{1}{Dt}\left[P + S\,\frac{4MD}{\pi D^3 t}\right] \tag{2-14}$$

where S = 3 for the 3-σ applied stress.

Thus Equations 2-12 and 2-14 are implicit in the plasticity correction factor. The performance of this calculation necessitates iteration. The 1-σ alternating stress to be used in the fatigue analysis is given simply by

$$\sigma_{alt} = \frac{8M\ D/2}{\pi D^3 t} \tag{2-15}$$

The allowable crippling stress is given by

$$F_{cr} = K \eta E (t/D) \tag{2-16}$$

where K = buckling constant, and the critical column load is given by the Euler equation, modified for plasticity

$$P_{cr} = \frac{C \pi^2 \eta EI}{L^2} \tag{2-17}$$

where C = fixity coefficient, which for a column fixed at one end and free at the other is 0.25.

The design requirement for the latter load is that the critical column load exceed the product of the applied axial load and the ultimate factor. For this particular analysis, the allowable random stress σ_{fat} corresponding to the 1-σ applied stress is computed from an allowable S-N curve (Figure 2-7 is an example) for the number of stress reversals given by

$$N = 4 N_F T f_n \tag{2-18}$$

where

N_F = number of flights

T = duration of the vibration environment per flight and the factor 4 is a factor of safety for fatigue life scatter.

The design factors corresponding to design requirements 1 through 5 are then computed as

Design Requirement	Design Factor
1	σ_{max}/S_{max}
2	σ_{max}/F_{cr}
3	$\sigma_{alt}/\sigma_{fat}$
4	$(UF\ P)/P_{cr}$
5	t_{mg}/t

where t_{mg} is the minimum gauge thickness, an input parameter.

The post design procedure of the existing computer program consists of iterating upon the post wall thickness t for a given tube diameter until the largest design factor is unity. All others must be less than unity, indicating that the applied load is less than the allowable, 1.

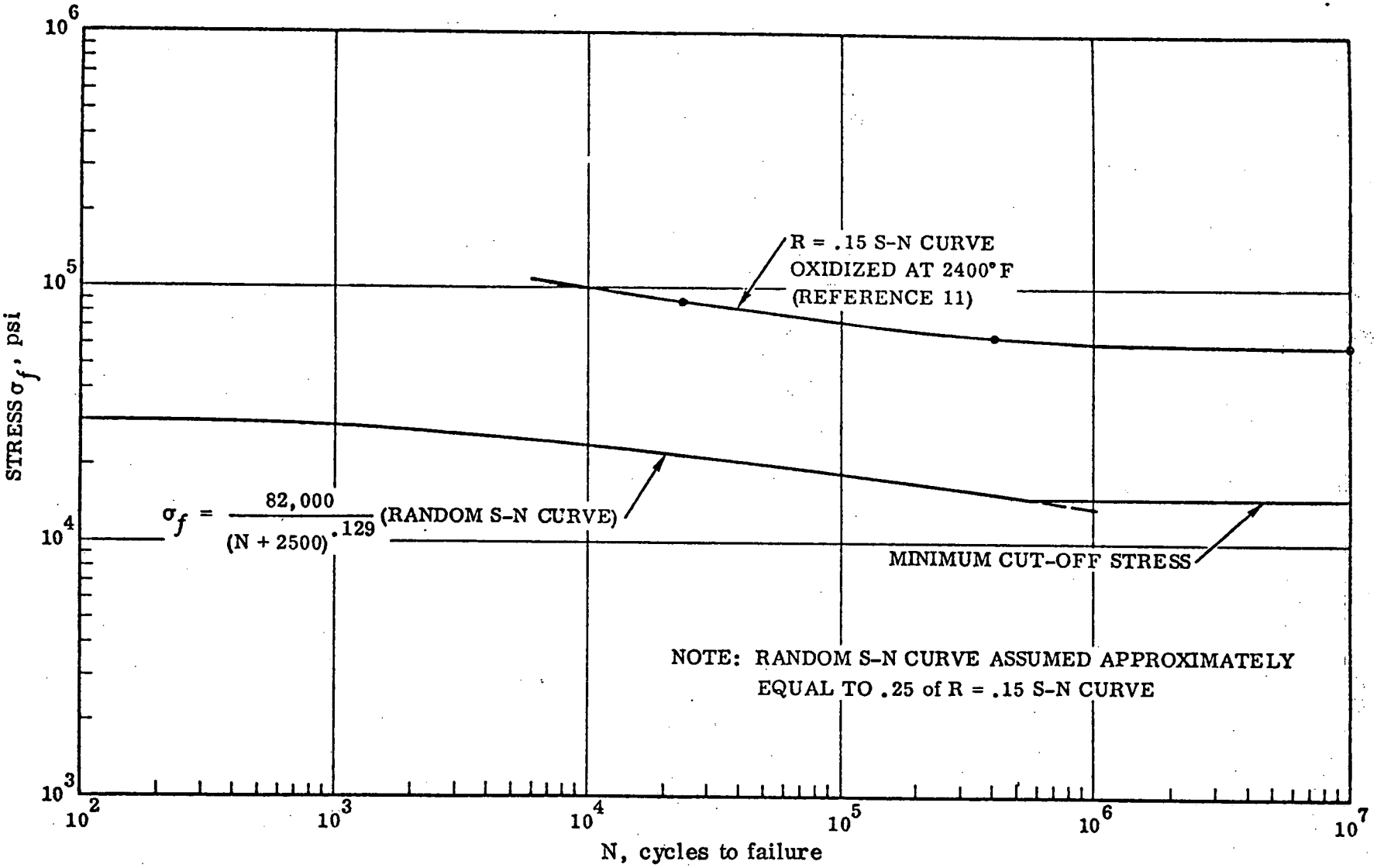

Figure 2-7. R = -1 and Random S-N Curves for TDNiCr

Results of studies conducted for TDNiCr posts

$W = 0.80$ lb (vibrating mass)

$\zeta = 0.125$ (damping ratio)

$P = 48$ lb (compressive axial load)

indicate that smaller post diameters yield lighter posts. This is shown by Figure 2-8. In addition, recent data developed at Convair have shown that this damping ratio may be low by an order of magnitude due to the frictional damping of this TPS of individual panels rubbing against each other. With this in mind, the entire system of cases represented in Figure 2-8 and a sensitivity study accompanying that investigation were re-run with a damping ratio of 10%. The results show that the design requirement in all cases run was minimum gauge; thus, the design philosophy of post supports alreay utilized in Contract NAS9-10956, to use minimum gauge posts, is confirmed.

2.1.3 DYNAMICS ANALYSIS, PANEL FLUTTER AND STABILITY. Panel flutter is a self-excited instability of elastic panels in supersonic flow, during which the panel oscillates in a direction normal to its plane at a constant amplitude; flutter usually results in fatigue damage to the panel. Considerable theoretical and experimental research has been conducted to understand the phenomenon and to develop design criteria to prevent it (Reference 5). The design approach recommended by Lemley is incorporated into the TPS sizing routine. The minimum panel thickness required to preclude panel flutter within the flight envelope is thereby established as a design constraint. Table 2-2 lists significant parameters that affect panel flutter.

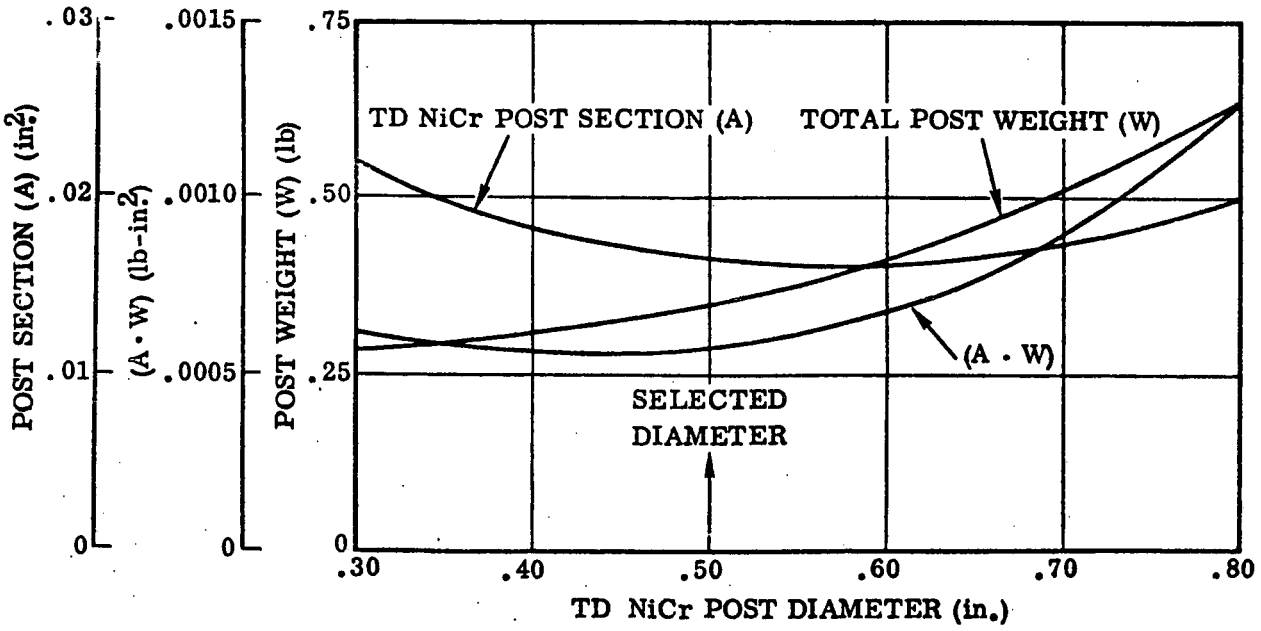

Figure 2-8. Post Section and Weight vs Post Diameter

Table 2-2. Parameters Affecting Flutter Speed

Flight Conditions	Physical Data and Geometry	Environmental Conditions
Mach no.	Young's modulus	Inplane Stress
Dynamic Pressure	Length	Differential Pressure
Angle-of-Attack	Width	Differential Temperature
Flow Angularity	Length-to-Width Ratio	
	Curvature	
	Cavity	
	Edge Conditions	
	Thickness (to be determined)	

The flutter analysis is performed using many computations already made in the sonic fatigue analysis. The stability limit for a flat panel is given in Figure 2-9 with the panel flutter parameter Φ plotted as a function of the panel length to width ratio. The curve is developed from experimental data (References 6 and 7). The function f(M) is given by Figure 2-10. The design occurs at the maximum value of q/f(M) for the given trajectory. Once this has been established, the computational procedure for establishing critical panel thickness is as follows:

1. Determine Φ for the panel length-to-width ratio from Figure 2-9.

2. Determine q from flow field calculations.

3. Determine f(M) from Figure 2-10.

4. Evaluate the panel modulus of elasticity E from the panel material property values at the design point temperature.

5. Compute the panel thickness t_B for flutter stability, where

$$\Phi = \left[\frac{f(M)E}{q}\right]^{1/3} \frac{t_B}{\ell} \qquad (2\text{-}19)$$

6. Compare this value t_B with the equivalent panel thickness already established in the fatigue analysis.

7. If t_B is less than the panel equivalent thickness, panel flutter presents no problem; if greater, the results are so noted in the fatigue analysis output, (Figure 2-11).

2.1.4 WEIGHTS/COST ANALYSIS

2.1.4.1 Parts Listing. The parts listing procedure requires that a library be maintained to call out an associated list of detailed parts when a given panel or structure configuration is specified. Each part has associated with it a list of manufacturing processes and amounts of material required to produce the part.

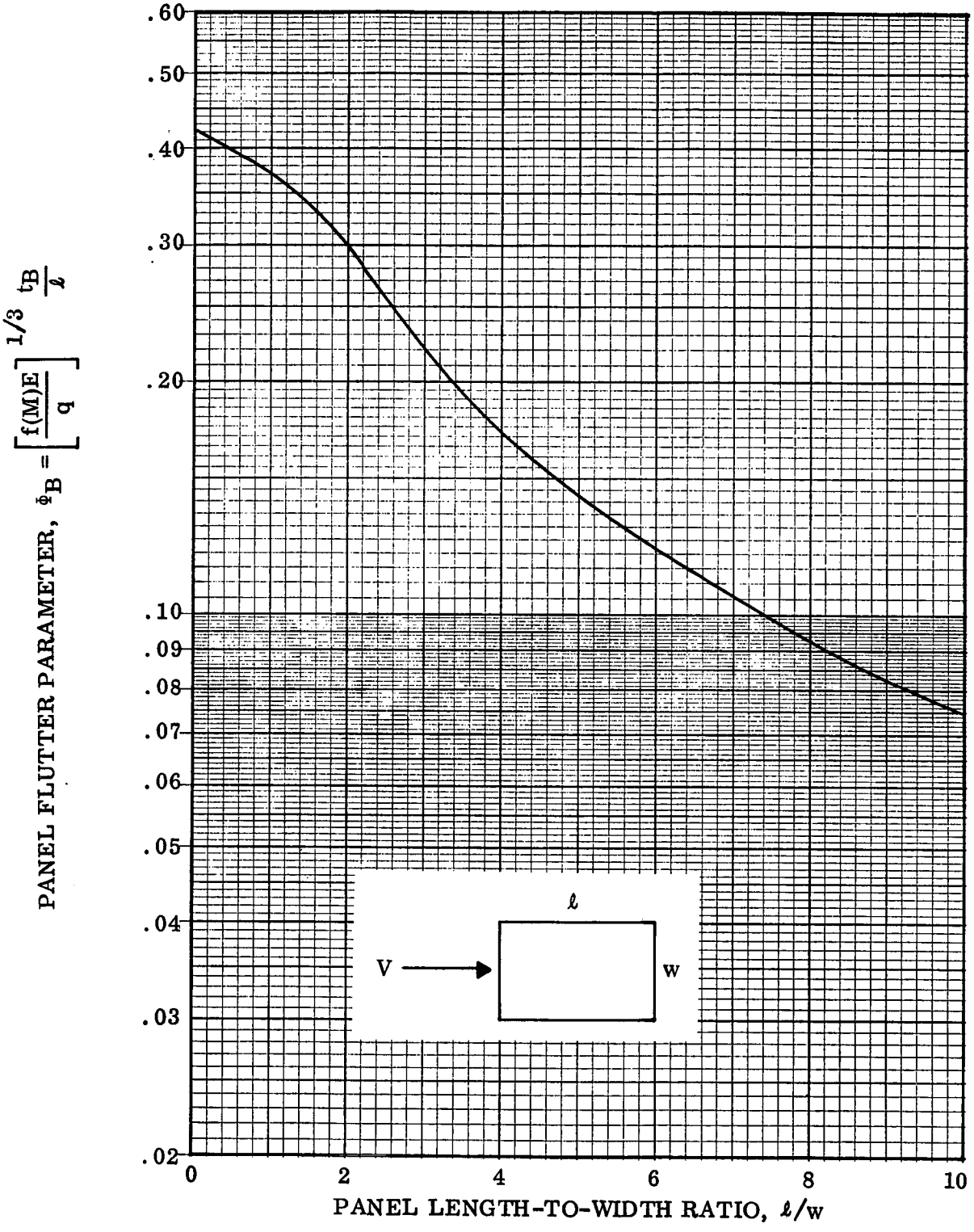

Figure 2-9. "Baseline" Design Curve

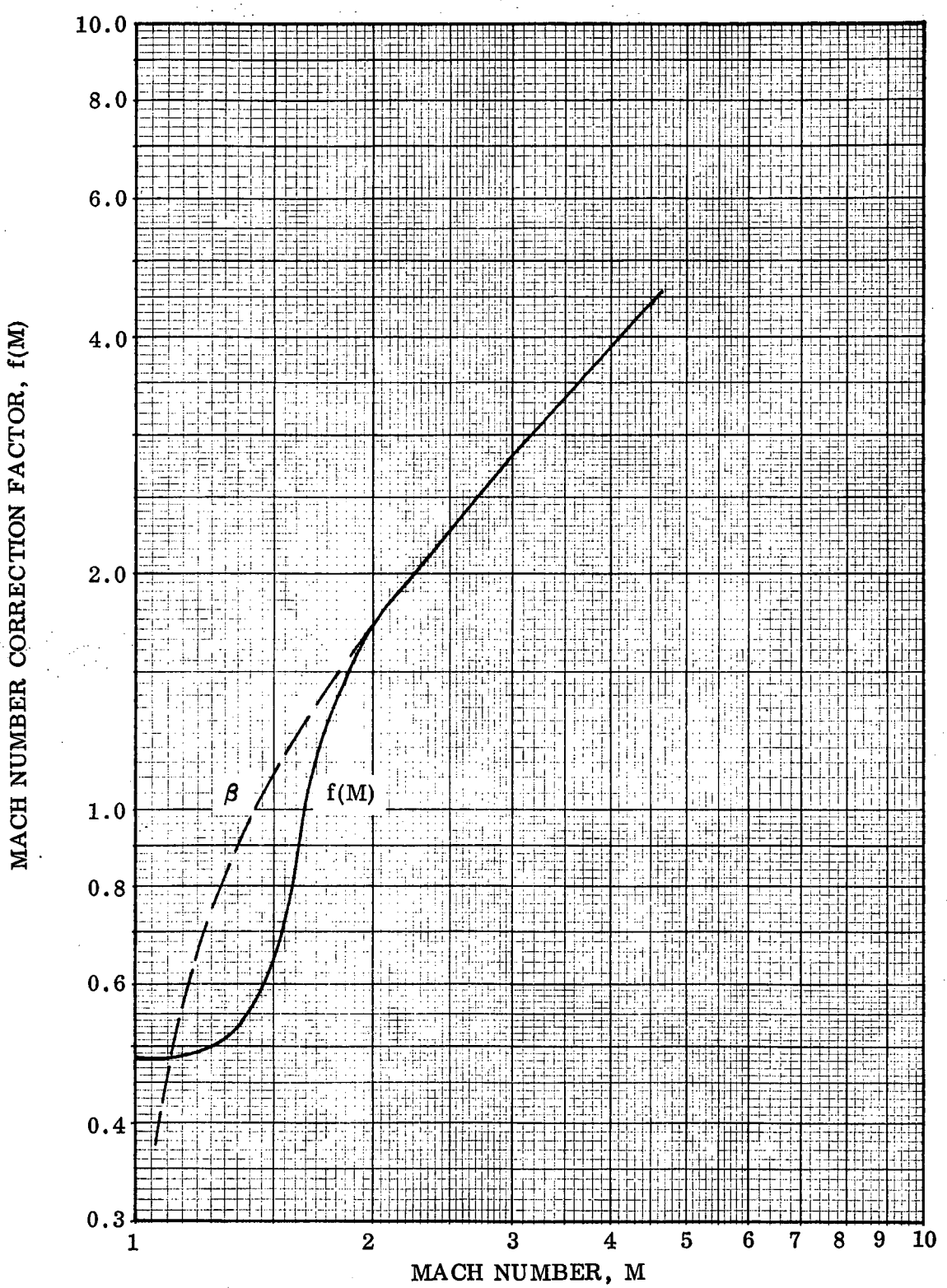

Figure 2-10. Mach Number Correction Factor Versus Mach Number

```
FREQUENCY =   527.9 HZ

BOUNDARY LAYER NOISE =  121.4 DB - REYNOLDS NO. =   2.4531E+08, MACH NO. =   1.5215E+00
DYNAMIC PRESSURE =   5.0738E+02, VELOCITY =   1.4423E+03
ROCKET ENGINE NOISE =  125.8 DB - APPARENT NOISE SOURCE AT   61.0 FT
ABES NOISE =   77.6 DB
JET SCRUBBING NOISE =  131.4 DB

MAXIMUM BENDING STRESS =        554 PSI
MAXIMUM RMS DEFLECTION =     .00001 IN
BOUNDARY LAYER NOISE CRITICAL STRESS =   3.1053E+01 PSI
NO. OF STRESS REVERSALS =   7.2451E+05
***PANEL IS GOOD FOR THIS CONDITION
   CRITICAL STRESS MAY BE INCREASED TO   3.3714E+04 PSI

MAXIMUM BENDING STRESS =        923 PSI
MAXIMUM RMS DEFLECTION =     .00001 IN
ROCKET ENGINE NOISE CRITICAL STRESS =   7.5678E+01 PSI
NO. OF STRESS REVERSALS =   1.9809E+05
***PANEL IS GOOD FOR THIS CONDITION
   CRITICAL STRESS MAY BE INCREASED TO   4.2595E+04 PSI

MAXIMUM BENDING STRESS =          4 PSI
MAXIMUM RMS DEFLECTION =     .00000 IN
JET FLYBACK ENGINE NOISE CRITICAL STRESS =   2.0902E-03 PSI
NO. OF STRESS REVERSALS =   1.3997E+07
***PANEL IS GOOD FOR THIS CONDITION
   CRITICAL STRESS MAY BE INCREASED TO   2.2849E+04 PSI

MAXIMUM BENDING STRESS =       1757 PSI
MAXIMUM RMS DEFLECTION =     .00002 IN
JET SCRUBBING NOISE CRITICAL STRESS =   2.2858E+02 PSI
NO. OF STRESS REVERSALS =   3.1217E+04
***PANEL IS GOOD FOR THIS CONDITION
   CRITICAL STRESS MAY BE INCREASED TO   5.9659E+04 PSI

COMPOSITE CRITICAL STRESS =   2.4278E+02 PSI
NO. OF STRESS REVERSALS =   1.8397E+05
***PANEL IS GOOD FOR THIS CONDITION
   CRITICAL STRESS MAY BE INCREASED TO   4.3179E+04 PSI

PANEL FLUTTER ANALYSIS - DESIGN POINT AT   7.4000E+01 SECONDS OF FLIGHT
YOUNGS MODULUS =   3.1600E+07, MACH NO. =   1.1923E+00
Q LOCAL/FCN(AMI) =   1.0045E+03, PHI =   4.0750E-01
***PANEL IS STABLE FOR FLUTTER
   PANEL EFFECTIVE THICKNESS =   2.2534E-01 IN.
   PANEL EFFECTIVE THICKNESS NECESSARY FOR FLUTTER STABILITY =   1.4852E-02 IN.
```

Panel Flutter

Figure 2-11. Output of Fatigue and Panel Flutter Analyses

In this way, a method of deriving the manufacturing costs and material costs of the complete TPS system has been developed with its basis at the detailed parts level. The parts listing process occurs as a function of the panel concept (specified by KINDP = 1, 2, 3 as shown in Figure 2-12). A detailed parts listing for the specified configuration is included in the manufacturing cost summary, Figure 2-13.

2.1.4.2 Weights. Actual and purchase weights are computed for each detail specified in the parts listing process; the results are listed in the output under the headings ACTUAL WEIGHT and MATERIAL WEIGHT. Actual weight is just what the name implies. It is computed based on the actual geometry of the finished detail part, taking into consideration all the necessary manufacturing and design requirements that normally

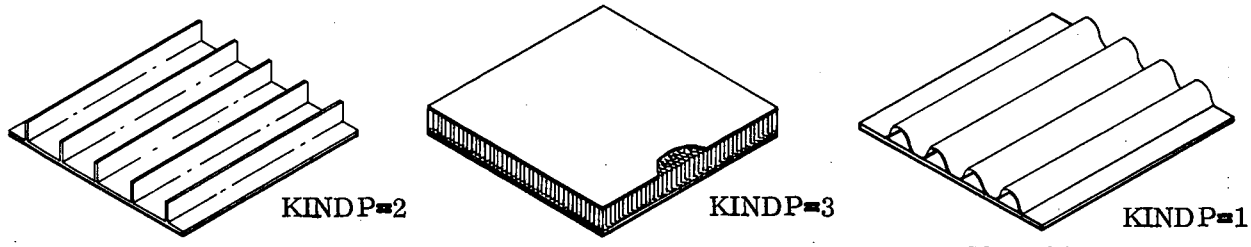

RIB-STIFFENED HONEYCOMB SANDWICH CORRUGATED

Figure 2-12. Panel Concepts

THERMAL PROTECTION SYSTEM, SPACE SHUTTLE STA XXXX

CONFIGURATION PANEL TYPE 1, CORRUGATED NOMINAL PANEL SIZE 3.0 X 2.0 FT
STRUCTURE TYPE A NOMINAL STANDOFF LENGTH .5 IN

DESCRIP	QT	THEORETL WEIGHT	ACTUAL WEIGHT	MATL WEIGHT	STD HOURS	LABOR HOURS	LABOR RATE	OV-HD RATE	MATL $ PER LB	LABOR COST	OVERHD COST	FACTORY COST	MATERIAL COST	FABRICAT COST
PANEL	1	0.000	14.272	18.719	0.0000	0.00	0.00	0.00	0.00	0.00	0.00	0.00	0.00	0.00
CORRUGNS	1	0.000	14.272	17.014	9.8908	24.73	4.75	8.31	14.50	117.45	205.54	323.00	271.38	594.37
STRUCTURE	1	0.000	1.140	1.701	0.0000	0.00	0.00	0.00	0.00	0.00	0.00	0.00	0.00	0.00
BEAM LN A	1	0.000	.346	.425	.3381	.85	4.75	8.31	14.00	4.01	7.03	11.04	6.55	17.59
BEAM SH A	1	0.000	.217	.280	.2103	.53	4.75	8.31	14.00	2.50	4.37	6.87	4.32	11.19
CORNERS	1	0.000	.058	.088	.0628	.16	4.75	8.31	17.50	.75	1.30	2.05	1.30	3.35
POST RCRN	2	0.000	.067	.383	.3111	.59	4.75	8.31	12.00	2.79	4.87	7.65	5.05	12.70
SEAL	1	0.000	.073	.112	.0505	.13	4.75	8.31	14.50	.60	1.05	1.65	1.79	3.44
FASTENERS	40	0.000	.375	.412	0.0000	0.00	0.00	0.00	172.71	0.00	0.00	0.00	60.22	60.22

TOTAL THEORETTCAL WEIGHT	0.00 LB
TOTAL ACTUAL WEIGHT	15.41 LB
TOTAL MATERIAL WEIGHT	19.72 LB
TOTAL STANDARD HOURS	10.86 HR
TOTAL LABOR HOURS	26.97 HR
TOTAL LABOR COST	128.09 $
TOTAL OVER COST	224.16 $
TOTAL FACTORY COST	352.25 $
TOTAL MATERIAL COST	360.61 $
TOTAL FABRICATION COST	702.86 $
TOTAL ASSEMBLY COST	21.05 $
TOTAL MANUFACTURING COST	723.91 $
TPS COST	120.65 $/SQ FT
TPS WEIGHT	2.57 LB/SQ FT
AVERAGE MATERIAL	18.72 $/LB
AVERAGE LABOR RATE	4.75 $/HR
AVERAGE OVERHEAD RATE	8.31 $/HR
AVERAGE FACTORY RATE	13.06 $/HR
AVERAGE MFG. RATE	26.86 $/HR
AVERAGE MFG. RATE	46.60 $/LB
AVERAGE REALIZATION FACTOR	.40
ASSEMBLY REALIZATION FACTOR	.40
COMPONENT NON-OPTIMUM	0.00

SUB-ASSEMBLY COST

TASK	STD HOURS	TOTAL HOURS	LABOR RATE	OV-HR RATE	LABOR COST	OVERHD COST	ASSEMBLY COST
LOCATE	.0456	.11	5.20	1.75	.59	1.04	1.63
CLAMP	.2800	.70	5.20	1.75	3.64	6.37	10.01
DRILL	.0418	.10	5.20	1.75	.54	.95	1.49
SECURE	.0570	.14	5.20	1.75	.74	1.30	2.04
INSPECT	.0304	.08	5.20	1.75	.40	.69	1.09
DISASSY	.0960	.24	5.20	1.75	1.25	2.18	3.43
CLEAN	.0380	.09	5.20	1.75	.49	.86	1.36

Figure 2-13. Manufacturing Cost Summary

go into producing a real part. Purchase weight is the weight of the raw material that must be purchased to produce each detail part. It is always larger than the actual weight. Calculation of the actual and purchase weights for a TPS detail part of the thermal protection system uses an equation of the form demonstrated below.

$$\text{Actual weight} = \text{density} * \text{length} * \text{width} * \text{thickness} \quad (2\text{-}20)$$

$$\text{Purchase weight} = \text{density} * (\text{length} + C_1) * (\text{width} + C_2) * (\text{thickness} + C_3) \quad (2\text{-}21)$$

where C_1, C_2, and C_3 are incremental distances added to the part geometry to account for the material removed during the cutting to size manufacturing operations. The actual equations can be found in the subroutine WTTPS in the program listing.

2.1.4.3 Manufacturing Processes. To predict the manufacturing processes required for each detail part, a library of shop orders and shop planning records was established. These processes, along with the Convair Aerospace San Diego operation standard hour data, were studied and used to identify basic standard shop operations and to correlate each detail part in the parts list with a set of these standard shop operations. The data are used to compute the standard hours necessary for each shop process required in the production sequence of each detail part.

Derivation of Standard Hour Equations

The Standard Hour equations are derived based on Standards data acquired through the industrial engineering department. Typically the Standards data are comprised of three major items - a machine setup time, a part handling time, and a machine run time. These may be considered separately, or are sometimes combined into tables. Each item considered may be either a constant time increment per job or per part, or may be a function of the part geometry or characteristic machine operation parameters. For example, in edge burring, the handling time is a function of the part area in square inches, and the run time is a function of the length to be burred in inches. In straddle milling, the handling time is again a function of the part area, but run time is a function of the volume of material to be removed from each part in cubic inches. In each case the setup time is a constant used once per job.

An example of the initial form of the Standards data is included in Figure 2-14. The data presented is in table form and represents the Standards for a HUFFORD A-12 extrusion stretch forming press, Convair machine code 8030. In this case the total standards hours are made up of two basic items, machine setup time (one increment per part for performing, and one for finish forming). The run time increments are a function of the overall part length.

The development of the Standard Hour Subroutine involved acquiring the general Standards data and deriving an equation for each manufacturing operation based on the characteristics

SETUP: 0.52 (once per die change)				MACHINE CODE: 8030			
PREFORM							
Length	0-15	16-30	31-45	46-60	61-75	76-90	91-105
Std. Hr.	.0255	.0285	.0315	.0345	.0375	.0405	.0435
Length	106-120	121-135	136-150	151-165	166-180	181-195	196-210
Std. Hr.	.0465	.0495	.0525	.0555	.0585	.0615	.0645
FINISH FORM							
Length	0-15	16-30	31-45	46-60	61-75	76-90	91-105
Std. Hr.	.0595	.0625	.0655	.0685	.0715	.0745	.0775
Length	106-120	121-135	136-150	151-165	166-180	181-195	196-210
Std. Hr.	.0805	.0835	.0865	.0895	.0925	.0955	.0985
NOTE: Length in inches is based upon the bill of material length of part. All values include stock allowance for vice jaws.							

Figure 2-14. Standard Hours for Press, Extrusion Stretch Form

process and part parameters. For the example Standards data, a general equation takes the form

$$STDHR = 0.52 + N \left[f_1 (L) + f_2 (L) \right] \quad \text{(hours)} \qquad (2\text{-}22)$$

where

0.52 = setup time (constant per job)

N = total number of parts to be produced

$f_1(L)$ = preform time as a function of part length

$f_2(L)$ = finish form time as a function of part length

The functions of length $f_1(L)$ and $f_2(L)$ are determined by curve fitting the data in the Standards table. In this case a linear curve fit is sufficient and the functions resulting are

$$f_1(L) = 0.002\ L + 0.058$$

$$f_2(L) = 0.002\ L + 0.024$$

The resulting Standard Hour equation for this particular press forming operation is then

$$STDHR = 0.52 + N (0.004 L + 0.082)$$

The Standards data are usually derived for aluminum only. To apply the data to additional materials, material complexity factors are utilized. The material complexity factors account for the difference in manufacturing time requirements for performing identical tasks or operations on different materials. These factors are typically required only for those manufacturing operations associated with material removal such as drilling, routing, burring, cutting, etc. Operations which usually do not require complexity factors are cleaning, layout, identification, painting, etc. Factors of 3.8 and 4.2 are commonly used as complexity factors for steel and titanium respectively. Methods are available for deriving complexity factors for other materials; these methods will be explored and factors developed for all the program material selections. Figure 2-15 presents a list of the manufacturing operations currently available within the Standard Hour subroutine. Provision has been built into the subroutine to allow the future addition of any number of new operations.

305	Burring, Edge	339	Layout Holes, Sheet Metal
308	Clamping	340	Layout Holes, Machine Shop
310	Cleaning, Basket (Degrease)	341	Layout Part, Machine Shop
311	Cleanup, Assembly	343	Milling, Chemical
312	Disassembly	348	Milling, Straddle
314	Drilling, Single Spindle	353	Painting, One Coat
315	Drilling and Tapping or Reaming	371	Routing, Edge (Single Piece)
316	Drilling, Assembly	375	Sawing, Cross Cut (Extrustions, Sections)
317	Forming, Hot Pressure Forming (Sheet Metal)	380	Securing
326	Heat Treatment	382	Setup, Assembly
332	Identify, Rubber or Steel Gang Stamp	383	Shearing to Size
336	Inspection, Assembly	385	Surface Treatment
337	Inspection	392	Turning - Brazing
338	Layout Part, Sheet Metal	397	Welding - Brazing

Figure 2-15. Basic Manufacturing Operations for Which Standard Hour Estimates are Available

Seven standard shop operations were identified for this study

Mfg. Operation Index	Mfg. Operation	Mfg. Operation Index	Mfg. Operation
1	Cuttoff	4	Drilling, Routing, Deburring
2	Milling	5	Surface Treatments
3	Forming	6	Heat Treatments
		7	Painting, Identification

Cutoff includes issue of the stock material to the shop and all cutting or sawing operations required during production. Milling includes milling, boring, and turning operations; forming includes all forming, stretch forming, and bending operations. Drilling, routing, and deburring operations are considered as a related group. Surface treatments include chemical milling, etching, anodizing, and peening. Heat treatments, painting, and part identification are also considered. An example of a callout for the manufacturing operations required to produce a corner post is

Corner Post (Titanium) Manufacturing Operations

KR and KS = 1 . 2 . 4 . 6 . 7

Thus, the operations include cutoff, milling, drilling, heat treating and identification.

The set of operation indexes KR and KS are then used by the program along with a material form index KK to call out values from the arrays KSETUP (KK, KS) and KRUN (KK, KR) located in the K-TABLES with BLOCK DATA. These values (in hours per pound actual weight) are then used to estimate a setup time and a run time required to manufacture each detail part. It is assumed that one basic machine setup is required per detail part, and that the setup for each additional like part is included with the run time. The equations take the following form

Setup Time (SETUP): ACWT * KSETUP (KK, KS)

Run Time (RUNTM): ACWT * KRUNTIM (KK, KR)

where ACWT is the actual weight of the detail part. The setup and run times calculated are in standard hours as discussed in the following section.

To predict the operations required to assemble the detail parts into the basic subcomponents and then to develop a complete final assembly, a library of shop assembly planning records was established. Basic processes were identified and correlated with each subassembly and with the final assembly. This information is established in equations to compute the standard hours for subassembly and final assembly.

Seven standard assembly operations were identified for this study. They are given in the table below along with their appropriate assembly operation.

Assembly Operation Index	Assembly Operation	Assembly Operation Index	Assembly Operation
1	Setup	4	Securing
2	Clamping	5	Inspection
3	Drilling	6	Disassembly
		7	Cleaning

Setup includes the mounting of parts to assembly fixtures, and clamping involves the clamping together of the parts to be assembled. Drilling considers the location, center punching, and the drilling of all required holes. Securing consists of the actual attachment of required fasteners, and inspection is self explanatory. Cleaning involves the final cleaning of the finished assembly and any cleanup required during the assembly process, such as deburring of the holes after drilling. In some cases after drilling, it is necessary to disassemble the assembled parts for inspection and cleanup purposes. The disassembly process is essentially the reverse of the setup and clamping processes, and includes reassembly before the final securing is done. The program calculates a value in hours for each required subassembly and for the final assembly of the finished part. Currently, these calculations are based on constants stored with the BLOCK DATA. The actual equations take the following form.

Setup Time:	HOLES * TIME6	Securing Time:	HOLES * VALUE
Clamping Time:	CLAMP * TIME1	Inspection Time:	HOLES * TIME 2
Drilling Time:	HOLES * VALUE	Disassembly Time:	CLAMP * TIME 5
		Cleaning Time:	HOLES * TIME 3

where: HOLES = number of fasteners (fastener holes)

CLAMP = number of clamps

VALUE = volume of material removed from all the holes × a material complexity factor based on the material type × TIME 7

The material complexity factor is assumed to be 3.0 for titanium. The constants TIMEX where X = 1 through 7 are stored in the BLOCK DATA as

TIME1 = 0.035 hour/clamp
TIME2 = 0.0008 hour/hole
TIME3 = 0.01 hour/hole
TIME4 = 0.0015 hour/hole
TIME5 = 0.012 hour/clamp
TIME6 = 0.0012 hour/hole
TIME7 = 0.52 hour/cubic inch

Provision has been built into the program so that the constants TIMEX can be replaced with equations. Values replacing the constants will be computed using these equations, which will be based on data collected and curve fit during the course of further study. An example of the type of data available is shown in Figure 2-16 where the hours required for drilling in titanium are shown as a function of the volume of material removed.

2.1.4.4 Standard Hours. For each detail called out in the parts listing process, there is a corresponding list of required manufacturing operations in the cost subroutine. For each manufacturing operation a calculation of required standard hours is made.

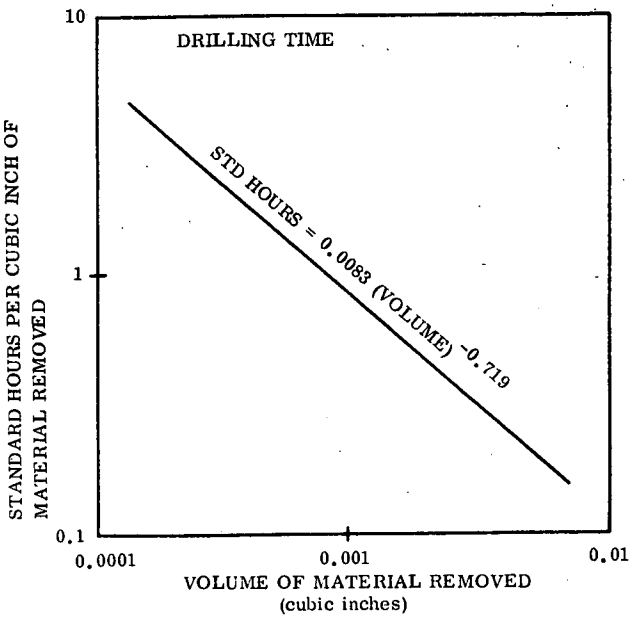

Figure 2-16. Drilling Time in Titanium

Standard hours are defined as a standard time, measured in hours, representing an optimum required to perform a task. Standard hours for each production process are established by the industrial engineering department by analysis of time and motion studies of typical tasks. They are used as a means of measuring performance by determination of realization factors (or efficiencies) when compared with actual labor hours acquired through labor accounting processes.

Within the program, standard hours are calculated for two separate cost areas: factory production and final assembly. Factory production includes the manufacturing and assembly of detailed parts into the basic subcomponents such as posts and beams. Final assembly involves the final assembly of the subcomponents into a finished TPS system. A listing of standard hours is output as part of the cost data under the heading STD HOURS (see Figure 2-13).

Standard-hour data have been collected for each of the seven manufacturing processes and assembly operations discussed; they have been adapted for use with this program. Standard-hour values are used to estimate the actual labor hours required for each of the production processes, and then to estimate the actual labor costs. Figure 2-17 presents an example of a (Convair Aerospace San Diego operation) shop planning order. Listed are the various manufacturing processes required to produce a brace and the corresponding number of standard hours required for setup and running each shop process. The object of the standard-hour calculation technique in the program is, in effect, to be able to predict the planning order.

Calculation of the standard hours for each of the manufacturing processes is performed in two parts: setup time and actual run time. Setup time is derived based on the size of the part, the complexity of the required setup, and the type of machine to be used. Run time is dependent on the machine operation rate, amount of material to be removed, depth of cut, and the surface area to be covered. The manufacturing standard hour equation is

$$STDHR = SETUP + RUNTM * KT * SHIPSET$$

where

SETUP is the setup time in standard hours

GENERAL DYNAMICS CONVAIR
SHOP ORDER PLANNING

H-DAY	AREA	PART NUMBER	LT-NO
471	2	4T11015-133A	A

PLANNER	GRP	CHG CD	D/C	P/L	QCA-NO	PT-CL	LT-NO	AREA	PART NUMBER
EHUGHES	11		8		592	2	A	2	4T11015-133A

TITLE	MATERIAL PERCENT	GRP NUMBER	A/Z
BRACE	4.000	12 120471	D

MATL DESCRIPTION	GAU/DIA	WID/WALL	LENGTH	SPECIFICATION	COND	PTS	OP/HND
NOTE A			40.000	QQ-A-200/12	NOTE	01	

DATE	STK RM	QTY	BY	SPARE	CUST	SHOP	INSP

-----OPERATIONS-----

INSP STMP	DEPT	CC	OPER NO	OPER SCHD	OPERATION DESCRIPTION TOOL/SPEC NO	TOOL SEQ NO	TOOL SYMB	MACH CODE	SET UP	RUN TIME
			A		H/F LS39157-1 7079 T6511					
			B		DS30004					
	836	07	C10		SAW TO LENGTH 4T11015-129A		SP	5880	0.12	0.0031
	036	07	020		SAW ANGLE CUTS SP			6880	0.19	0.0032
				025	INSPECT					
	045	00	C30		ROUT .50R (1) END			0000		
				035	INSPECT					
	001	06	040		SAW 3.50R CNT (2) 129A SP 4T11012-109A		SF	6881	0.19	0.0042
	001	12	050		BURR			2905		0.0106
	001	12	060		IDENTIFY TAG			2910	0.07	0.0008
				065	RW					
				075	INSP					
	002	05	080		ALK. ETCH STP57-301			5845		0.0104
	002	11	090		SULPH. ANOD STP58-208			5807		0.0078
				095	INSPECT					
	002	03	100		(1) ZC PRIMER STP59-201			4815	0.10	0.0068
	002	03	110		IDENTIFY R/S STP63-001			2910	0.07	0.0032
				115	INSPECT					
							TOTAL		0.74	0.0507

Figure 2-17. Example of a Shop Planning Order for a Brace

RUNTM is the run time in standard hours

KT is the number of parts required of a given detail to produce a complete component

SHIPSET is the number of shipsets of that component produced

The standard data are usually derived for aluminum only. To apply the data to additional materials, material complexity factors are utilized. The material complexity factors account for the difference in manufacturing time requirements for performing identical tasks or operations on different materials. These factors are typically required only for those manufacturing operations associated with material removal such as drilling, milling, routing, burring, cutting, etc. Operations which usually do not require complexity factors are cleaning, layout, identification, painting, etc.

Factors of 3.8 and 4.2 are commonly used as complexity factors for alloy steel and titanium, respectively. Methods are available for deviring complexity factors for other materials, but at present values based on the factors used in the COSTOT subroutine are used. These factors are described under PROGRAM COST SUMMARY of this report. Table 2-3 summarizes the values for material complexity factors currently in use.

Table 2-3. Summary of Material Complexity Factors Currently Being Used in the ASTDHR Subroutine

Material	Material Complexity Factor, F
Aluminum	1.0
Titanium	4.2
Inconel 718	4.2
Hastelloy X	4.0
René	4.2
TD Nicrome	5.0
Columbium C-6752	6.0
Columbium C-129Y	6.0
Haynes 188	4.2
Tantalum	6.0
Alloy Steel	3.8
Stainless Steel	4.2
Magnesium	4.0
Beryllium	5.0
L-605	4.2

Calculation of the standard hours for each subassembly operation and for the final assembly is performed using the equations discussed in the previous section. The value of standard hours determined for subassembly processes are summed and added to the manufacturing process standard hours and listed for each detail part. The standard hours determined for the final assembly of the completed component are listed separately after each assembly process.

2.1.4.5 Realization. Realization factors are the ratio of standard hours assigned for a given process to the actual hours required. Realization for a process is used as a means of measuring actual performance against a standard time that is typically an ideal number of hours. It is a measure of shop efficiency and, as such, varies from department to department and from day to day within a department. Realization data for the various departments involved in production tasks at the Convair Aerospace San Diego operation have been collected, studied, and adapted for use with the program. Since these data take into account the effects of the learning curve for a specific task, realizations can be specified

either as an average value or as a time-dependent variable. Some of the factors affecting realization are

a. Inaccurate planning of the required work, setup times, or run times.

b. Machine breakdown.

c. Change in machine, tools, or procedure which are not reflected by corresponding change in standard hour estimates.

d. Tool breakage and part spoilage.

e. Availability of previous setups.

f. Use of special supervision.

g. Ability and level of effort of individuals assigned to the task.

Some of these factors are subject to control by managers and foremen, but they can also vary based on the current shop work load. Realization factors are useful in determining the overall effect of deviations from standard hour estimates. Realization for a particular task is defined as standard hours divided by actual labor hours.

In the program, values for realization are stored for each manufacturing and assembly process, and since standard hours can be estimated, the actual labor hours can be calculated:

$$\text{Actual Labor Hours} = \text{Standard Hours/Realization}$$

Realization factors, along with labor rates and overhead ratios, are stored within the program. Provision has been made in the program for a different realization factor for each of the manufacturing processes, for subassembly, and for final assembly operations. However, at present, a constant realization factor of 0.40 is used for all operations, but data is readily available to establish an individual realization for each operation (although these factors would be strictly valid only within the Convair Aerospace San Diego operation shops).

Average realization factors, along with the computed labor hours, are listed for each part in the cost output data under the headings REAL FACT, LABOR HOURS, and TOTAL HOURS. Figure 2-18 illustrates some typical realization factors and manufacturing standard hours plotted as a function of the number of ship sets.

2.1.4.6 Labor and Overhead Rates. Labor and overhead rates are used within the program to calculate appropriate costs, based on the number of actual labor hours required for each manufacturing and assembly process.

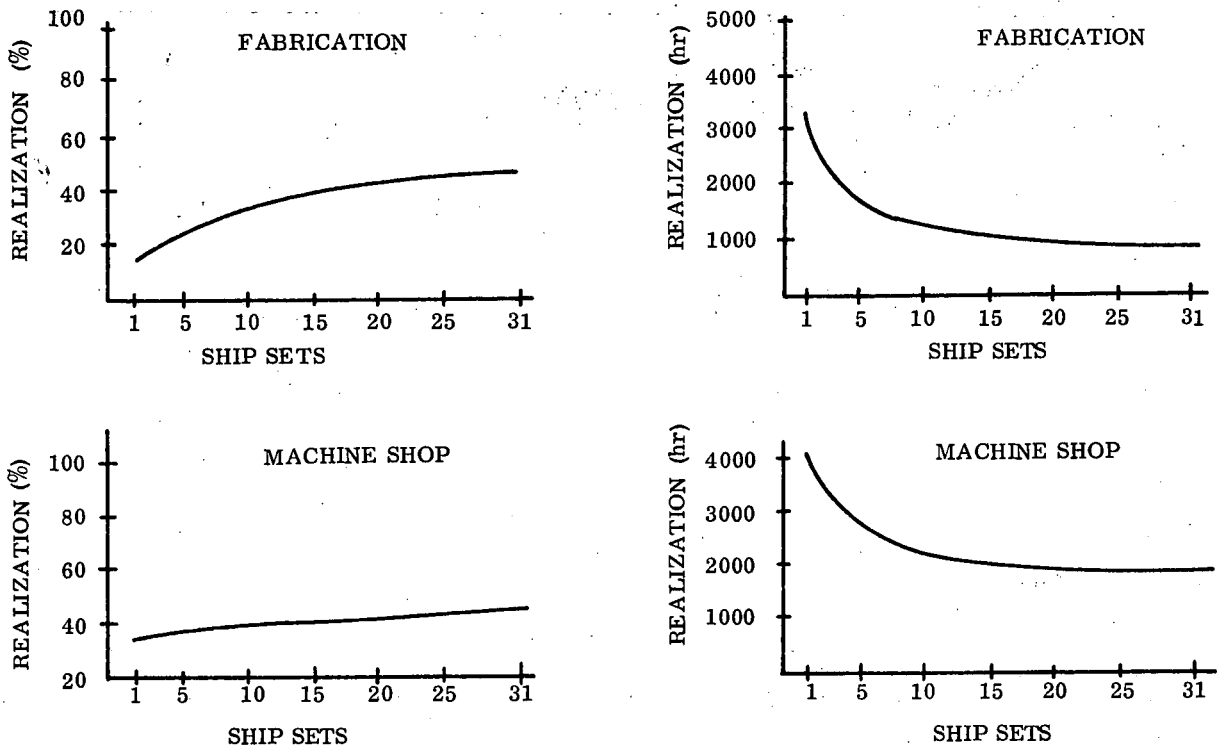

Figure 2-18. Typical Realization Factors and Standard Hours

Labor rates reflect the wages paid directly to the individual employees for each hour of clock time. The rates do not include fringe benefits or company contributions to retirement, Social Security, and state unemployment; these are considered part of the overhead cost. Also included as part of overhead are indirect labor costs, maintenance, supplies, taxes, insurance, and depreciation.

Labor rates are largely uncontrollable by management, being a function instead of union/management agreements and reflecting current labor supply and demand, general economic conditions, and inflation. Labor rates are a function of time and are readily predictable over the short term, although the incorporation of time-dependent equations has been left for future work. At present, the program can store a labor rate corresponding to each manufacturing process and the assembly operations. However, a constant manufacturing labor rate of $4.75 per hour is used, and for the assembly operations a constant rate of $5.20 per hour is used.

The overhead ratio is the ratio of overhead costs to labor costs and can, therefore, be used to determine an effective overhead rate

Overhead Rate = Overhead Ratio * Labor Rate

The overhead ratio is a useful tool for estimating purposes, and is readily available based on past labor cost and overhead cost data. The program can store an overhead

ratio corresponding to each manufacturing process and the assembly operations. A constant ratio of 1.75 is used at present. Representative values of labor rates and overhead ratios as a function of time are presented in Figure 2-19. Values for the realization factor, labor rate, and overhead ratio are stored in the program.

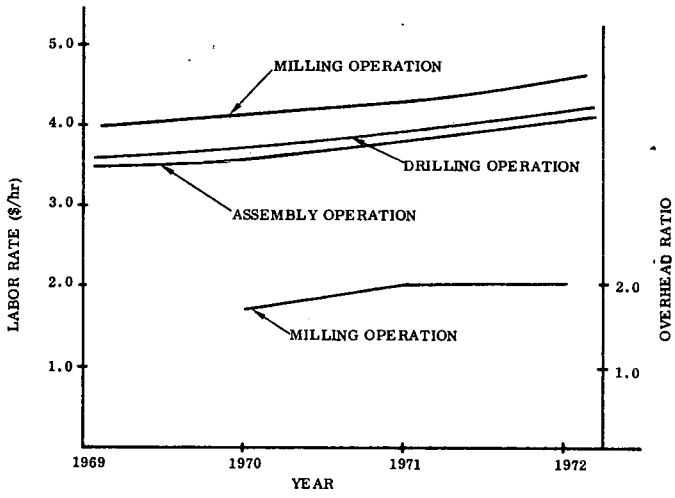

Figure 2-19. Typical Factory Direct Labor Rates and Overhead Ratios

The average labor rate for each part is output with the cost data, along with the corresponding average overhead rate (overhead ratio for final assembly costs). Labor cost and overhead costs are calculcated for each part as the product of the labor hours and labor rate, respectively. Factory costs and assembly costs, then, are the sum of the corresponding labor and overhead costs.

2.1.4.7 Material Costs. Material costs are computed based on the material type and alloy (titanium, columbium, beryllium, et al), material form (sheet, plate, bar, et al), and the raw material purchase weight. The actual calculation of material cost takes the form

$$MATCOS = AMUV * KCOSWT * MAWT$$

where MATCOS is the material cost in dollars for a given detail part, AMUV is the manufacturing usage variance factor explained below, KCOSWT is the material unit cost in dollars per pound, and MAWT is the raw material purchase weight described under WEIGHTS of this report.

The calculation of material costs requires the derivation of a material unit cost KCOSWT and the definition of a material manufacturing usage variance factor AMUV (the calculation of MAWT is done during the weight analysis portion of the program). The parameters KCOSWT and AMUV originate in the AMATL subroutine, which is called from the ASTDHR subroutine once for each detail part, immediately prior to return to the COST subroutine. The actual material cost calculation takes place in the COST subroutine.

The material unit cost KCOSWT is in general a function of the material type, alloy, and temper, material form, quantity of material bought, and special feature requirements such as special close tolerances, special lengths, widths, or thicknesses, and special marking. The determination of a value for material unit cost takes place in the AMATL subroutine where material price data has been curve fit and organized into equation form. Note that the integration of this subroutine into the program does away with the need for KCOSWT and KMUV K-TABLES previously provided in the BLOCK DATA subroutine.

Material form is specified by defining a value for KEY in the ASTDHR subroutine. Each detail part is assumed manufactured from the following forms:

KEY = 0	Insulation	KEY = 4	Wire, Rod, Car	KEY = 8	Casting
1	Fastener	5	Extrustion	11	Surface Insulation
2	Honeycomb	6	Tubing		
3	Foil, Sheet, Plate	7	Forging	12	Ablative

Material type is specified by input of a value for MATLID, which represents the system primary structural material. The materials currently available in the program are summarized in Table 2-4. The defining of values for KEY and MATLID directs the program to a block of cost data within the AMATL subroutine which is associated with the given material type and form. The material base price is then calculated utilizing the nominal material size requirements of length, width, and height (thickness) which are also carried over from ASTDHR with KEY and MATLID.

Table 2-5 shows a portion of a typical price schedule for alloy steel plate between 0.25 and 6.00 inches thick. The equation resulting from a curve fit of the data takes the form

Table 2-4. Summary of Primary Structural Material Types Currently Available in the Program

Aluminum	MATLID = 1
Titanium	2
Inconel 718	3
Hastelloy X	4
René 41	5
TD Nicrome	6
Columbium Cb 752	7
Columbium C-1294	8
Haynes 188	9
Tantalum	10
Alloy Steel	11
Stainless Steel	12
Magnesium	13
Beryllium	14
L-605	15

Table 2-5. Example of a Typical Portion of a Material Price Schedule for Alloy Steel Plate

Thickness (inches)	E4340 AMS-6359 Hot Rolled Annealed
0.250	45.00
0.375	44.40
0.500	44.15
0.625	44.25
0.750	44.10
1.000	43.95
1.250	44.00
1.500	44.00
1.750	44.55
2.000	44.55
2.250	47.40
2.500	47.40
2.750	47.40
3.000	47.40
3.500	47.40
4.000	47.40
4.500	47.40
6.000	47.40

PBASE = .006 * THK + .439

where PBASE is the base price of the material in dollars per pound and THK is the thickness in inches. Thus, by specifying MATLID = 11, KEY = 3, and THK equal to the characteristic height, the program is directed to calculate the base price for a required size of alloy steel plate. In a similar manner the base price data for other material types and forms were curve fit and the resulting equations are available within the AMATL subroutine.

The total material unit cost KCOSWT is equal to the material base price PBASE plus the sum of any extra cost item requirements PEXTRA. Table 2-6 presents a list of extra cost items available for aluminum plate, and Table 2-7 presents an example of one of the items, the quantity buy price differential. Typical extra cost items such as the quantity buy price differential, identification marking, packing for shipment, heat treatment, and ultrasonic tests, were curve fit in the same manner as the material base price data. They were organized in equation form for each material type and form to make up PEXTRA. In this way the total material unit cost + PEXTRA in dollars per pound is calculated directly within the AMATL subroutine.

Table 2-6. Summary of Extra Cost Items Available for Aluminum Plate

Actual Piece Count
Alloys and Special Extras
Circles
Conversion Coatings
Exact Quantity
Identification Marking - Standard
Identification Marking - Special
Interleaving and Oiling
Lengths, Long
Lengths, Short
Machined Surface (Two Sides)
Mechanical Testing
Packing
Packing - per Mill-Std 649 Sheet and Plate
Protective Tape
Quantity
Test Material Samples
Tolerances
Diameter, Flatness, Length, Thickness and Width
Ultrasonic Inspection

Table 2-7. Example of the Quantity Buy Price Differential for Aluminum Plate

Quantity per Item Pounds	Extra Dollar/Pound
300,000 and over	Base
29,999 - 20,000	0.010
19,999 - 10,000	0.020
9,999 - 8,000	0.050
7,999 - 4,000	0.070
3,999 - 3,000	0.125
2,999 - 2,000	0.285
1,999 - 1,500	0.450
1,499 - 1,000	0.775
999 - 500	1.775
499 - 250	3.715
249 - 1000	9.600
99 - 50	19.800

For some combinations of material type and form, (e.g., coated tantalum sheet) specific price data were not available. For these cases a characteristic material base price was established, as MBASE = 90.00 for coated tantalum. The specified material was then analyzed in terms of the equivalent aluminum material form (aluminum sheet), and the resulting value of PBASE derived for the equivalent aluminum form was ratioed using an aluminum base price (ALBASE = .80) and the specified material base price (MBASE). Table 2-8 summarizes the values of MBASE in dollars per pound currently being used in the program.

Table 2-8. Summary of Values for the Characteristic Material Base Price Currently in Use in the Program

Titanium	MBASE = 8.50
Inconel 718	6.00
Hastelloy X	15.00
René 41	8.00
TD Nicrome	105.00
Columbium Cb 752	110.00
Columbium C-1294	110.00
Haynes 188	15.00
Tantalum	90.00
Alloy Steel	0.40
Stainless Steel	0.96
Magnesium	
Beryllium	150.00
L-605	
Insulation	10.00
Ablative Material	
Reusable Surface Insulation	

The manufacturing usage variance factor AMUV is the ratio of the actual amount of material purchased to the original estimated amount of material required for manufacturing. The factor is, in general, a function of the material form and past manufacturing experience. The factor results from material and part overbuying to account for normal material losses during the manufacturing phase of production; it is established by accounting practice, as exemplified by Table 2-9. Material losses during manufacturing arise from part spoilage, loss, duplication, substitution, changes, and waste.

A value for the AMUV is defined for each material form (for each value of KEY) in the AMATL subroutine. The defined value of AMUV and the calculated value of KCOSWT are returned to the COST subroutine for the actual calculation of material cost. At present a nominal or average value of 1.10, representing a 10% overbuy, is used for all material forms. The final calculated value for KCOSWT is listed in the output for each detail part under MATL PER LB, and the resulting material cost under MATERIAL COST. The sum of FACTORY COST AND MATERIAL COST are listed as FABRICAT COST, and the total material costs for the complete system are summed under TOTAL MATERIAL COST.

2.1.4.8 Program Cost Summary. An example output of a program cost summary is presented in Figure 2-20. The total program costs are derived on the basis of the TPS gross weight, usually in terms of a Theoretical First Unit Cost or TFU. This is the predicted production cost of the prototype article including manufacturing planning, fabrication, subassembly, sustaining engineering, sustaining tooling, quality control, materials, and subcontracted parts.

Table 2-9. Typical Manufacturing Usage Variance Factors for a Past Commercial Transport Aircraft Program

Contract Lot No.	Material Costs, A (millions of $)	Original Estimated Material Costs, E (millions of $)	Percent Variance (A - E/A) * 100 (percent)	Mfg. Usage Variance Factor
1	40.65	34.74	17.0	1.170
2	4.61	4.25	8.5	1.085
3	16.67	14.39	13.8	1.138
4	22.69	21.40	6.1	1.061
5	16.28	15.84	2.8	1.028
6	66.50	62.15	7.0	1.070
7	10.22	9.84	3.9	1.039
8	68.71	61.94	10.9	1.109

THERMAL PROTECTION SYSTEM COST SUMMARY

	COST $/SQ FT
THEORETICAL FIRST UNIT COST (TFU) 461.49	
NON RECURRING COST	
ED AND D	22248.04
TOOLING	1172.26
GROUND TEST HARDWARE	1730.58
FLIGHT TEST ARTICLES	922.98
FLIGHT TEST S AND RP	309.20
TOTAL NONRECURRING TPS COST	26383.05
RECURRING PRODUCTION COST	
SUSTAINING ENGINEERING - INCLUDED IN TFU	
SUSTAINING TOOLING - INCLUDED IN TFU	
PRODUCTION ARTICLES	461.49
TEST ARTICLE CONVERSION	138.45
TOTAL RECURRING PRODUCTION COST	599.93
RECURRING OPERATIONS COST	
REPLENISHMENT S AND RP	614.70
TOTAL RECURRING OPERATIONS COST	614.70
TOTAL TPS PROGRAM COSTS	27597.68
NUMBER OF PRODUCTION UNITS	1.0

Figure 2-20. Program Cost Summary

The following expressions develop thermal protection system total cost. This is a weight-driven procedure which employs a technique independent of those previously discussed. Values of the embedded constants are given in Table 2-10 and complexity factors are given in Table 2-11; however, specification of the program cost option ICOS as unity allows the user to input his values for these parameters.

Theoretical first unit cost (TFU)

$$TFU = \dot{C}F_1 K_1 (W)^{AT}$$

Engineering Design and Developments Costs (EDD)

$$EDD = K_2 (W)^{BT}$$

Tooling Costs (TOOL)

$$TOOL = K_3 (W)^{CT}$$

Hardware requirements

Ground test hardware (GTH)

GTH = EGTH TFU

Flight test articles (FTA)

FTA = FTH TFU

Flight test spares and replenishment parts (FTSRP)

FTSRP = FTS TFU

} These parameters determine total non-recurring costs.

Production articles(PA)

PA = NPA TFU

Test article conversion (TAC)

TAC = ETA TFU

} These parameters, along with sustaining engineering and tooling (both included in the TFU) determine total recurring production cost.

Replenishment spares and replacement parts (RSRP)

RSRP = OS * TFU

} This parameter determines total recurring operation cost.

The total program cost (TPC) is obtained by a summation of non-recurring DDT&E(NR), recurring production (RP), and recurring operations (RO) costs.

THEORETICAL FIRST UNIT COST. The parameter which is fundamental to computing all other terms of the total program cost is the theoretical first unit cost (TFU). This is the predicted production cost of the prototype article including manufacturing, planning, fabrication, subassembly, sustaining engineering, sustaining tooling, quality control, materials, and subcontracted parts.

Table 2-10. Values of Total Cost Constants

AT	0.667
BT	0.187
CT	0.86
K1	0.00171
K2	6.58
K3	0.004324
EGTH	3.75
FTH	2.00
FTS	0.67
NPA	1.00
ETA	0.30
OS	1.332
STPS	22,000

Table 2-11. Summary of the Complexity Factors Currently Being Used in the COSTOT Subroutine

Material Type MATLID	Structural Configuration KINDP	Complexity Factor CF				
1	1 2 3 4 5	1.3	2.1	1.0	2.1	2.1
2		3.5	6.0	3.0	6.0	6.0
3		3.2	4.3	2.5	4.3	4.3
4		3.1	3.1	1.9	3.1	3.1
5		4.0	4.7	3.0	4.7	4.7
6		5.2	6.9	4.2	6.9	6.9
7		17.0	17.0	12.0	17.0	17.0
8		17.0	17.0	12.0	17.0	17.0
9		3.2	4.3	2.5	4.3	4.3
10		19.0	19.0	14.0	19.0	19.0
11		1.8	2.6	1.4	2.6	2.6
12		2.2	3.0	1.7	3.0	3.0
13		2.2	3.0	1.7	3.0	3.0
14		6.0	10.0	5.0	10.0	10.0
15		3.8	4.6	2.8	4.6	4.6

NONRECURRING DDT&E COST. This program cost consists of the engineering design and development (ED&D) cost and the production cost for ground test hardware (GTH), flight test hardware (FTH), and flight test program spares (FTS). The ED&D cost includes the engineering, design, development, laboratory test, support activities for subsystem development, and the cost of hardware required to support laboratory development testing and component qualification testing. Initial tooling for the fabrication of the subsystem is included in ED&D. Ground test hardware costs reflect all hardware used in both subsystem and combined subsystem development testing. Hardware costs are generated by multiplying the equivalent number of units required by the theoretical first unit (TFU) cost of the subsystem. No cost improvement (learning) is taken during the development program. The TFU cost of the subsystem includes manufacturing planning, fabrication, subassembly, sustaining engineering, sustaining tooling, quality assurance and control, and materials and subcontracted parts.

RECURRING PRODUCTION COST. This program cost covers the cost of manufacturing the production articles (PA) and converting the test articles (TAC) to the operational configuration. These costs are generated by multiplying the equivalent numbers of units by the TFU. No cost improvement (learning) is taken.

RECURRING OPERATIONS COST. This program cost covers the cost of spare hardware required during ten years of operation. The cost is generated by multiplying the equivalent subsystem replacement fraction for 444 flights (OS) by the TFU. Again, no cost improvement (learning) is taken.

The derivation and supporting rationale of the costs for basic subdivisions of work, i.e., engineering (ED&D), manufacturing (TFU and hardware requirements), and tooling, are generally based on one or all of the following: (1) historic cost data actuals, (2) vendor cost data, with or without adjustments, received in support of this or other studies, and (3) other cost models.

Since these models are all based upon a total TPS weight, all computations are made for a total weight based upon a total area of the order of 10,000 ft^2. Hence, total weight is simply the product of panel unit weight and system area, and panel unit cost is derived from the quotient of system total cost and system area, the dividend driven by system total weight. The number of hardware units, flight test spares, and the like are then really portions of the total vehicle TPS and not simply an additional number of panels.

2.1.4.9 Total Program Cost Analysis for RSI, Ablators, and Carbon-Carbon. An additional task was to establish a method for assessing the relative cost differences between alternate, orbiter-vehicle thermal protection systems (TPS). A parametric cost model was developed which calculates TPS total program costs in three categories: nonrecurring (DDT&E), recurring production, and recurring operations (maintenance and refurbishment). This concentrated on three specific TPS concepts, which were reusable carbon-carbon composites (C/C), reusable surface insulation (RSI), and ablatives.

Approach

Since the primary application of costs in this program is for design selection and optimization, emphasis is placed on the determination of relative cost differences rather than absolute costs such as those normally used for contract bidding purposes. The approach used in developing the parametric cost model started with the collecting of available cost data on thermal protection systems. A work breakdown structure (WBS) of major elements of cost was then established for typical thermal protection systems. Next, a set of parametric cost estimating relationships (CERs) were developed which correlated costs with weight for the various WBS elements. A sample calculation demonstrating the use of the model was made for a hypothetical orbiter TPS.

The cost data that were collected for the analysis could be grouped into three general categories, (1) actual costs from historical programs, (2) estimated costs from proposals and study results, and (3) existing cost models.

The actual costs from historical programs were of course the most desirable data because they are most representative of true program costs. However, these data were mostly metallic concepts and consequently only of limited use as a source of analogs for the C/C, RSI and ablative concepts being analyzed in this study. The costs appearing in recent space shuttle proposals and study reports were more similar to the TPS designs of interest in this study, but were estimates and not actual costs. Data from these sources typically suffer from a lack of design definition (e.g., uncertain

weights, no material distributions, no areas, locations, etc), inadequate cost visibility (e.g., no unit manufacturing costs shown, learning assumptions unknown, TPS costs buried in structure, etc), or general incompatibility between the design data shown and the cost data. Existing cost models used by Convair and other contractors were analyzed and utilized in the study. The actual data points which these models use are usually not shown due to proprietary reasons, but general trends such as the slope of various CERs and knowledge of a contractor's product line provided some data for our analysis. Some of the data sources utilized in this analysis were

General Dynamics Historical Data
General Dynamics Space Shuttle Cost Model
North American Rockwell Space Shuttle Cost Model
North American Rockwell Historical Data
Aerospace Corporation Earth Orbit Shuttle Cost Model
Space Shuttle Phase B and Phase B"
McDonnell Douglas Corporation Cost Model

The work breakdown structure established for the cost model is shown below.

TPS Total Program Cost			xxx
Nonrecurring		xx	
Development	xx		
Test Hardware	xx		
Tooling	xx		
Recurring Production		xx	
Production and Test Vehicle Mods	xx		
Recurring Operations		xx	
Operational Spare and Repair Parts	xx		

The elements of cost shown were based on an analysis of the space shuttle final reports and are representative of the total cost for a typical orbiter vehicle thermal protection system.

The development of the parametric cost estimating relationships (CERs) was the major task in building the cost model. Theoretical first unit (TFU) production cost CERs were generated for RSI, C/C, and ablative type TPS concepts. CERs for typical attachment structure and for insulation material were also developed because these two components were generally required in most TPS designs. A similar set of CERs for engineering design and development was also developed. A CER for initial tooling costs was developed as a function of vehicle total TPS weight and was independent of the type of TPS being evaluated. The refurbishment hardware costs for recurring operations were developed in the form of a range of cost-per-flight factors for each of the three TPS concepts. The range in these factors for any given type of TPS reflected the specific application (severity of environment) or location on the orbiter vehicle.

In the development of CERs, statistical regression techniques would normally be applied to a scatter plot of historical data points; however, in this study the lack of sufficient historical data prohibited the use of this method. A modification of this technique was used in which the slope of the CER equation was determined from other supporting data or existing CERs; then a line with this slope was passed through the best available analogs for the component in question. In other cases, CERs were adopted from previously developed cost models if they appeared to be in good agreement with the data and with similar CERs from other sources.

The sample calculation utilized a combination of fully reusable TPS types. Program characteristics (numbers of inventory vehicles, number of flights, test hardware conversion assumptions, etc) used in the sample calculation were based on the Space Shuttle program Phase B study period.

The following ground rules and assumptions were utilized in the analysis.

1. The development cost includes the engineering, design, development, laboratory test, support activities, and the cost of hardware required to support laboratory development testing and component qualification testing.

2. The development hardware costs represent the production cost for ground test hardware, flight test hardware, and flight test program spares.

3. The tooling cost includes all activities for engineering and building of initial tooling required for TPS fabrication.

4. The recurring production cost includes the cost of manufacturing the production articles, converting test articles to operational configuration, and sustaining tooling activities.

5. The recurring operations cost covers the cost of spare and repair hardware required for the flight program.

6. An operational program of 445 flights was assumed.

7. The following hardware requirements expressed in terms of equivalent TFU costs, were assumed:

   Development test hardware consumed = 1.7
   Production articles and flight test conversion = 3.6

8. All costs are in terms of 1970 dollars and exclude fee.

9. No costs are included for vehicle-level activities such as flight test operations, ground support equipment procurement and maintenance, etc.

Results

The cost model results are summarized in equation form in Table 2-12. In the following paragraphs the development of each CER is discussed. The reader should remember that the parametric costing approach required in a study of this type is by nature dependent on historical cost experience. The quality and quantity of historical data on thermal protection systems analogous to the Space Shuttle orbiter vehicle are very limited. Additionally, the relationship between TPS cost and TPS performance is not well understood at this time; consequently, in many cases a single previous data point or trends observed from historical airframe data were utilized in generating CERs.

TFU CERs

The theoretical first unit (TFU) manufacturing cost CERs (Figure 2-21) were based on an analysis of the North American Phase B study results, and existing cost models from Convair Aerospace, Aerospace Corporation, and McDonnell Douglas. A cost/weight scaling exponent of 0.6 was selected from the Aerospace model. This value is in good agreement with historical total airframe data that show cost/weight scaling exponents ranging from 0.5 to 0.8. The McDonnell Douglas model CERs are a function of area and individual panel size; therefore,no direct comparison of selected scaling exponent could be made. The RSI and carbon-carbon concepts are shown as having the same range of costs depending on the specific application. The upper edge of the band shown in the CER would correspond to a more complex application such as the wing leading edge and nose cap areas. The lower edge represents a general application over more gently contoured and lower temperature areas on the remaining body areas and aerosurfaces.

No good evidence was found for distinguishing between the two concepts, and since both are still in the development stages, any claims of "lower cost" must be considered suspect. Reported costs from individual proponents are often based on optimistic or exclusive applications that may not be realized in initial operational configurations. It seems likely that a significant portion of each type will be used on the first orbiter vehicles with carbon-carbon being used in the high-temperature highly contoured areas, RSI in the low-temperature gently contoured areas, and both competing for the moderate-temperature, moderately contoured areas.

The ablative CER is shown at about one-half the complexity of the RSI and C/C. This line passes half way between two independent estimates of an ablative TPS design, and the ratio of complexities between the ablative and advanced (RSI & C/C) concepts is in rough agreement on a similar cost model.

The attachment structure CER was based on the Aerospace cost model and assumed the use of titanium for this application. The North American orbiter TPS carrier panels estimate fell just above (more expensive) this parametric line as could be expected due to the use of a Ti sandwich construction. The insulation CER was taken directly from the Aerospace cost model.

Table 2-12. TPS Cost Model Summary

	Reusable Surf. Insulation	Reusable Carbon Carbon	Ablatives	Attachment Structure	Insulation	Total Orbiter TPS
TFU*	.07181 (WT)$^{.6}$ .06528 (WT)$^{.6}$	.07181 (WT)$^{.6}$ .06528 (WT)$^{.6}$	.03295 (WT)$^{.6}$	.04782 (WT)$^{.6}$	.01500 (WT)$^{.6}$	Σ Components
EDD	.575 (WT)$^{.6}$	.575 (WT)$^{.6}$	.300 (WT)$^{.6}$	.250 (WT)$^{.6}$	.100 (WT)$^{.6}$	Σ Components
Tooling						.004974 (WT)$^{.86}$
Dev. Test Hdwr						Equiv. Dev. Units x TFU
Subtotal Nonrecurring						ΣEDD, Tool, Hdwr
Production Articles & Flt. Test Conversion						Equiv. Unit × TFU
Subtotal Recurring Production						Σ Prod. Articles
Ops Spares Hdwr	%/flight x No. Flts x TFU	% per flt. x No. Flts x TFU	% per flt x No Flts x TFU	% per flt x No. Flts x TFU	% per flt x No. Flts x TFU	ΣComponents
Subtotal Recurring Operations						Σ Spares
Total Program						ΣNonrecurring, Recurring Prod, Recurring OPS

*RSI and C/C TFU is represented by a band rather than a single line.

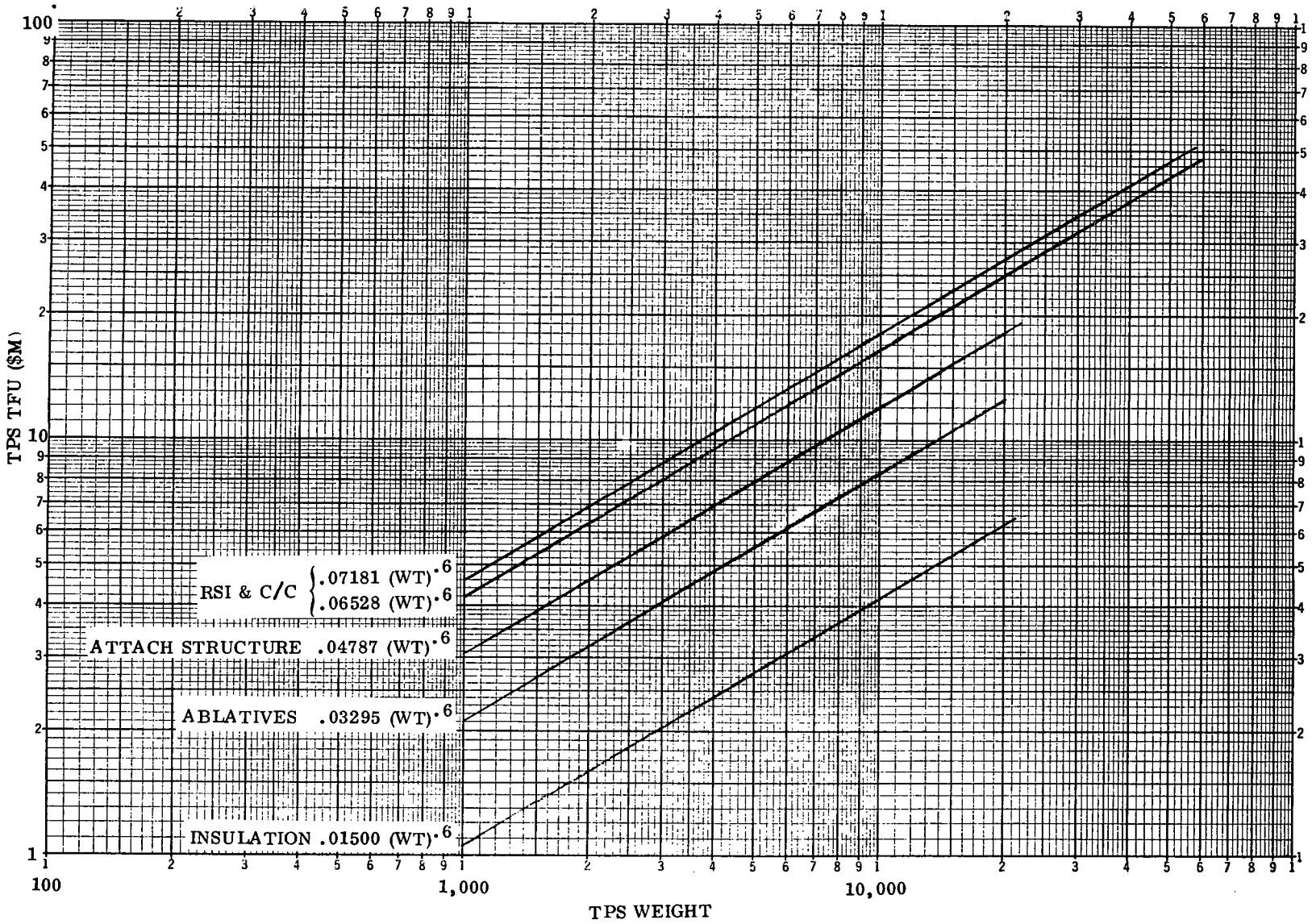

Figure 2-21. Theortical First Unit (TFU) Cost

Initial Tooling CER

The initial tooling cost CER was selected from an existing set of tooling CERs developed for the Space Shuttle booster vehicle (Figure 2-22). The particular line selected was one used for estimating aerosurfaces initial tooling requirements. The physical shapes and contours encountered in aerodynamic surfaces were felt to closely approximate the TPS shapes and contours. Values obtained from this CER were in good agreement with those from the North American final report, McDonnel Douglas thermal-structure tooling CER, and the Aerospace cost model.

ED&D CERs

The engineering design and development CERs (Figure 2-23) used the slope from the Aerospace model TPS. A line with this slope was then passed through the North American orbiter development estimate for an RSI type TPS with C/C nose and wing leading edges. No difference between RSI and C/C was indicated and this CER is properly entered at the total weight of the RSI and C/C. The attachment structure CER was established by passing another line of the same slope through the estimated development cost for the titanium carrier panels on the NAR orbiter. This line coincided with the Aerospace cost model's baseline (complexity factor of 1.0) thermal protection panel CER. The ablative TPS development CER was then estimated to have a relative complexity of about 1.2 based on the Aerospace model's allowance for materials and configuration complexities. This resulted in a line that was about 50% of the RSI and C/C line as was the case for TFU. The CER for TPS insulation was taken directly from the Aerospace model even though this was about 25% higher than the NAR orbiter insulation data point.

Refurbishment CERs

The two contributors to TPS refurbishment costs are hardware consumption, in the form of spare and repair parts, and labor. For this analysis the differences in labor requirements between the various TPS concepts were assumed to be negligible and were excluded. This assumption is reasonable considering the objective of obtaining relative cost differences rather than absolute costs for a specific concept. Historically, the labor portion of operations cost is small compared to the materials used. One reason for this is that labor is not so "dedicated" as hardware. A mechanic can work on landing gears, wings, etc when he is not doing TPS work (i.e., more efficient utilization of a dollar spent on labor versus hardware). Also, this labor portion is unlikely to be greatly different between TPS types because a large part of the labor task is associated with inspection to determine which areas are qualified for an additional flight, and this must be done regardless of the design concept. Removal and replacement activities will be relatively insensitive to TPS type. Here the more important discriminator is likely to be the panel size with smaller panels requiring more labor due to the greater number of dissimilar interfaces which produce problems with joint mismatch, seals and plugs, etc. The scope of this study did not permit going into these details for each

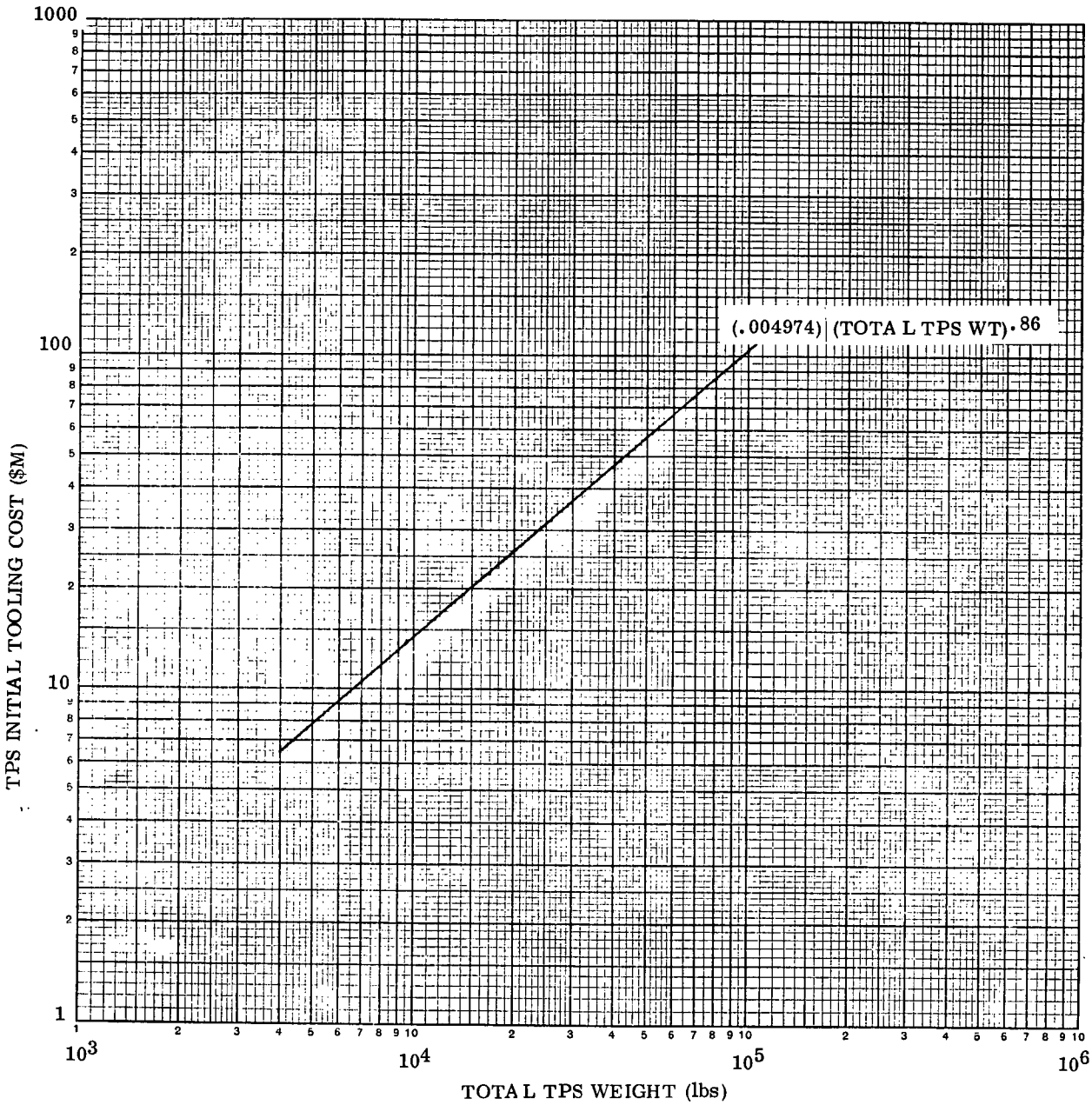

Figure 2-22. Initial Tooling Costs

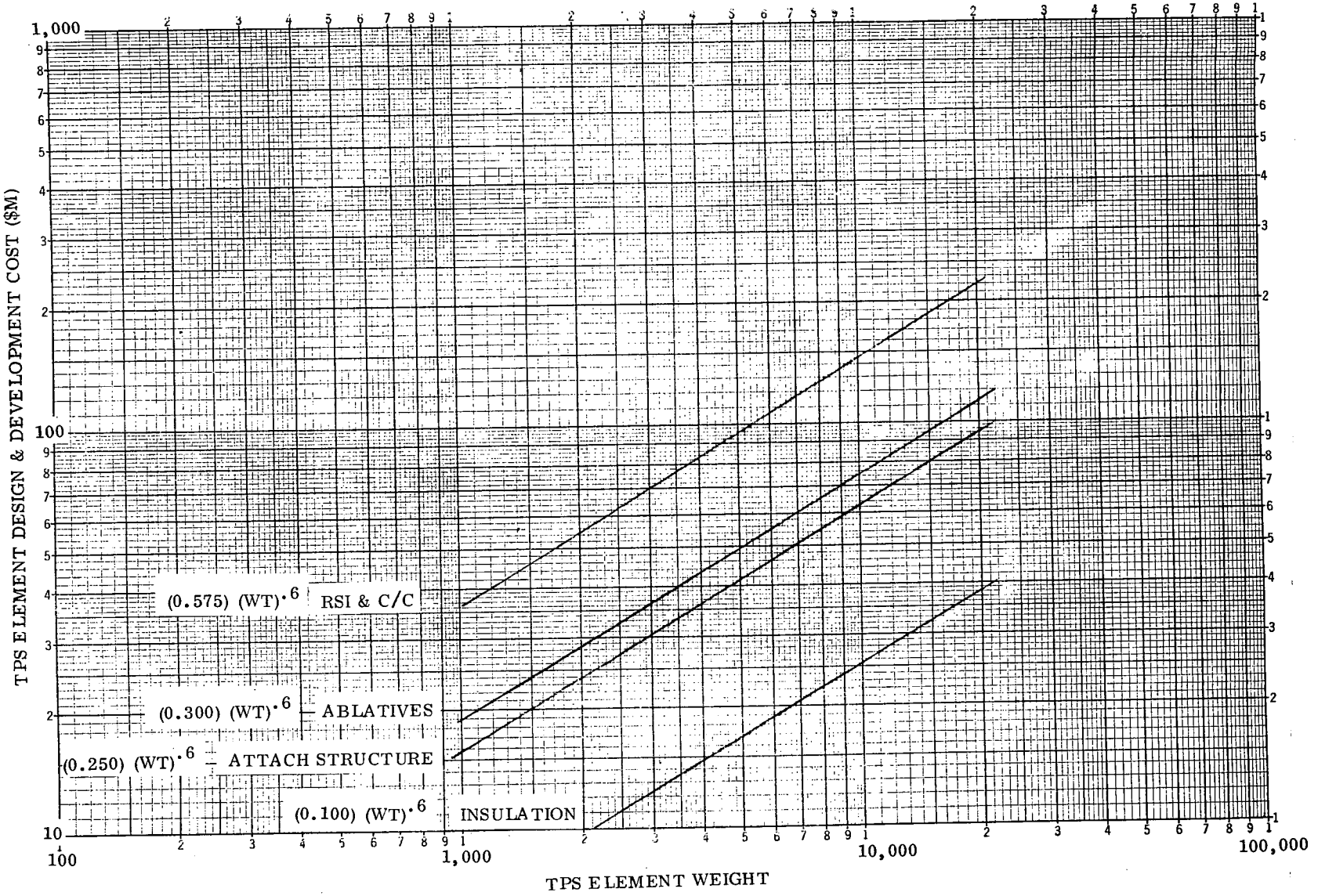

Figure 2-23. Engineering Design and Development Costs

type of TPS. The hardware costs are simply a function of the quantities consumed and their respective unit costs. This consumption was expressed in terms of equivalent theoretical first units per flight, which are multiplied by the TFU costs to get operational spares costs. As in the other areas of the cost analysis, the historical data base applicable to orbiter TPS consumption is minimal. Additionally, the replacement rate of any TPS concept will likely be affected by the degree to which reusability is stressed during development. We can also expect the replacement rate to change (either increase or decrease) through the life of the program. For example, removal frequencies of certain panels may be changed after the initial flights because the predicted thermal loads differ from actual experience. The specific application would also affect the consumption rate. For example, ablatives used on the nose and wing leading edge may require 100% replacement per flight, while on other areas of the wing and body they may withstand 10 or 20 flights. The range of spares consumption rates considered for the TPS concepts analyzed is shown in Figure 2-24.

Sample Calculation

The calculation of a typical TPS total program cost is shown in Figure 2-25. This TPS concept is similar to the design submitted for the North American Phase B 161-C orbiter and assumes the same hardware equivalents for the program.

Uncertainties

The results of the economic analysis must be considered uncertain because of a number of factors peculiar to this study.

1. No schedule effects were considered; consequently, time phasing of costs is not included in the selection criteria. Benefits associated with lower peak-year funding requirements or smaller early-year development outlays are not defined by the cost model. In view of the current budget constraints in aerospace and related fields, this is a limitation of the study.

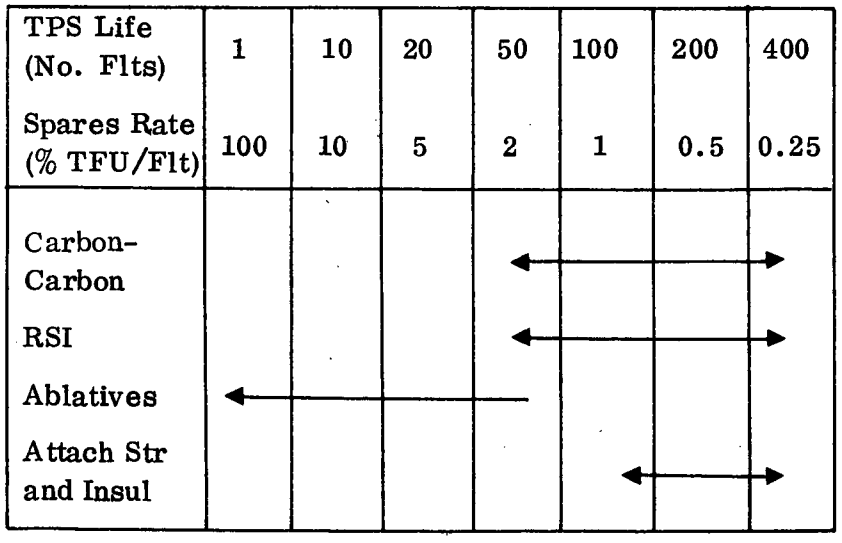

Figure 2-24. TPS Spares Consumption Ranges

2. The general absence of actual historical experience in developing, manufacturing, and operating systems such as those investigated in this study makes the cost model results of this analysis highly uncertain. Adding to this uncertainty (mainly in the CERs

TPS Element	Weight (lbs)	TFU ($M)	Nonrecurring				Recurring Production Qty@TFU=($M)	Recurring Operations %/Flt×No. Flts×TFU=($M)	Total TPS Program ($M)
			ED&D ($M)	Test Hardware Qty.@TFU=($M)	Tooling ($M)	Total Nonrecurring DDT&E ($M)			
Orbiter TPS	(36550)	(42.78)	(296.5)	1.7×42.78=(72.7)	(44.0)	(413.2)	3.6×42.78=(154.0)	— — — =(136.6)	703.8
RSI	20500	25.20	233.0					0.5%×445×25.20=56.1	
C/C	1650	6.20[1]						2.0%×445× 6.20=55.2	
Attach str.	4400	7.28	38.0					0.5%×445× 7.28=16.2	
Insulation	10000	4.10	25.5					0.5%×445× 4.10= 9.1	

[1] Reusable carbon/carbon assumed for nose cap and wing leading edge so TFU based on upper edge of CER band.

Figure 2-25. Sample Calculation - Typical Reusable Orbiter TPS

developed) is the fact that the designs being evaluated are still preliminary in nature with relatively little detail. One would expect a significant difference between the description of any TPS at this time and the actual operational system that results. The cost model, however, is intended to predict the cost of the operational system without the benefits of knowing what the final design will be.

3. Existing cost models have not dealt with these types of systems except on a purely theoretical basis (i.e., "paper" designs). Differences inherent in the existing cost models, such as different cost categories, different cost driving parameters, (e.g., weight vs area), and different ground rules (no fee, no sustaining engineering, no program management, etc) prohibited making a comparison of results on a single TPS concept. Since this analysis relied heavily on current cost model experience, the validity of the results must be considered uncertain.

Values of the total program cost parameters have been developed here (Table 2-13) to allow the program user to input applicable parameters.

2.1.5 MATERIAL PROPERTY DATA. A limited effort was expended throughout the contract to gather and reference the material property data necessary to run the TPS sizing procedure. Much of the data gathered in the previous contract, NAS9-10956, is of course applicable to the metallic cover panel for which the majority of that effort was spent. The efforts of the present contract have been directed to four new systems - RSI, ablators, carbon-carbon, and phase change materials. The following paragraphs discuss references and what properties are available for each material.

Table 2-13. Total Cost Program

Parameter	NSECT			
	1-6	7	8	9
		RSI	Ablator	C-C
CF1	Table	1.0	1.0	1.0
AT	0.667	0.6	0.6	0.6
BT	0.187	0.6	0.6	0.6
CT	0.86	0.86	0.86	0.86
K1	0.00171	0.06528	0.03295	0.07181
K2	6.58	0.575	0.300	0.575
K3	0.004324	0.004974	0.004974	0.004974
EGTH	3.75	1.7	1.7	1.7
FTH	2.0			
FTS	0.67			
NPA	1.0			
ETA	0.3			
OS	1.332			
STPS	1000	1000	1000	1000

The properties of metallics have been amplified by the publication of data by General Electric's publication, Space Shuttle Thermal Protection System Metallic Materials Property Data (Ref. 8). The metallics considered are outlined in Table 2-14 along with the properties included in the handbook. It should be noted that not all properties are necessarily available, but at least an attempt is made to provide them.

Unfortunately, no single compendium exists for properties of the other three concepts: RSI, ablators, and

Table 2-14. List of Metallic TPS Property Data Contained in Reference 8

Materials	Data	
Inconel 718 René 41 TD-Nickel Chromium (2% ThO_2) L-605 (Haynes Alloy No. 25) Haynes Alloy No. 188 Cb-752 FS-85 C-129Y B-66 T-111 T-222	Commercial Designation: Composition: Weight Percent Physical Properties: Thermal Expansion Thermal Conductivity Specific Heat Emittance Density (Room Temp)	Mechanical Properties: Elastic Modulus Shear Modulus (or Poisson's Ratio) 0.2% Yield Strength Ultimate Tensile Strength Tensile Ductility Creep Creep Rupture Bend Ductility Impact Properties High-Cycle Fatigue Low-Cycle Fatigue

carbon-carbon. The reusable surface insulation system has been studied in great detail by three companies: General Electric, Lockheed, and McDonnell Douglas. The final reports of these companies' efforts contain all the current physical and mechanical property values. Since the reports themselves are available in either hard cover or microfiche, only the references are given here (References 9, 10 and 11). Both test and design values are given for all RSI properties as well as data for the glue line, the substrate, and other related parts of the configuration. It was necessary to select a consistent set of RSI properties to be used in calculations during the course of the study. For this, the General Electric data of Reference 11 was selected as typical,and it appears in Table 2-15. This selection was based primarily on the ease of computer implementation considerations and does not imply a preference of recommendation for this material over those supplied by other contractors.

Typical property values for ablative materials are usually available from the material manufacturers. Since no structural analysis is performed on the ablative system, only thermodynamic properties are of interest here. Table 2-16 gives the thermal, thermophysical, and mechanical/physical properties of two charring ablators manufactured by General Electric. These are typical, but if other property data is desired, the program user is urged to check with ablator manufacturers.

Material property data for carbon-carbon composites are difficult to obtain basically because of limited industrial experience in dealing with the materials. The major efforts to date have been performed by the Vought Missiles and Space Company in their Phase II contract on the TPS development for the Space Shuttle wing. Other companies, including Convair Aerospace, have been developing carbon-carbon concepts under company funded research or contracts to other agencies such as NRL. To obtain data for the stringer reinforced leading edge configuration, Reference 12 is recommended. For the truss core configuration, the thermal and mechanical properties

Table 2-15. Typical Properties of Reusable Surface Insulation (RSI)

TEMPERATURE		THERMAL CONDUCTIVITY (Btu/ft sec R) × 10^5			SPECIFIC HEAT (Btu/lbm R)
R	F	P < 10^{-4} ATM	P = 10^{-2} ATM	P = 1 ATM	REI MULLITE
500	40	0.187	0.550	0.95	0.172
600	140	0.215	0.610	1.02	0.195
700	240	0.248	0.673	1.11	0.214
800	340	0.283	0.743	1.20	0.228
900	440	0.33	0.820	1.30	0.240
1000	540	0.376	0.910	1.41	0.250
1250	790	0.532	1.16	1.72	0.267
1500	1040	0.756	1.49	2.1	0.280
1750	1290	1.07	1.90	2.57	0.289
2000	1540	1.60	2.45	3.14	0.295
2250	1790	2.14	3.13	3.86	0.300
2500	2040	3.03	4.00	4.71	0.300
2750	2290	4.30	5.15	5.80	0.300
3000	2540	5.10	6.60	7.07	0.300
DENSITY (lbm/ft^3)		15.0			

developed at Convair Aerospace under company funded research are presented in Tables 2-17, 2-18, and Figure 2-26. The program user is cautioned however, that material properties are extremely process and configuration dependent - to ensure their proper use, only property values ascertained by test for the particular configuration should be used.

For the case of the heat sink TPS (the phase change material - PCM), used in conjunction with the RSI system, thermodynamic properties for a wide variety of PCMs have been gathered at Lockheed Huntsville (Reference 13). These fillers include both high and low temperature phase change materials as well as a number of solid-solid state change ones too. Additional information on heat sink systems is being developed by McDonnell Douglas under Contract NAS8-27708. A limited amount of data has also been gathered to describe the thermodynamic properties of several fiberglass and aluminum honeycomb configurations. These concepts are applicable to the honeycomb substrate which will be used for the RSI both with and without an impregnated PCM. The honeycomb properties are equivalent specific heat and thermal conductivity, the latter being evaluated at low temperature at which radiation effects across the substrate are negligible. These data will be applicable to the RSI TPS since the thermal constraint on the system is a bond line temperature on the order of 300F. The thermodynamic properties are presented in Figures 2-27 through 2-32, and Tables 2-19 through 2-23.

Table 2-16. Properties of Low-Density Elastomeric Shield Materials (ESM 1004)

PROPERTIES		ESM 1004-X			ESM 1004 AP		
THERMAL							
A. Specific Heat (Btu/lb-F)	0F	0.28					
	100F	0.31			0.30		
	300F	0.35			0.39		
	500F	0.38			0.43		
B. Dynamic Enthalpy		Strong Endotherm - 0.01 atm, air Slight Exotherm - 1 atm, air			--- Exotherm (Air, 1 atm, 725F)		
C. Thermal Conductivity × 10^5 (Btu/ft-sec-F) 1 atm, air	0F	1.00			---		
	100F	1.14			2.25		
	300F	1.46			2.14		
D. TGA - 5% Weight Loss		*650F			800F		
50% Weight Loss		1150F			1120F		
Residual Weight		35%			43%		
*ESM 1004A° Post Cure = 500F, ESM 1004X Post Cure = 300F. Initial Weight Loss Due to Unreacted Residual Volatiles and Not Thermal Decomposition							
E. Weight Loss in Vacuum 10^{-5} MM HG - R.T. 5 Days		0.17%			---		
THERMOPHYSICAL							
Virgin Density, ρ_v lb/ft^3		15			35.0		
Char Density, ρ_c, lb/ft^3		6			14.4		
Surface Emissitity		0.85			0.85		
Pyrolysis Gas Specific Heat, CP_g Btu/lb R		0.384			0.384		
Molecular Weight of Injected Species, M_G		24.5			24.5		
Order of Reaction		2			2		
Pre-Exponential Factor, Z sec^{-1}		30,000			30,000		
Activation Energy, E Btu/lb mole		47,500			47,500		
Heat of Decomposition H_{GF}	1135R	50			50		
Btu/lb Gas Generated	1460	450			450		
	1710	1,000			1,000		
	2610	1,960			1,960		
MECHANICAL/PHYSICAL							
A. Density (lb/ft^3)		15 ± 2			35 + 3		
B. Tensile Properties		Stress (psi)	Elong. (%)	Elastic Modulus (psi)	Stress (psi)	Elong. (%)	Elastic Modulus (psi)
	-150F	32	40	95	150	50	300
	-100F	14	--	--	90	46	210
	-50F	9	22	60	70	34	200
	75F	7	22	45	60	25	200
	300F	6	17	45	50(est)	22	200
C. Bond Shear Strength Shield/Bond System		Shear Strength (psf) (RTV 560 to Ti)			Shear Strength (psf) (RTV 560 to BE)		
	-150F	5820			---		
	75F	1320	(Cohesive Failure		10800	(Cohesive Failure	
	300F	1180	in ESM 1004-X)		6750	in ESM 1004AP)	
	500F	1120			4500		
	800F	518	(Adhesive to Ti)		—		
D. Bond Shear Strength - Bond Aluminum to Aluminum RTV 560 Adhesive		Shear Strength (psi)			Shear Strength (psi)		
	75F	600 (Average)			600 (Average)		
	400F	250 (Average)			250 (Average)		
E. Thermo Structural - Low Temperature Compatibility		No Failure Down to -300F as Substantiated by Test			No Failure Down to -300F as Substantiated by Test		

Table 2-17. Assumed Material Properties

Carbon-Carbon (Pyrocarb 500)

Density = 93.7 lb × ft^{-3}

Specific Heat = 0.22 Btu × lb^{-1} × $(R)^{-1}$

Thermal Conductivity* in Btu × ft^{-1} × hr^{-1} × $(R)^{-1}$

Temperature, R	960	1460	1960	2460
Conductivity	.958	.992	1.03	1.06

Dynaflex Insulation

Density = 1 lb × ft^{-3}

Specific Heat in Btu × lb^{-1} × $(R)^{-1}$

Temperature, R	500	1000	1500	2000	2500	3000
Specific Heat	.177	.220	.242	.257	.270	.277

Thermal Conductivity in Btu × ft^{-1} × hr^{-1} × $(R)^{-1}$

Temperature, R	660	1060	1460	1860	2260	2460
Conductivity	.0225	.0417	.0625	.0834	.121	.141

Titanium Structure

Density = 281 lb × ft^{-3}

Specific Heat = .14 Btu × lb^{-1} × $(R)^{-1}$

Thermal Conductivity = 5.0 Btu × ft^{-1} × hr^{-1} × $(R)^{-1}$

*Taken same as for Pyrocarb 400

Table 2-18. Mechanical Properties of C-C Truss Core Processed by Various Techniques

Process	ρ (g/cc)	Compression: Longitudinal F_{cu} (psi)	Compression: Longitudinal $E \times 10^{6}$ (psi)	Compression: Longitudinal $\epsilon_f \times 10^{-6}$ (in./in.)	Compression: Transverse F_{cu} (psi)	Compression: Flatwise F_{cu} (psi)	Flexure (Longitudinal) F_{cu} (psi)	Flexure (Longitudinal) $E \times 10^{-6}$ (psi)	Flexure (Longitudinal) $\epsilon_f \times 10^{-6}$ (in./in.)	Shear (Short Beam) F_{su} (psi)
long cycle CVD infiltration	1.51	10,100	2.37	4,400	9,450	388				
short cycle CVD infiltration	1.38	7,200	1.97	3,900	6,300	303				
impregnated (mandrels used before and during cure)	1.30	2,690	1.0	2,850	2,250	147				
impregnated (mandrels not used)	1.31	3,430	1.10	3,475	2,840	150				
pyrolyzed (skin warp parallel to flutes)	1.19	1,490	1.21	2,020	1,610	51				
fast carbonization + CVD infiltration	1.29	9,630	2.41	4,000	8,130	307				
fast carbonization/CVD infiltration	1.30	8,430	2.33	3,820	6,560	365				
impregnated (mandrels used before cure only)	1.18	1,940	1.0	2,850	1,520	110				
pyrolyzed (skin warp parallel to flutes)	1.19	2,230	1.62	1,740	1,730	38	2,470	1.48	1,870	1,234
pyrolyzed (skin warp perpendicular to flutes)	1.19	1,600	0.62	3,450	2,600	64	1,990	0.55	4,850	1,186

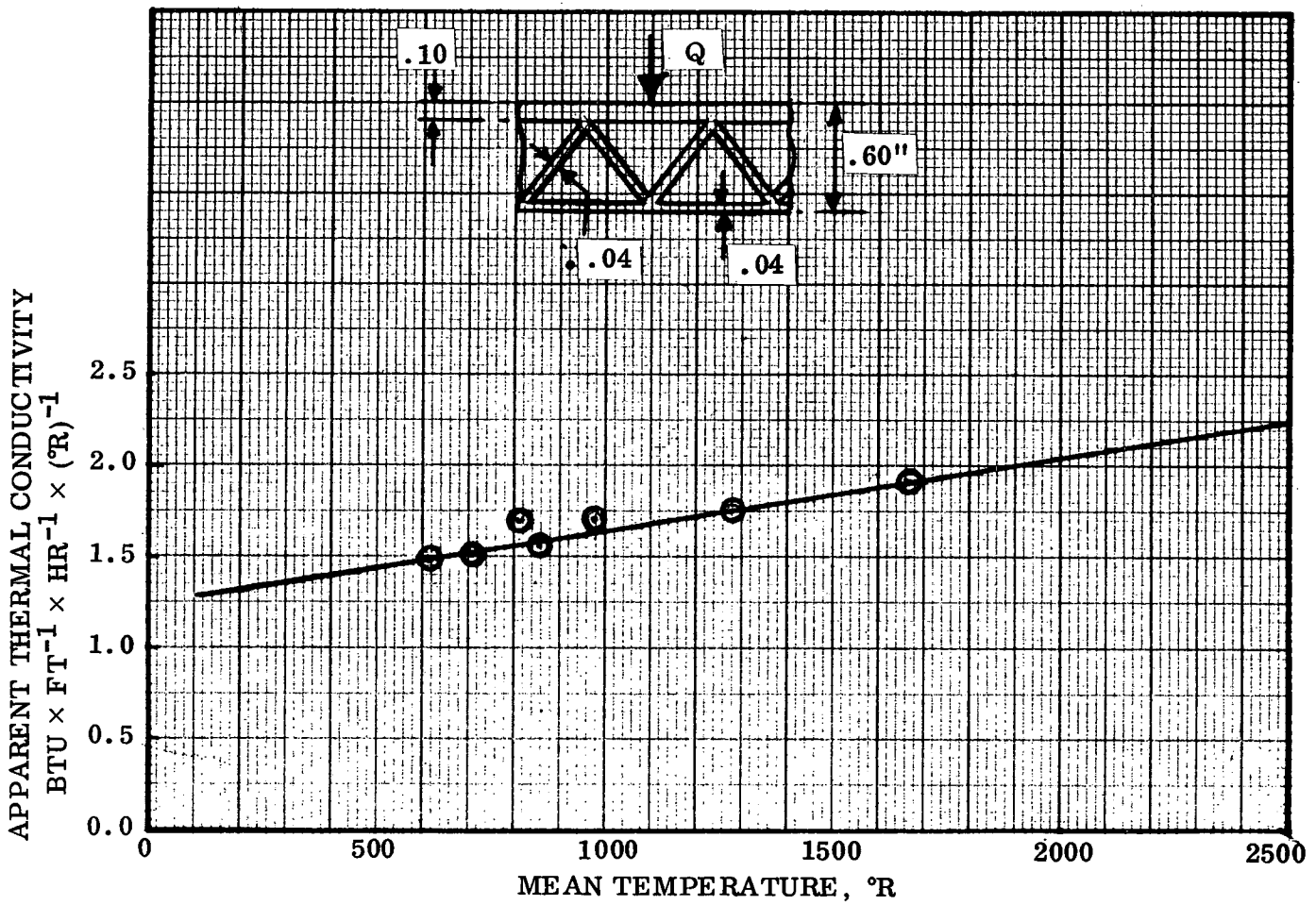

Figure 2-26. Apparent Thermal Conductivity of Carbon-Carbon Truss Core

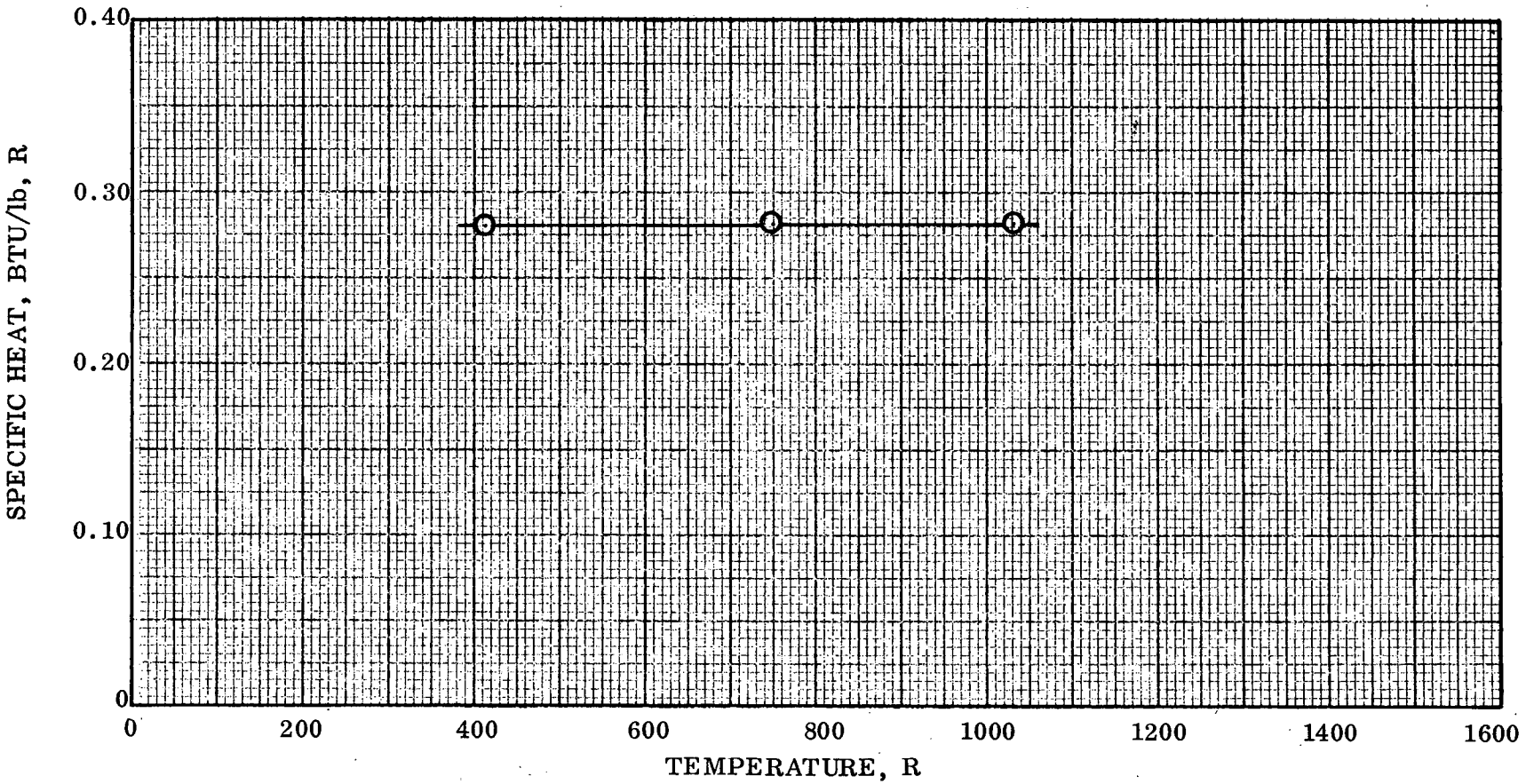

Figure 2-27. Specific Heat of Fiberglass Honeycomb

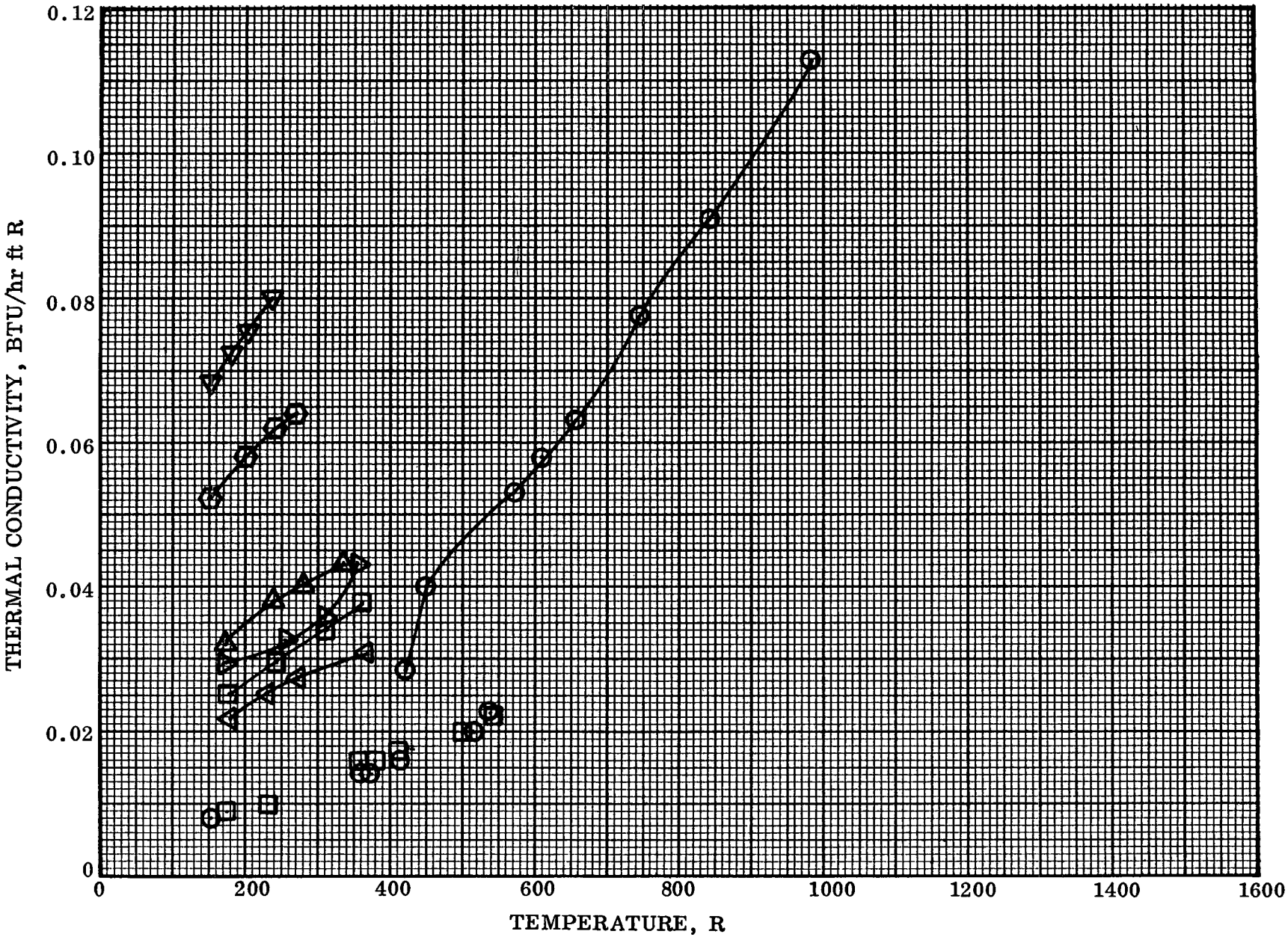

Figure 2-28. Thermal Conductivity of Fiberglass Honeycomb Sandwich Panels

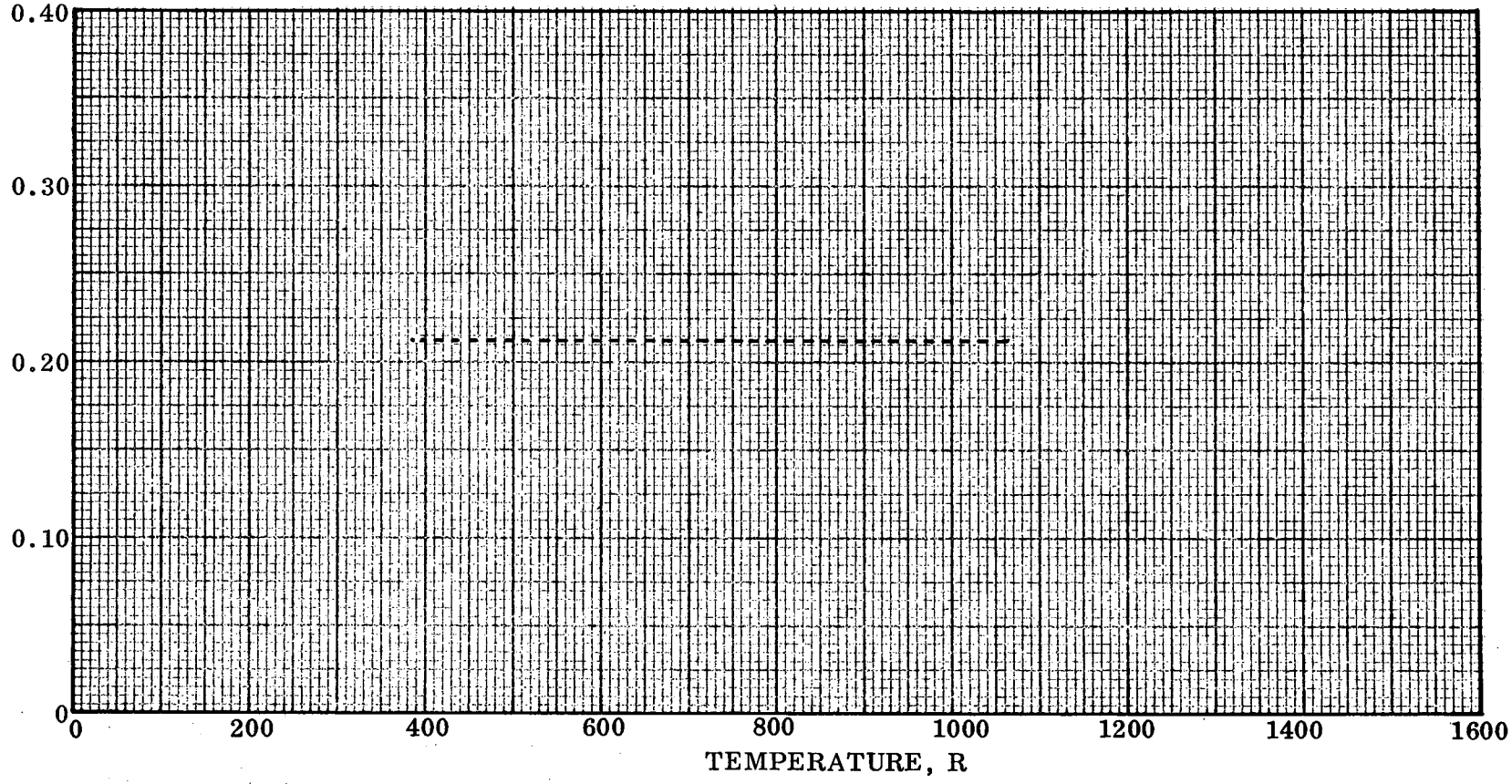

Figure 2-29. Specific Heat of Aluminum Honeycomb

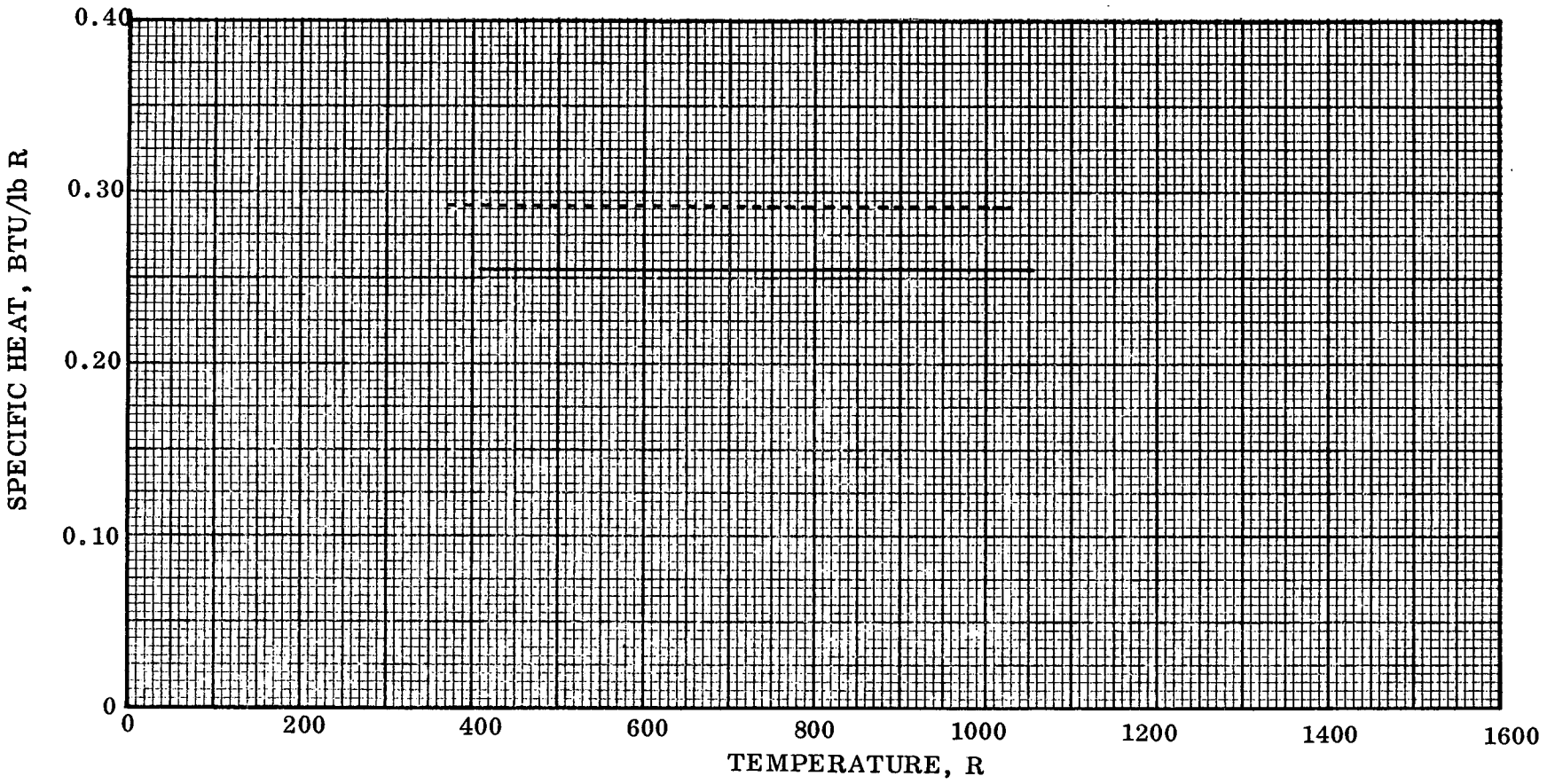

Figure 2-30. Specific Heat of Honeycomb Sandwich Panels Having Aluminum Core

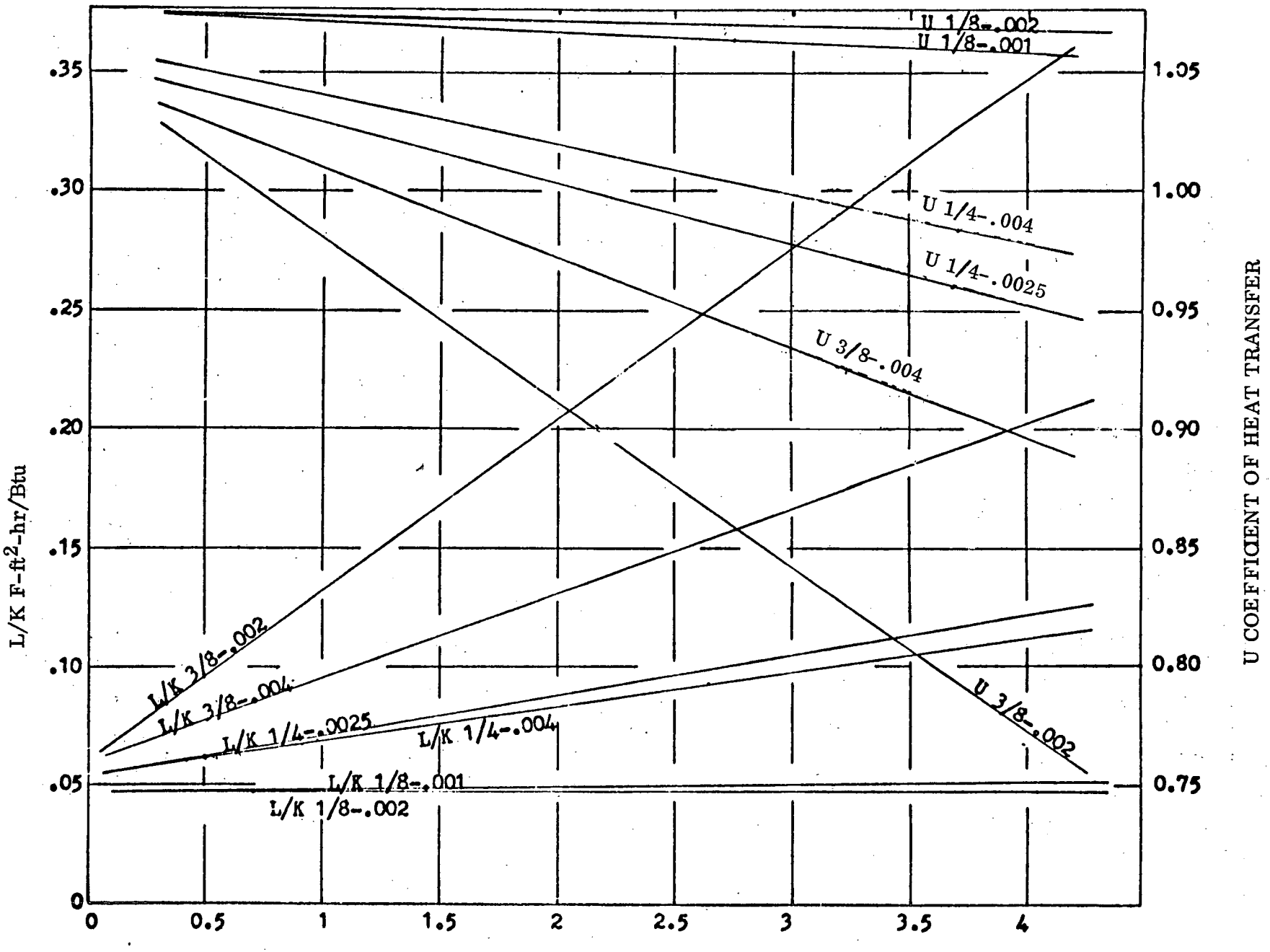

Figure 2-31. Thermal Conductivity of HEXCEL Panels

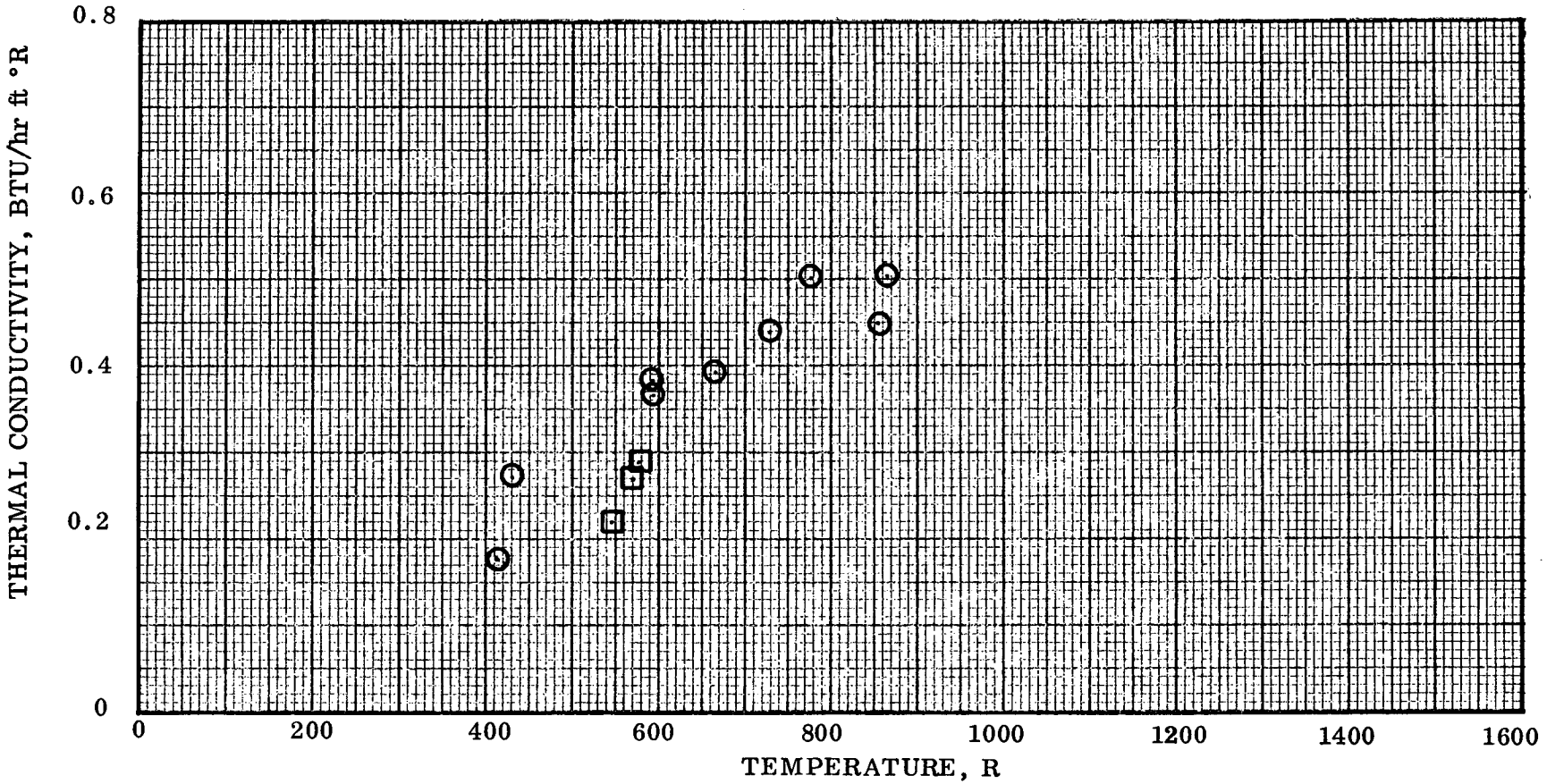

Figure 2-32. Thermal Conductivity of Aluminum Honeycomb Sandwich

Table 2-19. Specific Heat of Fiberglass Honeycomb

Sym.	Ref.	Range, R	Material Composition	Remarks
○	39	410 to 1035	Skin - Al 2024-T3; 0.020 in thick; Core - phenolic honeycomb (Brunswick-Balke Collender Co); 5/8 in thick; 1/9 in cell size; catalyst Agent A; 9 lb/cu ft; 0.6694 total thickness; resin content 54.4%.	C_p of core is 0.300 Btu/lb -R from 380 to 1040 R. Drop method; copper block calorimeter

Table 2-20. Thermal Conductivity of Fiberglass Honeycomb Sandwich Panels

Sym.	Ref.	Range, R	Material Composition	Remarks
○	40	154 to 534	One inch fiberglass honeycomb cells filled with CO_2-blown foam, polyester based polyurethane foam	Aged at even temp 1-3 mos. Atmos. pressure. Guarded twin hot plate.
□	40	174 to 540	One inch fiberglass honeycomb cells filled with CO_2-blown foam, polyester based polyurethane foam.	Same as above.
△	41	170 to 342	Faces: Outer 0.025 in. phenolic glasscloth laminate; inner 0.009 in. epoxycloth. Honeycomb: phenolic glasscloth 3/16 in.cell, 0.15 in. core. Fillers: air	Cold Temp.: -321F
⬡	41	156 to 270	Faces: Same as above. Honeycomb: Same as above. Fillers: Dry potassium titanate (DuPont)	Same as above
▽	41	154 to 242	Faces: Same as above. Honeycomb: Same as above. Fillers: Potassium titanate and epoxy mastic	Same as above
▷	41	172 to 358	Faces: Same as above. Honeycomb: Same as above. Fillers: Min-K 1301 (Johns-Manville)	Same as above
◁	41	178 to 368	Faces: Same as above. Honeycomb: Same as above. Fillers: Min-K 501 (Johns-Manville)	Same as above
◇	41	177 to 365	Faces: Same as above. Honeycomb: Same as above. Fillers: Polyurethane foam, 4 lb/ft^3	Same as above

Table 2-20. Continued

Sym.	Ref.	Range, R	Material Composition	Remarks
○	39	419 to 984	3 ply panel - Faces: 0.020 in. thick Al alloy 2024-T3; core: phenolic honeycomb by Brunswich-Balke Collender Co. (9 lb/cu ft); 1/9 in. cell size; Agent A catalyst; 5/8 in. core thickness; 0.67 in. total thickness; resin content 54.4% total weight.	Decomposition evident above 390F. Guarded twin plate.

Table 2-21. Specific Heat of Aluminum Honeycomb

Sym.	Ref.	Range, R	Material Composition	Remarks
--	39	380 to 1060	5/8 in. thick honeycomb panel of 0.020 in. Al alloy 2024-T3 with 1/4 in. cell size; 4.3 lb/ft^3.	Made by Brunswick-Balke Collender Co. Drop method copper block calorimeter.

Table 2-22. Specific Heat of Honeycomb Sandwich Panels Having Aluminum Core

Sym.	Ref.	Range, R	Material Composition	Remarks
——	39	410 to 1060	Aluminum alloy 2024-T3 honeycomb with 2024-T3 faces; 4.3 lb/ft^3	Made by Brunswick-Balke Collender Co. Drop method copper block calorimeter.
---	39	360 to 1030	Aluminum alloy 2024-T3 honeycomb with 181 Volan A polyester faces; 4.3 lb/ft^3	Same as above.

Table 2-23. Thermal Conductivity of Aluminum Honeycomb Sandwich

Sym.	Ref.	Range, R	Material Composition	Remarks
○	39	418 to 864	3 ply panel - Faces: 0.020 in. Al alloy 2024-T3; Core: 0.002 in. Al alloy 2024-T3 honeycomb (1/4 in. cell × 5/8 in. thick, density = 4.3 lbs/cu ft); Resin bonded (15.5% total wt); 0.66 in. total thickness.	Made by Brunswick-Balke Collender Co. Decomposition evident above 310F. Guarded twin plate method.
□	42	549 to 573	Faces: Two 0.008 in. Al 24 ST bonded with Elastomer-resin adhesive to Core: 1/4 in. cellular 0.0030 Al 3S-H19.	

2.1.6 AEROTHERMODYNAMIC ANALYSIS. The prediction of aerothermodynamic environment is based on the Convair Aerospace Computer Program P3020 (Ref. 14 and 15) and the recent recommendations of the NASA thermal panel on heat transfer methodology (Ref. 16). Figure 2-33 outlines the computational procedure. Using the Patrick AFB atmosphere, the freestream conditions are then established by the prediction of the flow field about simple geometric shapes such as flat plates, wedges, cones, cylinders, or spheres. Cross-flow theory is then applied to correct the three-dimensional effects.

Prediction of flow field is classified into two regimes: high and low local angle of attack. For low angle of attack, the shock waves are assumed attached to the body, and flow properties are computed from tangent wedge/cone techniques. At high angles of attack, the flow field cannot be predicted so conveniently as at low angles of attack because of shock detachment. Thus, approximate methods are used.

Computation of local heating rates is classified into three regimes: laminar, turbulent and transitional boundary layer. For the laminar boundary, the Blasius solution is evaluated at the Eckert reference enthalpy, and heat transfer is computed from Colburn's statement of Reynolds analogy. For turbulent flow, two techniques are presented; the first utilizes skin friction predicted by the Schultz-Grunow equation evaluated at Eckert's reference enthalpy, with Colburn's Reynolds analogy, and the second is the Spalding-Chi skin friction and von Karman's Reynolds analogy. Masek's criterion is used to predict the onset of transition. Transitional heating between the laminar and turbulent boundary layers is then calculated as a linear interpolation of turbulent and laminar heating values, the degree of turbulence depending on the "turbulent fraction" exhibited by the boundary layer with respect to values of Reynolds number for transition onset and end. The virtual origin for turbulent flow can be taken as either the leading edge or the beginning of transition. Swept cylinder theories of Fay-Riddell (laminar) and Beckwith-Gallagher (turbulent) are used to compute heating rates on leading edges and for bodies at high angle of attack.

Flow Field Calculations

The effective angle of attack, ψ, is defined as the scalar product of the direction cosines of the normal to the surface and of the velocity vector. Using Figure 2-34 these are

x, y, z direction cosines of normal to surface

$$DNX = \sin\theta,\ DNY = -\cos\theta\cos\phi,\ DNZ = -\cos\theta\sin\phi$$

x, y, z direction cosines of velocity vector

$$Vx = V\cos\alpha\cos\beta,\ V_Z = V\sin\alpha\cos\beta$$

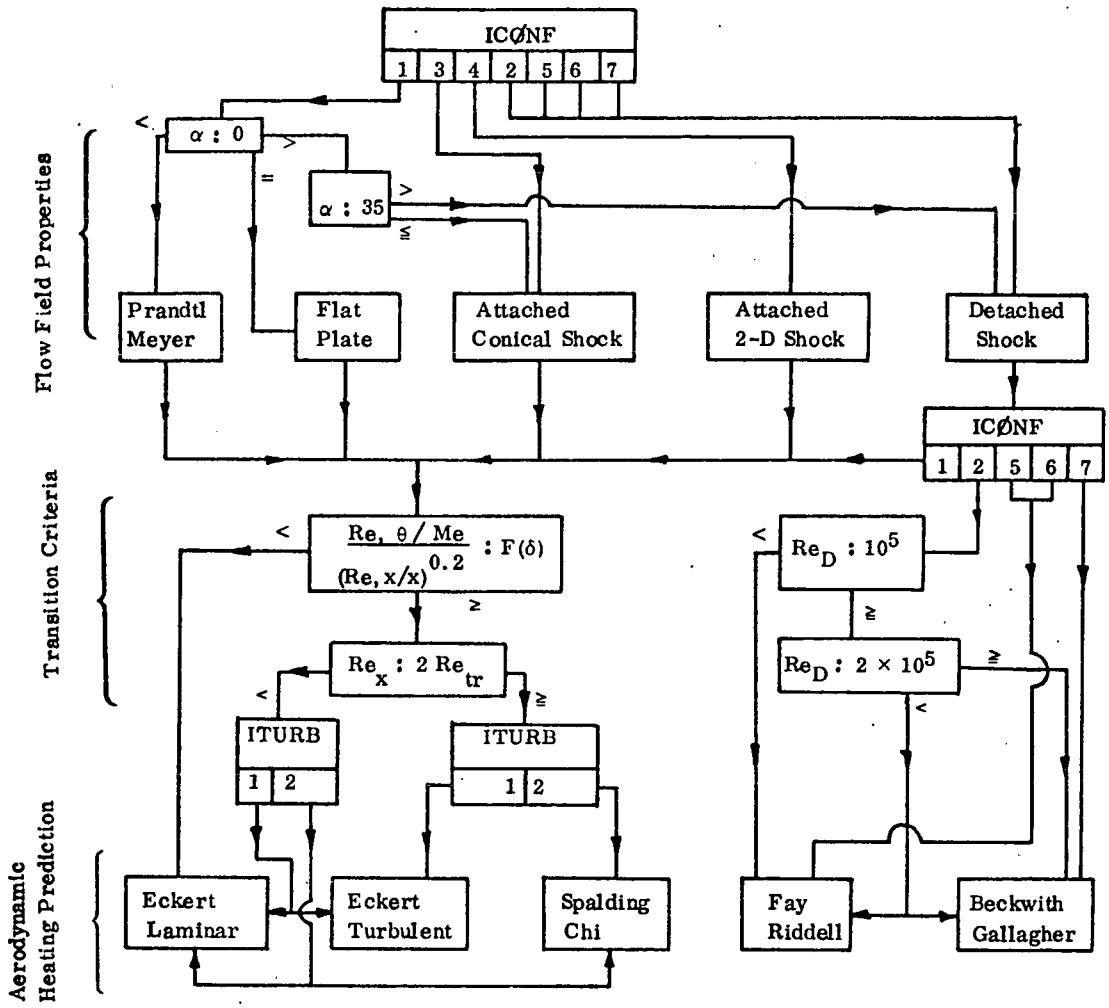

ICØNF = 1 Flat Plate With Cross Flow
2 Cylinders
3 Cone
4 Wedge
5 Sphere
6 Laminar Cylinder
7 Turbulent Cylinder

Figure 2-33. Aerodynamic Heating Prediction

Then, the scalar product is

$$\sin \psi = DNX \cos \alpha \cos \beta + DNY \sin \beta + DNZ \cos \beta \sin \alpha \qquad (2\text{-}23)$$

where

α = angle of attack

β = yaw angle

Thus, body orientation can be described simply as a function of these two angles.

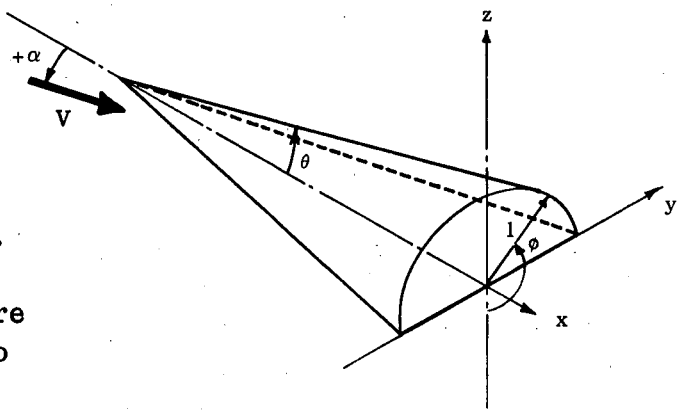

Figure 2-34. Body Orientation

The expressions for the inviscid pressure over half-pointed cones are applicable to other types of geometry (such as a half elliptical cone) if the geometric angles θ and ϕ at any locations are defined similarly to those of the half cone. This implies the use of the same axis of symmetry with respect to the centerline. The body local angle of attack, ψ, for a semi-cylinder is obtained by setting $\theta = 0$ in the equation of ψ for a semi-cone.

The thermodynamic properties of the air ahead of the shock, P_∞, T_∞, and ρ_∞ and the free stream Mach number M_∞, are determined from the given flight conditions using the 1963 Patrick AFB atmosphere.

a. Low Angle of Attack. A set of empirical equations (Reference 17) is used in determining the shock layer thermodynamic properties at the boundary layer edge as functions of the hypersonic similarity parameters $M_\infty \sin \alpha$ (Reference 18). For the flat plate configuration, $\alpha = 0$, it is assumed that the freestream conditions exist at the boundary layer edge.

b. High Angle of Attack. At high angle of attack the pressure is calculated by the modified Newtonian flow theory, which is expressed as

$$\frac{P_e}{P_\infty} = 1 + \frac{\gamma}{2} M_\infty^2 C_{P_{max}} \sin^2 \psi \qquad (2\text{-}24)$$

where

$$C_{P_{max}} = \frac{\gamma + 3}{\gamma + 1} \left[1 - \frac{2}{(\gamma + 3) M_\infty^2} \right]$$

When the attached shock properties break down at high angles of attack, an empirical equation based on data of Bertram and Henderson (Ref. 19) is used to compute the shock angle as shown in Figure 2-35.

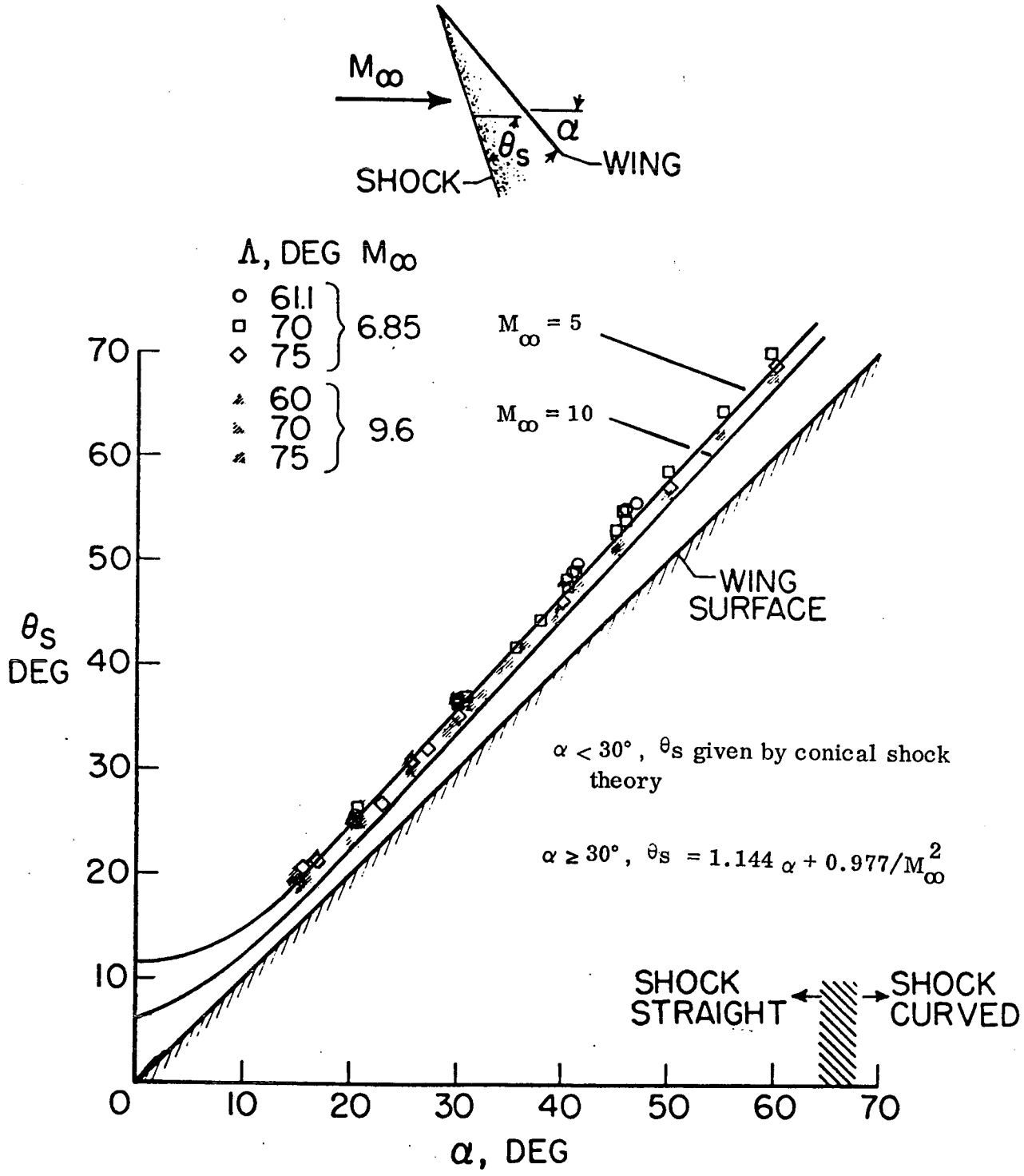

Figure 2-35. Effect of Mach Number on Shock Angle for Flat Delta Wings

Once the shock angle is known, the conditions downstream of the shock wave can be computed from the oblique shock relations using the upstream conditions. The governing equations are simply the normal momentum and energy equations

$$P_2 = P_1 + \rho_1 V_{1n}^2 (1 - x) \qquad (2\text{-}25)$$

$$i_2 = i_1 + \frac{1}{2} V_{1n}^2 (1 - x^2) \qquad (2\text{-}26)$$

where $x = \rho_1/\rho_2$ and the continuity equation has been eliminated from the original set of equations. The subscripts 1 and 2 denote conditions up and downstream of the shock.

At low freestreem stagnation enthalpies ($i < 705$ Btu/lb_m), from the perfect gas law, the stagnation pressure after an oblique shock, P_s, is

$$\frac{P_s}{P_o} = \left[\frac{6M_\infty^2 \sin^2 \delta}{M_\infty^2 \sin^2 \delta + 5}\right]^{3.5} \left[\frac{6}{7M_\infty^2 \sin^2 \delta - 1}\right]^{2.5} \qquad (2\text{-}27)$$

At high freestream enthalpies, real gas effects are important, and Mollier chart of equilibrium air (Ref. 20) is used. Equations 2-25 and 2-26 are solved iteratively together with the equation of state $\rho = \rho\ (i,\ P)$.

Aerodynamic Heating

Aerodynamic heating rates are computed in two combinations:

Eckert laminar with Eckert turbulent
Eckert laminar with Spalding-Chi turbulent

The Eckert reference enthalpy method (Reference 21) depends upon the assumption that the incompressible mass, momentum, and energy equations can be used for compressible flow solutions provided the thermodynamic and transport properties of the gas are known and are evaluated at an appropriate reference enthalpy. Real gas effects, including dissociation, are taken into account in the determination of the properties of the gas just outside the boundary layer. The Eckert reference enthalpy is

$$i^* = i_e + 0.5\ (i_w - i_e) + 0.22\ (i_r - i_e) \qquad (2\text{-}28)$$

where i_e is the shock layer (just outside the boundary layer) static enthalpy, i_w is the enthalpy of air at the wall temperature, and i_r is the boundary layer recovery enthalpy, given by

$$i_r = i_e + r \frac{V_e^2}{2gJ} \qquad (2\text{-}29)$$

where the flow recovery factor, r is 0.84 for laminar flow and 0.89 for turbulent flow.

The shearing stress at the wall is given by

$$\tau_w = \frac{C_f}{2} \rho V_e^2 \tag{2-30}$$

where C_f is the skin friction coefficient. In the following sections, methods of computing C_f will be described. The convective heat transfer is given by

$$q = h (i_e - i_w) \tag{2-31}$$

The heat transfer coefficient is obtained from the Stanton number

$$h = \rho V_e St \tag{2-32}$$

The Reynolds analogy relation is used to obtain Stanton number

$$St = C_f/2 Pr^{*2/3} \tag{2-33}$$

where the Prandtl number

$$Pr^* = \frac{\mu^* C_p^*}{K^*} \tag{2-34}$$

A constant value of 0.71 is assumed for Pr*, based on the data of Hansen (Reference 22).

a. Laminar Boundary Layer. The Blasius solution for an incompressible laminar boundary layer gives a skin friction coefficient

$$C_f = 0.664/\sqrt{Re^*} \tag{2-35}$$

where Reynolds number is

$$Re^* = \frac{\rho^* V_e X}{\mu^*} \tag{2-36}$$

yields the laminar heat transfer coefficient

$$h = \frac{13.43 \sqrt{\rho^* \mu^* V_e}}{\sqrt{X}} \tag{2-37}$$

b. Turbulent Boundary Layer. The Schultz-Grunow solution for the local skin friction coefficient is (Reference 23)

$$C_f = \frac{7.485 \rho^* V_e}{(\log Re^*)^{2.584}} \tag{2-38}$$

The Spalding-Chi (Ref. 24) method was based upon incompressible skin friction relationships. Transformation from incompressible to compressible cases was

postulated upon previously successful transformations of Van Driest and others. These transformations were evaluated by obtaining constants with the least squares deviation from a wide variety of experimental data. Equations used in this analysis stem from curve fits to the Spalding-Chi values developed by Komar (Reference 25). In this manner, successive solutions of the equations

$$F_c = \left\{ \frac{1}{\sqrt{-c}} \left(\sin^{-1} \left[\frac{-(2c + b)}{\sqrt{b^2 - 4ac}} \right] - \sin^{-1} \left[\frac{-b}{\sqrt{b^2 - 4ac}} \right] \right) \right\}^{-2} \qquad (2\text{-}39)$$

$$F_{r\theta} = \left[\frac{i_w}{i_e} \right]^{-0.702} \left[\frac{i_{aw}}{i_w} \right]^{0.72} \qquad (2\text{-}40)$$

$$F_{rx} = F_{r\theta} / F_c \qquad (2\text{-}41)$$

$$A = \log_e (F_{rx} \, Re_x) \qquad (2\text{-}42)$$

$$C_f \, F_c = \exp \left[\sum_{j=1}^{n} g_j \, A^{j-1} \right] \qquad (2\text{-}43)$$

where

$$a = i_w / i_e \qquad b = 1 + \frac{r}{2} (\gamma - 1) \, M_e^2 - \frac{i_w}{i_e} \qquad c = -\frac{r}{2} (\gamma - 1) \, M_e^2 \qquad (2\text{-}44)$$

The coefficients g_j are those developed by Komar for the curve fits.

Reynolds analogy is then used to obtain the heating coefficient. A recommended equation for the Reynolds analogy factor is that of Karman as proposed by Bertram (Reference 26).

$$S = 1 + 5 \sqrt{(F_c \, c_f)/2} \left[Pr - 1 + \log \frac{5 \, Pr + 1}{6} \right] \qquad (2\text{-}45)$$

c. Cross-flow and Transition Boundary Layer. At vehicle angles of attack greater than twenty degrees, for body shapes of the type associated with lifting entry, streamline divergence, or cross-flow, thins the boundary layer and increases heat transfer. Two dimensional flow assumptions, ie, strip theory, do not account for this three-dimensionality and therefore underpredict observed heat transfer. Approximate methods have been developed for estimating the influence of flow divergence. These methods are described by Young in Reference 27. Since cross-flow also causes a reduction in boundary layer momentum thickness, it must be included in any transition correlation involving this parameter.

For a slab of width D, the velocity gradient along the center line is defined by the relation

$$f_2 = \frac{D}{V_e}\left.\frac{dU}{dy}\right]_{y=0} = \left[0.745 + 3.14\frac{r}{D}\right]\left[\frac{\gamma-1}{2}\right]^{1/2}\tan\psi \qquad (2\text{-}46)$$

The ratios of heating rate with cross-flow to that from strip theory are

$$\left.\frac{q_{CF}}{q_s}\right]_L = \left[\frac{2A}{1-e^{-2A}}\right]^{1/2} \qquad (2\text{-}47)$$

$$\left.\frac{q_{CF}}{q_s}\right]_T = \left[\frac{A}{1-e^{A}}\right]^{1/5} \qquad (2\text{-}48)$$

where

$$A = f_2\,\frac{X}{D}$$

and the ratio of momentum thickness for a slab including cross-flow to that for strip theory is

$$\frac{\theta_{CF}}{\theta_S} = \left[\frac{1-e^{-2A}}{A}\right]^{1/2} \qquad (2\text{-}49)$$

An interim transition criterion has been proposed by Masek (Reference 28). The value of the transition criterion at which transition onset occurs is a function of flow deflection angle as shown in Figure 2-36. The criterion can be expressed as

$$\frac{Re_\theta/M_e}{(Re_x/X)^{.2}} = f(\psi) \qquad (2\text{-}50)$$

All quantities are based upon local boundary layer edge properties where local Reynolds number and momentum thickness Reynolds number are

$$Re_x = \frac{\rho_e V_e X}{\mu_e} \qquad (2\text{-}51)$$

and

$$Re_\theta = \frac{Re_x}{X}\,\theta \qquad (2\text{-}52)$$

The momentum thickness is given by

$$\theta = \frac{.664X}{(Re_x)^{1/2}}\sqrt{\frac{\rho^*\mu^*}{\rho_e\mu_e}}\cdot\frac{\theta_{CF}}{\theta_s} \qquad (2\text{-}53)$$

where ρ^*, μ^* are evaluated at Eckert's reference enthalpy.

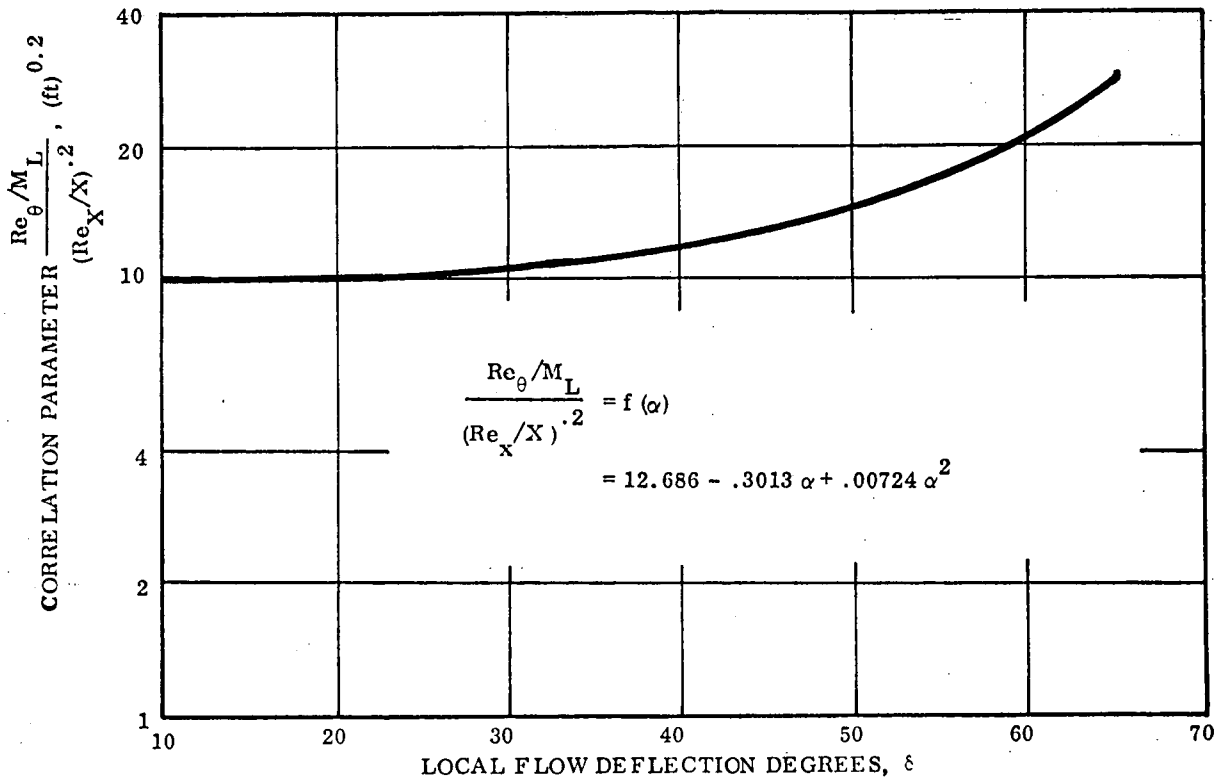

Figure 2-36. Correlation Parameter

The transitional boundary layer is represented as a linear transition from laminar into turbulent flow. Transition is assumed to begin at a calculated value of the shock layer Reynolds number, Re_{tr}, and end at a calculated value of the shock layer Reynolds number, denoted Re_E. The heating rate is computed as the linear interpolation between laminar and turbulent values, the virtual origin of both being the leading edge. Interpolation is performed using the value of Reynolds number that occurs between the calculated values specifying the onset and end of transition. Hence, for example, the heat transfer coefficient is given by

$$h = \frac{Re - Re_{tr}}{Re_E - Re_{tr}} h_T + \left[1 - \frac{Re - Re_{tr}}{Re_E - Re_{tr}}\right] h_L = f_T h_T + f_L h_L \qquad (2\text{-}54)$$

The value of Re_{tr} can be determined by Equation 2-50 and experimentally, one observes (Reference 29)

$$f_{tr} = \frac{Re_E}{Re_{tr}} = 2 \qquad (2\text{-}55)$$

d. Sphere and Cylinder Heating. For leading edges or at high angle of attack, swept cylinder theories are used to predict the aerodynamic heating. For laminar flow, heating is computed by method of Fay and Riddel (Reference 30), while the method of Beckwith and Gallagher (Reference 31) is used to compute the turbulent heating.

Bushnell (Reference 32) suggests the use of a simple transition criterion for leading edges at all sweeps which is based upon freestream Reynolds number and the leading edge diameter as the characteristic length. Based upon Bushnell's and other's data and since fin and wing leading edges of the shuttle will have end effects, the onset of transition is taken as $R_{\infty,D} = 0.1 \times 10^6$, and fully turbulent flow occurs as $Re_{\infty,\ D} = 0.2 \times 10^6$.

Laminar heat transfer to a swept cylinder is computed through a transformation of spherical heating rates. Heat transfer to a sphere is calculated by the Fay-Riddell (Reference 30) expression

$$q_{sph} = 30.25\ (\rho_w \mu_w)^{0.1}\ (\rho_s \mu_s)^{0.4}\ (dV/dX)_s^{0.5}\ (i_s - i_w) \tag{2-56}$$

where

$$\left[\frac{dV}{dX}\right]_s = \frac{2}{D}\left[\frac{2\ (P_s - P_\infty)}{\rho_s}\right]^{1/2} \tag{2-57}$$

Cylindrical heating rates are then obtained by adjusting for sweep by

$$q_{cyl} = 0.75\ q_{sph}\ (\cos \Lambda)^{1.2} \tag{2-58}$$

where the sweep angle $\Lambda = 90° - \psi$.

Turbulent heat transfer to a cylinder is computed by the method of Beckwith and Gallagher (Reference 31). The equation for heat transfer to the stagnation line of a swept cylinder is

$$\frac{h_s D}{K_o} = Pr^{1/3}\left[\frac{\rho_o V_\infty D}{\mu_o}\right]^{n/(1+n)}\left[a\frac{\mu_r \rho_r}{\mu_o \rho_o}\right]^{n/(1+n)}\left[\sin \Lambda\right]^{(n-1)/(n+1)}$$

$$\left[\frac{49}{376}\ \cos \Lambda \frac{D}{u_\infty}\left(\frac{dV_n}{dx}\right)_s\right]^{n/(1+n)} \tag{2-59}$$

where $Pr = 0.71$, a and n are constant in the Blasius skin friction law and were taken as $a = 0.0228$ and $n = 4$. V_n is the component of V_∞ normal to the cylinder stagnation line; thus $V_n = V_\infty (\cos \Lambda)$.

The heat transfer to the stagnation line is then

$$q_{cyl} = 1.30622\left[\frac{V_\infty \sin \Lambda}{\mu_o}\right]^{3/5}\left[\frac{\rho_r}{\mu_r}\right]^{4/5}\left[\frac{dV}{dX}\right]_s^{1/5}\left[i_r - i_w\right] \tag{2-60}$$

Reference conditions ρ_r and μ_r are evaluated at stagnation conditions after the shock, (Ps, Ts), where values of recovery factor used in evaluating i_r are obtained by curve fit of the data in Beckwith and Gallagher (Reference 31).

The methods of Bertram and Henderson (Reference 19) are used to correct the flat face velocity gradients (Figure 2-37). Since stagnation heating is proportional to free stream velocity gradient, it was postulated that

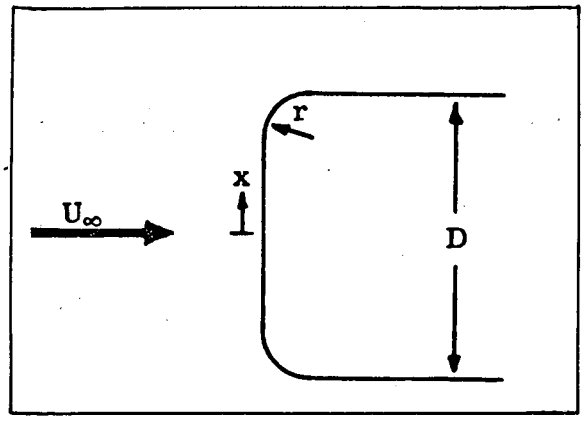

Figure 2-37. Geometry of Flat Face Velocity Gradient Correction

$$\frac{q_{flat}}{q_{cyl}} = \sqrt{\frac{\left.\frac{dV_e}{dx}\right|_{x=0}^{flat}}{\left.\frac{dV_e}{dx}\right|_{x=0}^{cyl}}} \qquad (2\text{-}61)$$

For the laminar boundary layer of a flat disc

$$\left[\frac{dV_e}{dx}\right]_{x=0} = 0.745 + 3.14\left[\frac{r}{D}\right] \qquad (2\text{-}62)$$

the laminar centerline heating rates are of the form

$$q_{flat} = q_{cyl}\sqrt{\frac{0.745 + 3.14\,(r/D)}{2.315}} \qquad (2\text{-}63)$$

For turbulent boundary layer a 1/5 power correction is used, i.e.,

$$q_{flat} = q_{cyl}\left[\frac{0.745 + 3.14\,(r/D)}{2.315}\right]^{1/5} \qquad (2\text{-}64)$$

e. Heat Distribution on Peripheral Locations. Lees (Reference 33) solution modified by Bertram and Everhart (Reference 34) is used to calculate the distribution of heating rates for various peripheral locations. If the peripheral pressure distribution over a body is assumed to be represented by an equation of the form

$$p/p_o = \cos^2\phi + b\sin^2\phi + c\,\phi^n \qquad (2\text{-}65)$$

the ratio of heat transfer coefficients at the peripheral location to the stagnation line is

$$\frac{h}{h_o} = \frac{\sqrt{2}\,[1 - (1\text{-}b)\sin^2\phi + C\phi^n]\,\phi}{\left[(1\text{-}b)(\beta\sin 2\phi - \sin^2\phi) + \phi^2\left(\frac{4C}{n+2}\phi^n + 1 + b\right)\right]^{1/2}} \qquad (2\text{-}66)$$

According to the Newtonian approximation adopted by Lees, $b = (\gamma M_\infty^2)^{-1}$ and $c = 0$. However, the values of b, c, and n which accurately represented the pressure distribution on a cylinder for $M_\infty \geq 4$ were found to be $b = 0.16$, $c = -0.00665$, $n = 5$ for $0 < \theta = 90°$.

Thermodynamic and Transport Properties

The perfect gas law is used for air at low temperatures, and the enthalpy of air is obtained from an empirical equation as shown in Figure 2-38. At high temperature a Mollier chart (Reference 20) is used.

A constant value of 0.71 is assumed for Prandtl number, based on the data of Hansen (Reference 22). The viscosity of air is calculated by equation of Hansen and Heims (Reference 35) which is in the form

$$\frac{\mu}{\mu_o} = \left[1 + 0.023A\left(1 + \tanh\frac{A(1-\frac{1}{8}B) - 6.5}{1.5+\frac{1}{8}B}\right)\right]\left[1 - \exp\frac{A - 14.5 - 1.5B}{0.9 + 0.1B}\right] \quad (2\text{-}67)$$

where

A = T/1800

B = log (P/Po)

T is temperature in degrees Rankine

P, Po are local pressure and one atmosphere pressure respectively

μ_o takes Sutherland's value, i.e.,

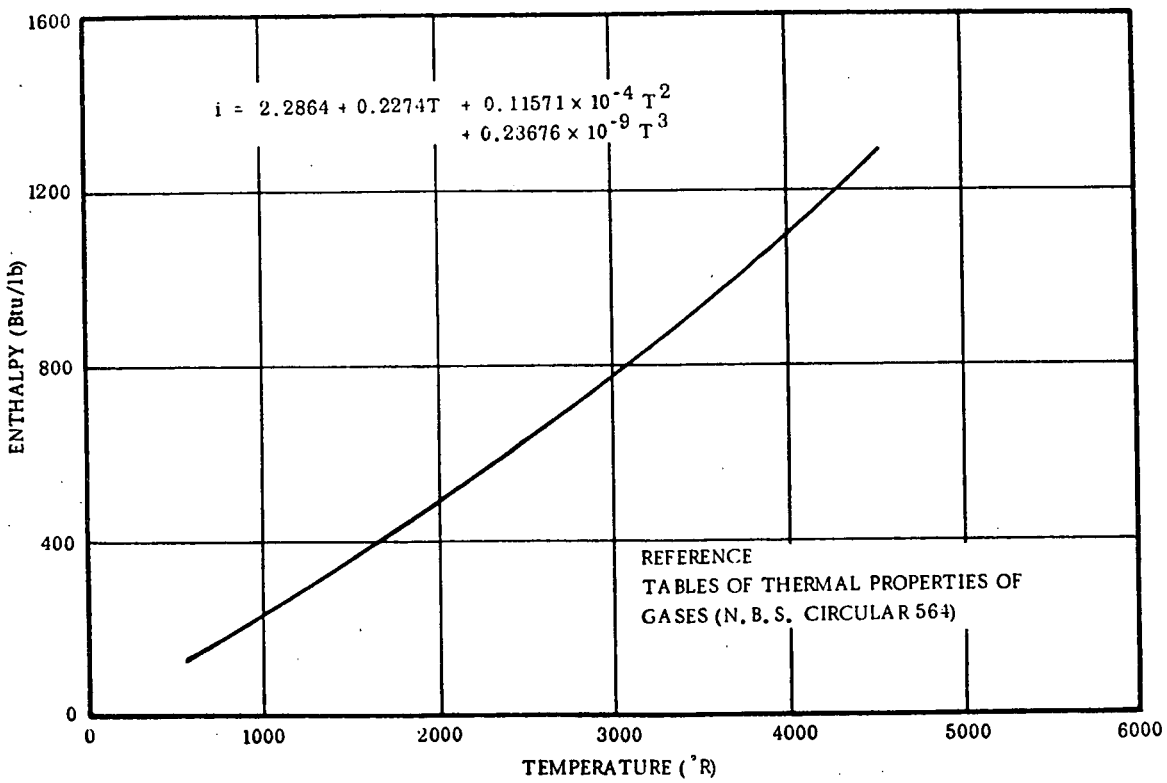

Figure 2-38. Enthalpy Versus Temperature for Air

$$\mu_o = 2.27 \times 10^{-8} \frac{(T)^{3/2}}{T + 198.6} \qquad (2\text{-}68)$$

2.2 ADDITIONAL TPS DESIGNS

The capability of treating a number of alternate TPS concepts was added to the existing TPS sizing routine. These included the passive systems of Reusable Surface Insulation (RSI), the carbon-carbon systems including a new leading edge concept as well as the configurations available for the flat panel metallic systems, and a heat sink system which incorporates either a change of phase or change of state in a material embedded in the honeycomb substrate which supports the RSI. The only active cooling concept considered was the charring ablator.

Of the new systems investigated, the most difficult task by far to accomplish was the stress analysis required for the RSI. Because of the large deformation of the glue line, a finite element stress analysis had to be shortened and streamlined to allow its use in an already massive computer code. In addition, a discrete element stress analysis on the same system had to be developed and utilized just to find the design point at which the finite element analysis could be used. The next most difficult task was the temperature description of the ablator. Fortunately, a charring ablator code was available to be adapted into the TPS sizing analysis. Simply by suppressing the chemical reactions of the ablator, a one-dimensional heat transfer analysis could be employed for the RSI system both with and without the phase change material (PCM). The PCM itself was described simply by performing an energy balance on the substrate to determine when enough heat had entered this region of the system to support either a change of phase or a change of state. Material properties were then adjusted accordingly. Finally, a thermodynamic model was developed to describe the carbon-carbon leading edge. The following paragraphs describe the mathematical models of the new TPS's.

2.2.1 PASSIVE COOLING SYSTEMS

2.2.1.1 Reusable Surface Insulation (RSI)

Thermal Analysis

No new programming was required to perform the thermal analysis of RSI. This is accomplished using the ablator routine by inputting the appropriate RSI thermal properties (ie, thermal conductivity, specific heat, etc), and fictitious ablation parameters to suppress the chemical reactions and pyrolosis.

Stress Analysis

The stress analysis of the RSI TPS is performed by two separate routines. The first, already developed within the framework of analyses existing in the TPS sizing driver program, describes by discrete element analysis the stress produced within an isolated section of a simply supported beam. The loadings considered are bending due to

external aerodynamic pressure and internal forces due to temperature gradients. The discrete element analysis is performed throughout the trajectory at time increments dictated by the program user. A number of structural indices are calculated at each time step, and the critical design point of the system is identified as that trajectory point exhibiting the minimum design indices. At this time, the second stress analysis is performed; here, a finite element analysis adopted from an existing independent program is applied. The RSI panel cross-section is subdivided into a group of bars and panels simulating the behavior of the RSI, its coating and underlying bond and the honeycomb substrate. The advantages of the finite element analysis are that it considers axial, bending, shear, and normal deformation of the panel and RSI as well as the shear and normal deformation of the bond. However, within the constraints of a fast and inexpensive computer program, it is not economically feasible to perform the finite element stress analysis throughout the trajectory. Hence, at least initially, this procedure will be employed only at the design point of the trajectory.

During the stress analysis of the program, the following functions are performed. At the first call for the stress analysis, subroutine PANEL divides the RSI/bond/substrate configuration into a predetermined number of discrete elements. The areas and location of these elements are computed as well as the appropriate moments of inertia. Once these geometric parameters are determined, there is no need for them to be repeated each time step; the values are stored for future use. At each time step, nodal temperatures for the discrete element stress analysis are interpolated from the thermodynamic analysis and stored. Next, thermal and mechanical stresses are computed. The stress model is comprised of five different components: (1) the face sheets of the honeycomb substrate, (2) the core of the substrate, (3) the bond material, (4) the RSI, and (5) the coating which is considered to cover only the top of the TPS. Inherent in this assumption is the neglect of edge effects of the coating around the edges (perpendicular faces) of the RSI tiles. Material properties are evaluated at the nodal temperatures and include the ultimate tension, compression, and shear strengths, the modulus of elasticity, the coefficient of thermal expansion, the modulus of rigidity, and Poisson's ratio for the bond material. Some modifications had to be made to the existing stress analysis since the original dealt with only a single material. A sketch of the nodal breakdown for the five different materials is given in Figure 2-39. Once the stresses are computed for the nodes of the model, a comparison is made to the applicable allowable values. The design factors or margins of safety are presented in Table 2-24. These are computed throughout the trajectory and stored for investigation at the trajectory end. The design point is then identified by the minimum design factors.

At this point in the computer program, the finite element stress analysis is performed. It is used primarily as a check of the design point which has been located by the more economical discrete element method.

Finite Element Stress Analysis General Theory

This section presents the general theory for determining displacements and stresses in the two-dimensional structure used to simulate the RSI behavior by the finite element stress analysis.

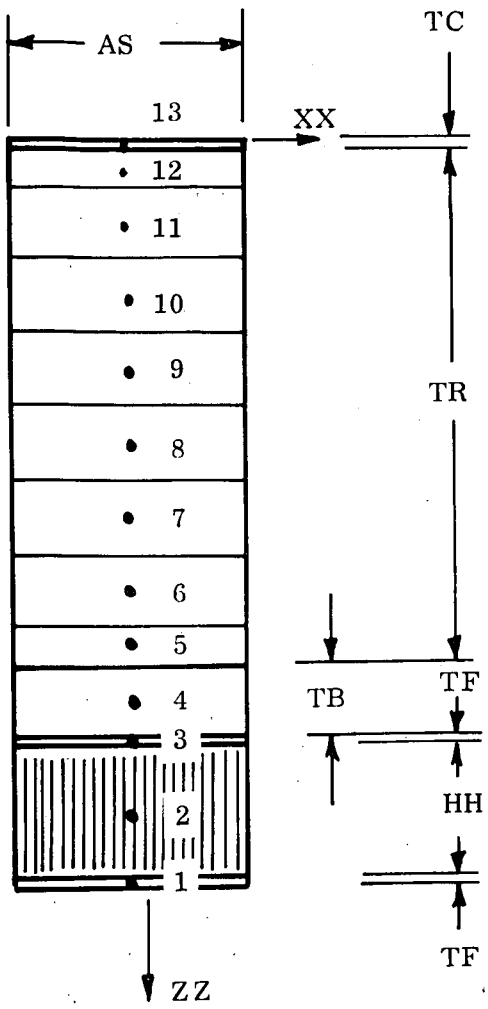

Figure 2-39. Discrete Element Stress Analysis Nodal Schematic

The method is based upon Castigliano's Theorem of Equilibrium (Reference 36). Finite differences are developed for the partial derivatives, and the resulting equations which relate forces and displacements are written in matrix form for automatic digital solution. The program output is internal loads and point displacements.

The development is presented in two sections:

a. An orthogonal stiffener grid

b. Thermal stress considerations

This procedure is advantageous because it yields separate routines for the simpler (and more commonly encountered) cases, and thus saves computing machine time.

The general development requires four steps:

1. Obtain a statement for strain energy at a typical point in the structure.
2. Apply the Energy Theorem.
3. Express the results of the preceding steps in matrix form.
4. Present the problem in a proper form for use by a digital computer.

The last two steps offer considerable latitude in procedure and have been tailored to suit existing computing equipment and programs.

Development of the Theorem

Castigliano's Theorem of Equilibrium states, "If the strain energy of any elastic structure is expressed in terms of the displacements of a number of points of the structure, then the differential coefficient of the expression with respect to the displacement of one of the points gives the component force acting at that point in the direction of the displacement." If u and w are displacements in the x and z directions at a point (m, n), then

$$\frac{\partial U}{\partial u_{m,n}} = F_{x_{m,n}} \quad \text{and} \quad \frac{\partial U}{\partial w_{m,n}} = F_{z_{m,n}} \tag{2-69}$$

Table 2-24. Design Factors

1 Elements	2 I	3 Failure Mode	4 Stress Ratio	5 Max Ratio	6 Critical Element	7 Critical Time	8 Margin of Safety
Face Sheets	1 & 3	Tension	$R_1=\frac{FX}{FTU(I,N)}$	R11M	I11	N11	MSFT =1./(R11M*UF)-1.
		Compression	$R_2=\frac{-FX}{FCY(I,N)}$	R12M	I12	N12	MSFC =FCR/(R2M*FCY (N2,N12)-1.
Honeycomb Core	2	Shear	$R_2=\frac{CRFS}{FSU(I,N)}$	R23M	2	N23	MSHS=-1/(R23M*UF)-1.
Bond	4	Shear Tension	$R_3=\frac{SUMPX}{FSU(I,N)}$	R33M	4	N33	
RSI	5 to 12	Tension	$R_1=\frac{FX}{FTU(I,N)}$	R41M	I41	N41	MSIT=1./(R41M*UF)-1.
		Compression	$R_2=\frac{-FX}{FCU(I,N)}$	R42M	I42	N42	MSIC=1./(R42M*UF)-1.
Coating	13	Tension	$R_1=\frac{FX}{FRU(I,N)}$	R51M	I51	N51	MSCT=1./(R51M*UF)-1.
		Compression	$R_2=\frac{-FX}{FCU(I,N)}$	R52M	I52	N52	MSCC=1./(R52M*UF)-1.
Column 6 Value of I corresponds to RXXM Column 7 Value of N corresponds to RXXM							

It is essential to note that, when using difference equations, the expressions stated above indicate that only the structural elements containing or including point (m, n) need be considered. (The derivatives of the terms for all elements not containing (m, n) are zeros). This permits use of one set of general equations to represent any point in the structure.

Orthogonal Stiffener Grid

Figure 2-40 shows all structural elements which must be taken into account when a typical point (m, n) is considered.

The following limitations and assumptions apply:

1. All applied forces are in the plane of the structure.

2. Stiffeners carry axial load only.

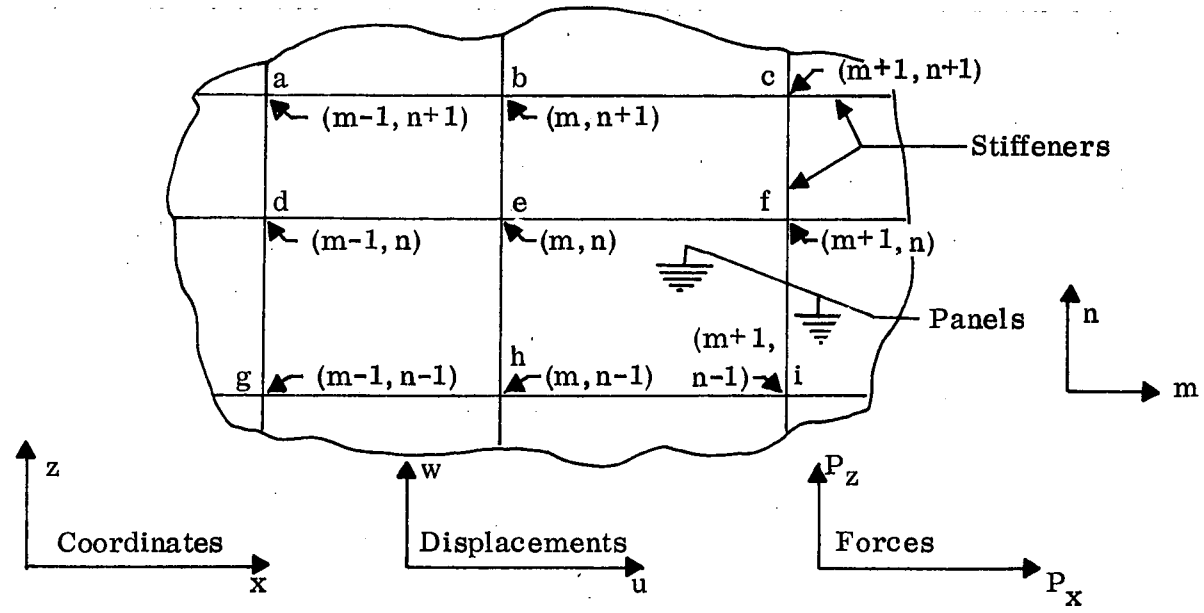

Figure 2-40. Structural Elements

3. The axial load carrying capacity of the panels must be predetermined and included as part of the axial load carrying capacity of the stiffeners; the panels carry only pure shear.

4. The stiffness of each axial or shear element is constant for the length of the element.

5. The axial load in a stiffener varies uniformly so that the shear in each attached panel is constant.

6. No stability failure can occur.

7. There is a constant linear load-deflection relationship for each structural element at all times.

8. Each stiffener is either parallel to or inclined at 90 degrees to each other stiffener.

For plane stresses in two direction

$$\epsilon_x = \frac{\partial u}{\partial x}; \qquad \epsilon_z = \frac{\partial w}{\partial z}; \quad \bar{\gamma}_{xz} = \frac{\partial u}{\partial z} + \frac{\partial w}{\partial x}$$

Expressed as first differences

$$\epsilon_x = \frac{\Delta u}{\Delta x}; \quad \epsilon_z = \frac{\Delta w}{\Delta z}; \quad \bar{\gamma}_{xz} = \frac{\Delta u}{\Delta z} + \frac{\Delta w}{\Delta x}$$

The strain energy expressions needed are

For a stiffener

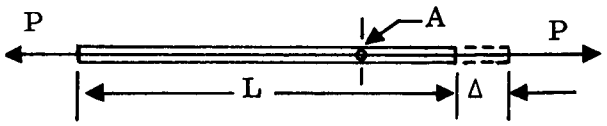

$$U = \frac{1}{2} P\Delta$$

$$\Delta = \frac{PL}{AE}, \quad \epsilon = \frac{\Delta}{L}$$

$$U = \frac{1}{2} \left(\frac{AE}{L}\right) \Delta^2 \tag{2-70}$$

For a shear panel

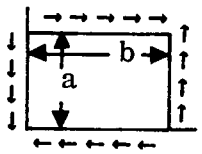

Deforms,

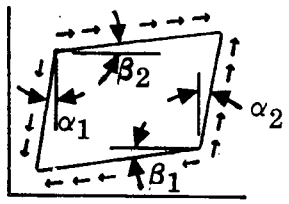

$$\bar{\alpha} = \frac{1}{2} (\alpha_1 + \alpha_2)$$

$$\bar{\beta} = \frac{1}{2} (\beta_1 + \beta_2)$$

$$\bar{\gamma} = \bar{\alpha} + \bar{\beta}$$

$$q = tf_s; \qquad f_s = G\bar{\gamma}$$

$$U = \frac{1}{2} (f_s ta)\, b\, \bar{\beta} + \frac{1}{2} (f_s tb)\, a\bar{\alpha}$$

$$U = \frac{1}{2} (f_s tab)\, (\bar{\alpha} + \bar{\beta}) = \frac{1}{2} Gt\, (\bar{\alpha} + \bar{\beta})^2\, (ab)$$

$$U = \frac{1}{2} Gtab\, \bar{\gamma}^2 \tag{2-71}$$

For a typical stiffener in the x-direction, for example, bar (m,n) to (m+1,n)

$$U_{m,n,x} = \frac{1}{2} \cdot \frac{(AE)_{m,n,x}}{x_{m+1,n} - x_{m,n}} \left(u_{m+1,n} - u_{m,n}\right)^2$$

Define

$$C_{m,n,x} \equiv \frac{AE\big|_{m,n,x}}{x_{m+1,n} - x_{m,n}}$$

and

$$U_{m,n,x} = \frac{1}{2} C_{m,n,x} (u_{m+1,n} - u_{m,n})^2 \tag{2-72}$$

For a typical stiffener in the z-direction, for example, bar (m,n) to (m, n+1).

$$U_{m,n,z} = \frac{1}{2} \cdot \frac{(AE)_{m,n,z}}{z_{m,n+1} - z_{m,n}} (w_{m,n+1} - w_{m,n})^2$$

Define

$$C_{m,n,z} = \frac{(AE)_{m,n,z}}{z_{m,n+1} - z_{m,n}}$$

and

$$U_{m,n,z} = \frac{1}{2} C_{m,n,z} (w_{m,n+1} - w_{m,n})^2 \tag{2-73}$$

For the shear panel (m, n)

$$U_{m,n,xz} = \frac{1}{2} \left[Gt|_{m,n} (x_{m+1,n} - x_{m,n})(z_{m,n+1}) \right] \bar{\gamma}^2$$

Define

$$\Delta x \equiv (x_{m+1,n} - x_{m,n}); \qquad \Delta z \equiv (z_{m,n+1} - z_{m,n})$$

$$\bar{\gamma}^2 = (\bar{\alpha} + \bar{\beta})^2 \qquad H_{m,n} \equiv \frac{1}{4} Gt|_{m,n}$$

Since

$$\bar{\alpha} = \left[\frac{(u_{m,n+1} = u_{m+1,n+1}) - (u_{m,n} + u_{m+1,n})}{2\Delta z} \right]$$

$$\bar{\beta} = \left[\frac{(w_{m+1,n+1} + w_{m+1,n}) - (w_{m,n+1} + w_{m,n})}{2\Delta x} \right]$$

$$U_{m,n,xz} = \frac{1}{2} H_{m,n} (\Delta x)(\Delta z) \left[\frac{(u_{m,n+1} + u_{m+1,n}) - (u_{m,n} + u_{m+1,n})}{\Delta z} \right.$$

$$\left. + \frac{(w_{m+1,n+1} + w_{m+1,n}) - (w_{m,n+1} + w_{m,n})}{\Delta x} \right]^2 \tag{2-74}$$

When constraints exist at (m, n) the strain energy in the constraints

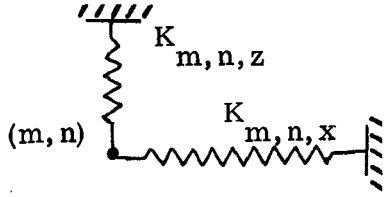

$$U_{m,n,z,k} = \frac{1}{2} K_{m,n,z} w_{m,n}^2$$

$$U_{m,n,x,k} = \frac{1}{2} K_{m,n,x} u_{m,n}^2$$

Then for any force applied at point (m, n), the total strain energy involved can be expressed as the sum of the energies of the elements surrounding the point, as stated previously in the development of the Energy Theorem.

$$U_{m,n} = U_{m,n,x} + U_{m-1,n,x} + U_{m,n,x,k} + U_{m,n,z} + U_{m,n-1,z} + U_{m,n,zk}$$

$$+ U_{m,n,xz} + U_{m+1,n,xz} + U_{m-1,n-1,xz} + U_{m,n-1,xz}$$

$$U_{m,n} = \frac{1}{2} C_{m,n,x} (u_{m+1,n} - u_{m,n})^2 + \frac{1}{2} C_{m-1,n,x} (u_{m,n} - u_{m-1,n})^2$$

$$+ \frac{1}{2} K_{m,n,x} u_{m,n}^2 + \frac{1}{2} C_{m,n,z} (w_{m,n+1} - w_{m,n})^2$$

$$+ \frac{1}{2} C_{m,n-1,z} (w_{m,n} - w_{m,n-1})^2 + \frac{1}{2} K_{m,n,z} w_{m,n}^2$$

$$+ \frac{1}{2} H_{m,n} \left[(\Delta x)(\Delta z)\right]_{m,n} \left[\frac{(u_{m,n+1} + u_{m+1,n+1}) - (u_{m,n} + u_{m+1,n})}{\Delta z_{m,n}} \right.$$

$$\left. + \frac{(w_{m+1,n+1} + w_{m+1,n}) - (w_{m,n+1} + w_{m,n})}{\Delta x_{m,n}} \right]^2$$

$$+ \frac{1}{2} H_{m-1,n} \left[(\Delta x)(\Delta z)\right]_{m-1,n} \left[\frac{(u_{m-1,n+1} + u_{m,n+1}) - (u_{m-1,n} + u_{m,n})}{\Delta z_{m-1,n}} \right.$$

$$\left. + \frac{(w_{m,n+1} + w_{m,n}) - (w_{m-1,n+1} + w_{m-1,n})}{\Delta x_{m-1,n}} \right]^2$$

$$+ \frac{1}{2} H_{m-1,n-1} \left[(\Delta x)(\Delta z)\right]_{m-1,n-1} \left[\frac{(u_{m-1,n} + u_{m,n}) - (u_{m+1,n-1} + u_{m,n-1})}{\Delta z_{m-1,n-1}} \right.$$

$$\left. + \frac{(w_{m,n} + w_{m,n-1}) - (w_{m-1,n} + w_{m-1,n-1})}{\Delta x_{m-1,n-1}} \right]^2 + \frac{1}{2} H_{m,n-1} \left[(\Delta x)(\Delta z)\right]_{m,n-1}$$

$$\times \left[\frac{(u_{m+1,n} + u_{m,n}) - (u_{m+1,n-1} + u_{m,n-1})}{\Delta z_{m,n-1}} + \frac{(w_{m+1,n} + w_{m+1,n-1}) - (w_{m,n} + w_{m,n-1})}{\Delta x_{m,n-1}} \right]^2 \quad (2\text{-}75)$$

All of the terms needed to satisfy these conditions are shown in Figure 2-40.

It follows from Equations 2-70 and 2-71

$$
\begin{aligned}
F_{m,n,x} = {} & -C_{m,n,x}(u_{m+1,n} - u_{m,n}) + C_{m-1,n,x}(u_{m,n} - u_{m-1,n}) + K_{m,n,x}u_{m,n} \\
& - H\frac{\Delta x}{\Delta z}\Big|_{m,n}\left[(u_{m,n+1} + u_{m+1,n+1}) - (u_{m,n} + u_{m+1,n})\right] \\
& - H_{m,n}\left[(w_{m+1,n+1} + w_{m+1,n}) - (w_{m,n+1} + w_{m,n})\right] \\
& - H\frac{\Delta x}{\Delta z}\Big|_{m-1,n}\left[(u_{m-1,n+1} + u_{m,n+1}) - (u_{m,n} + u_{m-1,n})\right] \\
& - H_{m-1,n}\left[(w_{m,n+1} + w_{m,n}) - (w_{m-1,n+1} + w_{m-1,n})\right] \\
& + H\frac{\Delta x}{\Delta z}\Big|_{m-1,n-1}\left[(u_{m-1,n} + u_{m,n}) - (u_{m-1,n-1} + u_{m,n-1})\right] \\
& + H_{m-1,n-1}\left[(w_{m,n} + w_{m,n-1}) - (w_{m-1,n} + w_{m-1,n-1})\right] \\
& + H\frac{\Delta x}{\Delta z}\Big|_{m,n-1}\left[(u_{m+1,n} + u_{m,n}) - (u_{m-1,n-1} + u_{m,n-1})\right] \\
& + H_{m,n-1}\left[(w_{m+1,n} + w_{m+1,n-1}) - (w_{m,n} + w_{m,n-1})\right] \qquad (2\text{-}76)
\end{aligned}
$$

$$F_{m,n,z} = -C_{m,n,z}(w_{m,n+1} - w_{m,n}) + C_{m,n-1,z}(w_{m,n} - w_{m,n-1}) + K_{m,n,z}\,w_{m,n}$$

$$- H_{m,n}\left[(u_{m,n+1} + u_{m+1,n+1}) - (u_{m,n} + u_{m+1,n})\right]$$

$$- H\frac{\Delta z}{\Delta x}\Big|_{m,n}\left[(w_{m+1,n+1} + w_{m+1,n}) - (w_{m,n+1} + w_{m,n})\right]$$

$$+ H_{m-1,n}\left[(u_{m-1,n+1} + u_{m,n+1}) - (u_{m,n} + u_{m-1,n})\right]$$

$$+ H\frac{\Delta z}{\Delta x}\Big|_{m-1,n}\left[(w_{m,n+1} + w_{m,n}) - (w_{m-1,n+1} + w_{m-1,n})\right]$$

$$+ H_{m-1,n-1}\left[u_{m-1,n} + u_{m,n}) - (u_{m-1,n-1} + u_{m,n-1})\right]$$

$$+ H\frac{\Delta z}{\Delta x}\Big|_{m-1,n-1}\left[(w_{m,n} + w_{m,n-1}) - (w_{m-1,n} + w_{m-1,n-1})\right]$$

$$- H_{m,n-1}\left[(u_{m+1,n} + u_{m,n}) - (u_{m+1,n-1} + u_{m,n-1})\right]$$

$$- H\frac{\Delta z}{\Delta x}\Big|_{m,n-1}\left[(w_{m+1,n} + w_{m+1,n-1}) - (w_{m,n} + w_{m,n-1})\right] \qquad (2\text{-}77)$$

Equations 2-76 and 2-77 are typical equations for any point in the structure. If the point under consideration is on an edge or borders a cut-out, the stiffness parameters, $C_{m,n}$ and $H_{m,n}$ become zero.

Thermal Effects

The effects of temperature differentials in a structure can be taken into account for an orthogonal grid by a modification of Equations 2-76 and 2-77. It should be noted that the thermal effects do not change the stiffness matrix, and hence are in effect external forces.

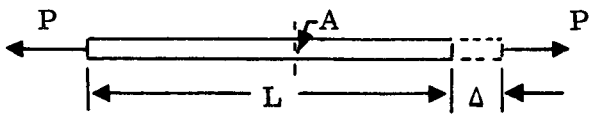

$$\Delta x = \Delta u - \theta k \Delta x$$

$$\Delta z = \Delta w - \theta k \Delta z$$

θ is the temperature differential of the bar ends, and k is the coefficient of thermal expansion.

$$U_{m,n,x,T} = \frac{1}{2} C_{m,n,x}\left[u_{m+1,n} - u_{m,n} - \theta k\,(x_{m+1,n} - x_{m,n})\right]^2$$

$$U_{m,n,z,T} = \frac{1}{2} C_{m,n,z} \left[w_{m,n+1} - w_{m,n} - \theta k \, (z_{m,n+1} - z_{m,n}) \right]^2$$

Again assuming that the panels carry only shear, their energy expressions do not change. They the total strain energy to describe the state at point (m, n) is

$$U_{m,n,T} = U_{m,n,x,T} + U_{m-1,n,x,T} + U_{m,n,z,T} + U_{m,n-1,z,T} + \Sigma U_{i,j,x,z,T} + \Sigma U_k$$

Define, $T_{m,n,x} \equiv k_{m,n,x} (x_{m+1,n} - x_{m,n}) \theta_{m,n,x}$

$$T_{m,n,z} \equiv k_{m,n,z} (z_{m,n+1} - z_{m,n}) \theta_{m,n,z}$$

$$U_{m,n,T} = \frac{1}{2} C_{m,n,x} (u_{m+1,n} - u_{m,n} - T_{m,n,x})^2 + \frac{1}{2} C_{m-1,n,x} (u_{m,n} - u_{m-1,n}$$

$$- T_{m-1,n,x})^2 + \frac{1}{2} C_{m,n,z} (w_{m,n+1} - w_{m,n} - T_{m,n,z})^2$$

$$+ \frac{1}{2} C_{m,n-1,z} (w_{m,n} - w_{m,n-1} - T_{m,n-1,z})^2 + \Sigma U_{i,j,x\,z} + \Sigma U_k$$

$$F_{m,n,x,T} = - C_{m,n,x} (u_{m+1,n} - u_{m,n,x} - T_{m,n,x}) + C_{m-1,n,x} (u_{m,n} - u_{m-1,n}$$

$$- T_{m-1,n,x}) + \Sigma \frac{\partial}{\partial u_{m,n}} (U_{i,j,xz}) + \Sigma \frac{\partial}{\partial u_{m,n}} (U_k)$$

$$F_{m,n,z,T} = - C_{m,n,z} (w_{m,n+1} - w_{m,n} - T_{m,n,z}) + C_{m,n-1,z} (w_{m,n} - w_{m,n-1}$$

$$- T_{m,n-1,z}) + \Sigma \frac{\partial}{\partial w_{m,n}} (U_{i,j,xz}) + \Sigma \frac{\partial}{\partial w_{m,n}} (U_k)$$

Then, from Equations 2-76 and 2-77

$$F_{m,n,x,T} = F_{m,n,x} + C_{m,n,x} T_{m,n,x} - C_{m-1,n,x} T_{m+1,n,x} \tag{2-78}$$

$$F_{m,n,z,T} = F_{m,n,z} + C_{m,n,z} T_{m,n,z} - C_{m,n-1,z} T_{m,n-1,z} \tag{2-79}$$

Formation of the Matrices

If the unknowns are listed in a specific order, the equations may be expressed in matrices of the form

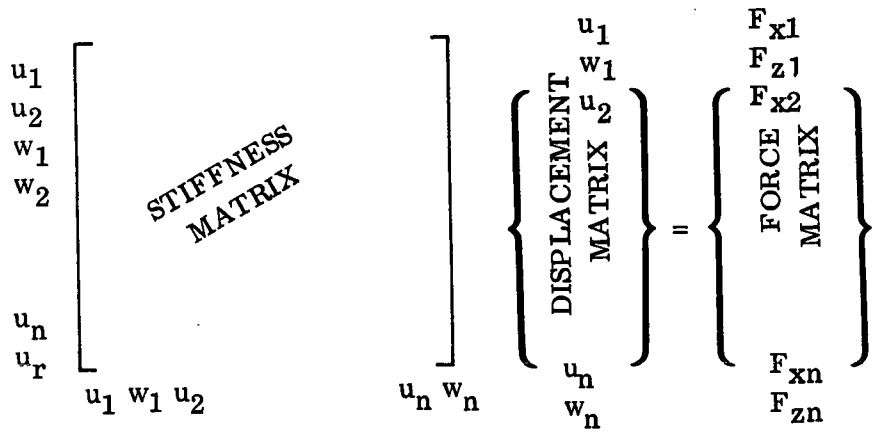

Since displacements are the unknown quantities, the problem is solved

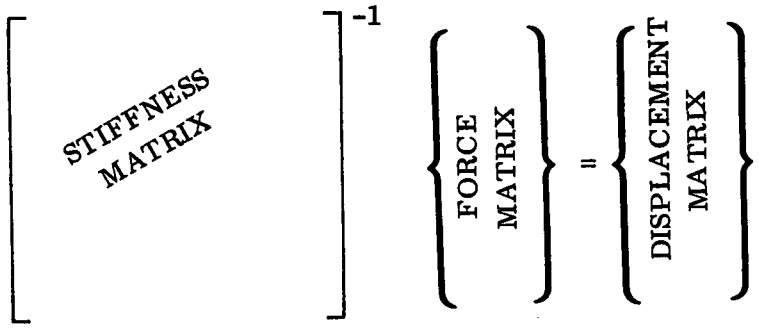

Examination of Equations 2-76 and 2-77 shows that for Point (m, n) a coefficient for u and w at each of the nine points considered is found in the expression for F_x and for F_z.

After the equations have been solved, the deflections of each point for which Strain-Energy equations were written are known. These displacements and the basic relationships are used to find internal stiffener loads and panel shear flows. These will be shown for the orthogonal grid.

For a stiffener

$$P = \frac{AE\Delta}{L}$$

Then in a stiffener (m, n), running in the x-direction

$$P_{m,n,x} = (u_{m+1,n} - u_{m,n}) \frac{AE}{L} \Big|_{m,n,x}$$

$$P_{m,n,x} = C_{m,n,x} (u_{m+1,n} - u_{m,n}) \qquad (2\text{-}78)$$

$$P_{m,n,z} = C_{m,n,z} (w_{m,n+1} - w_{m,n}) \qquad (2\text{-}79)$$

This is the internal load at the midpoint of stiffeners (m,n), and a positive sign indicates tension in the stiffener.

For a shear panel

$$q = tfs = tG\bar{\gamma} = tG\,(\bar{\alpha} + \bar{\beta})$$

$$q_{m,n} = 2H_{m,n}\left[\frac{(u_{m,n+1} + u_{m+1,n+1}) - (u_{m+1,n} + u_{m,n})}{\Delta z_{m,n}}\right]$$

$$+ 2H_{m,n}\left[\frac{(w_{m+1,n+1} + w_{m+1,n}) - (w_{m,n+1} + w_{m,n})}{\Delta x_{m,n}}\right] \qquad (2\text{-}80)$$

These are active shear flows, and the positive sign indicates shear flows in the positive direction act on sides with the more positive coordinates.

Equations 2-79 and 2-80 are valid.

For the thermal effects considered

$$P_{m,n,x,T} = C_{m,n,x}\,(u_{m+1,n} - u_{m,n} - T_{m,n,x}) \qquad (2\text{-}81)$$

$$P_{m,n,z,T} = C_{m,n,z}\,(w_{m,n+1} - w_{m,n} - T_{m,n,z}) \qquad (2\text{-}82)$$

A special purpose version of the previously described finite element computer program (Program No. P2354) has been prepared to perform the stress analysis of a TPS panel with bonded RSI. The major modifications to the program consist of (1) the addition of subroutines to generate the mathematical model, applied loads and temperatures internally from a minimum of input parameters, and (2) the addition of routines to compute maximum principal stresses and maximum shear stresses in the RSI and bond and to select the critical stresses in each element. Details of the necessary input data, mathematical model, stress calculations and an outline of the method of incorporating the RSI analysis in the existing stress program are discussed below. A comparison of preliminary results with a published analysis is also given.

The input parameters required to describe the panel geometry are as shown.

SL	= Semi Span (in)	TB	= Bond Layer Thickness (in)
TF1	= Inner Face Sheet Thickness (in)	TI	= Insulation (RSI) Thickness (in)
TF2	= Outer Face Sheet Thickness (in)	TC	= Protective Coating Thickness (in)
H	= Honeycomb Core Dept (in)		

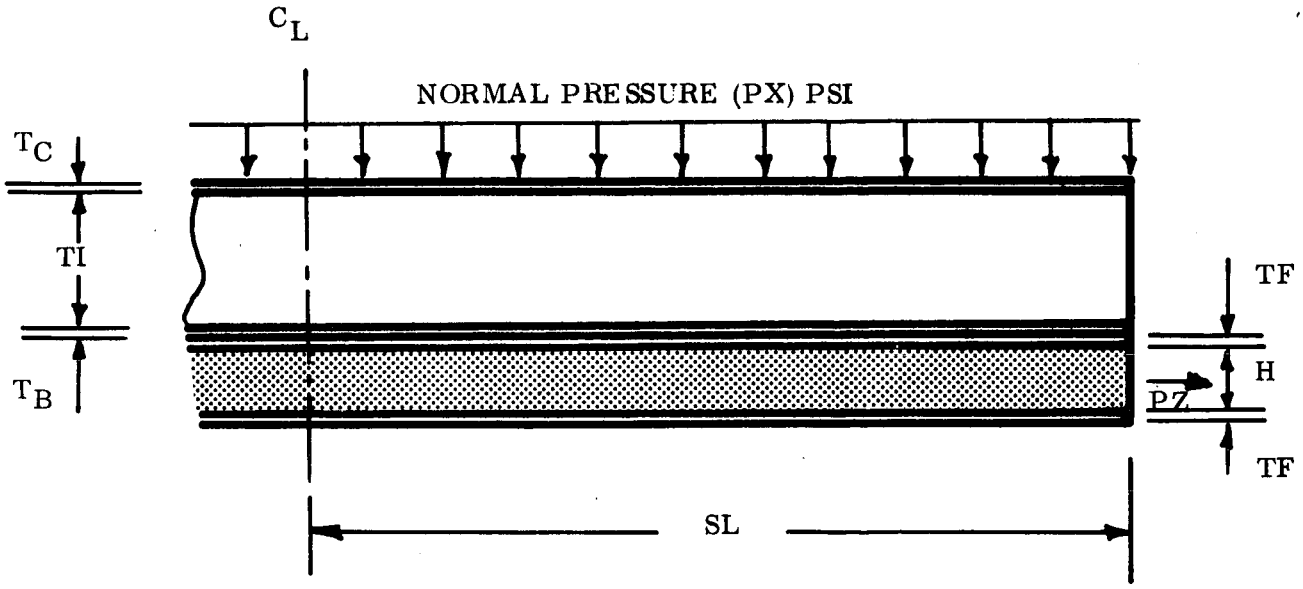

Figure 2-41. Panel Geometry

The input parameters defining the applied loads are

PX = Differential Pressure on Panel (psi)
PZ = Axial Load in Honeycomb Panel at Edge (lb)

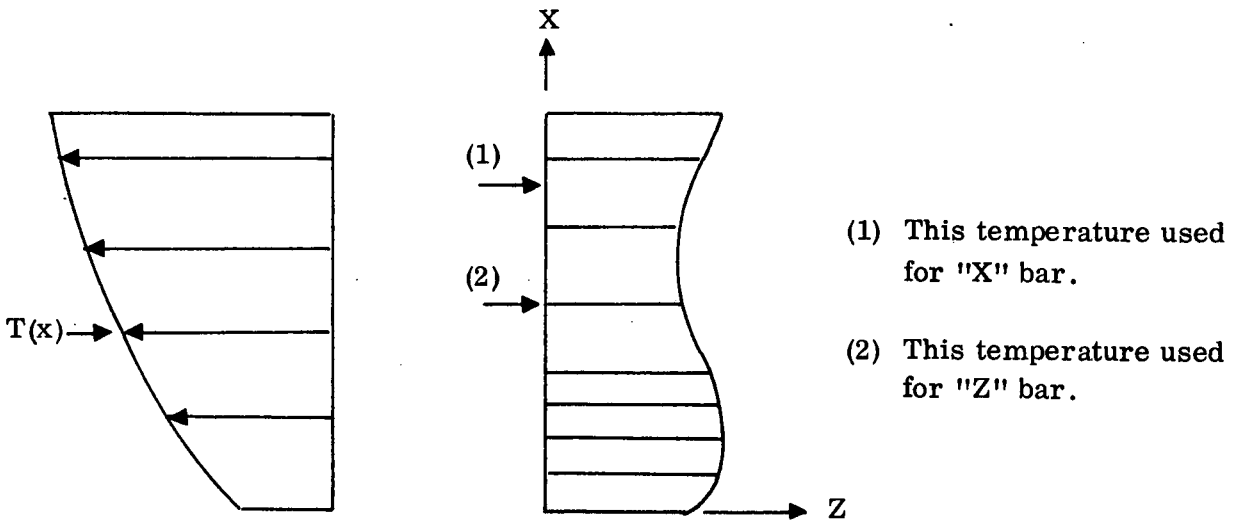

Figure 2-42. Transverse Temperature Distribution

The input parameters required to describe the transverse temperature distribution are

TX(I) = Temperature at Mid-Length of Each "X" Direction Bar Segment (° F)
TZ(I) = Temperature at Each "Z" Direction Bar (° F)

The temperature distribution is assumed constant in the "Z" direction.

The input parameters required to describe the temperature dependent material properties are

NT = Number of reference temperatures at which material properties are defined (the maximum number is 16)

E1(I) I = 1, NT Elastic Modulus of Face Sheets (psi)
E2(I) I = 1, NT Elastic Modulus of Core (psi)
E3(I) I = 1, NT Elastic Modulus of Bond (psi)
E4(I) I = 1, NT Elastic Modulus of RSI (psi)
E5(I) I = 1, NT Elastic Modulus of Coating (psi)

G2(I) I = 1, NT Shear Modulus of Core (psi)
G3(I) I = 1, NT Shear Modulus of Bond
G4(I) I = 1, NT Shear Modulus of RSI

ALFA1(I) I = 1,NT Temperature Coefficient of Face Sheets (in/in-°F)
ALFA2(I) I = 1,NT Temperature Coefficient of Core (in/in-°F)
ALFA3(I) I = 1,NT Temperature Coefficient of Bond (in/in-°F)
ALFA4(I) I = 1,NT Temperature Coefficient of RSI (in/in-°F)
ALFA5(I) I = 1,NT Temperature Coefficient of Coating (in/in-°F)
VB Poisson's Ratio of Bond

The mathematical model which represents one-half of the symmetrical panel is shown on Figure 2-43. Seven sets of longitudinal bars represent the panel face sheets, RSI and the protective coating. The number of sets of transverse bars (NH) is defined at input (Min. = 16 Max. = 40). The boundary conditions representing a simply supported panel are determined by eight constraints, one at each "Z" direction bar at the panel centerline which prevents axial displacement while permitting free displacement in the "X" direction. Displacement in the "X" direction is constrained at the panel edge. The derivation of the grid spacing, bar areas, bar and panel properties and the applied loads from the input parameters follows.

Distance between sets of "Z" direction bars DX(J)

DX(1) = H + .5 (TF1 + TF2)
DX(2) = TB
DX(3) = DX(4) = DX(5) = 2.* (TI + 0.5 * TC)/7
DX(6) = 0.5 * DX(3)

Distance between sets of "X" direction bars (DZ(I))
The basic grid size is progressively reduced as the panel edge is approached.

N1 = NH - 15
N2 = N1 + 4
N3 = N2 + 6

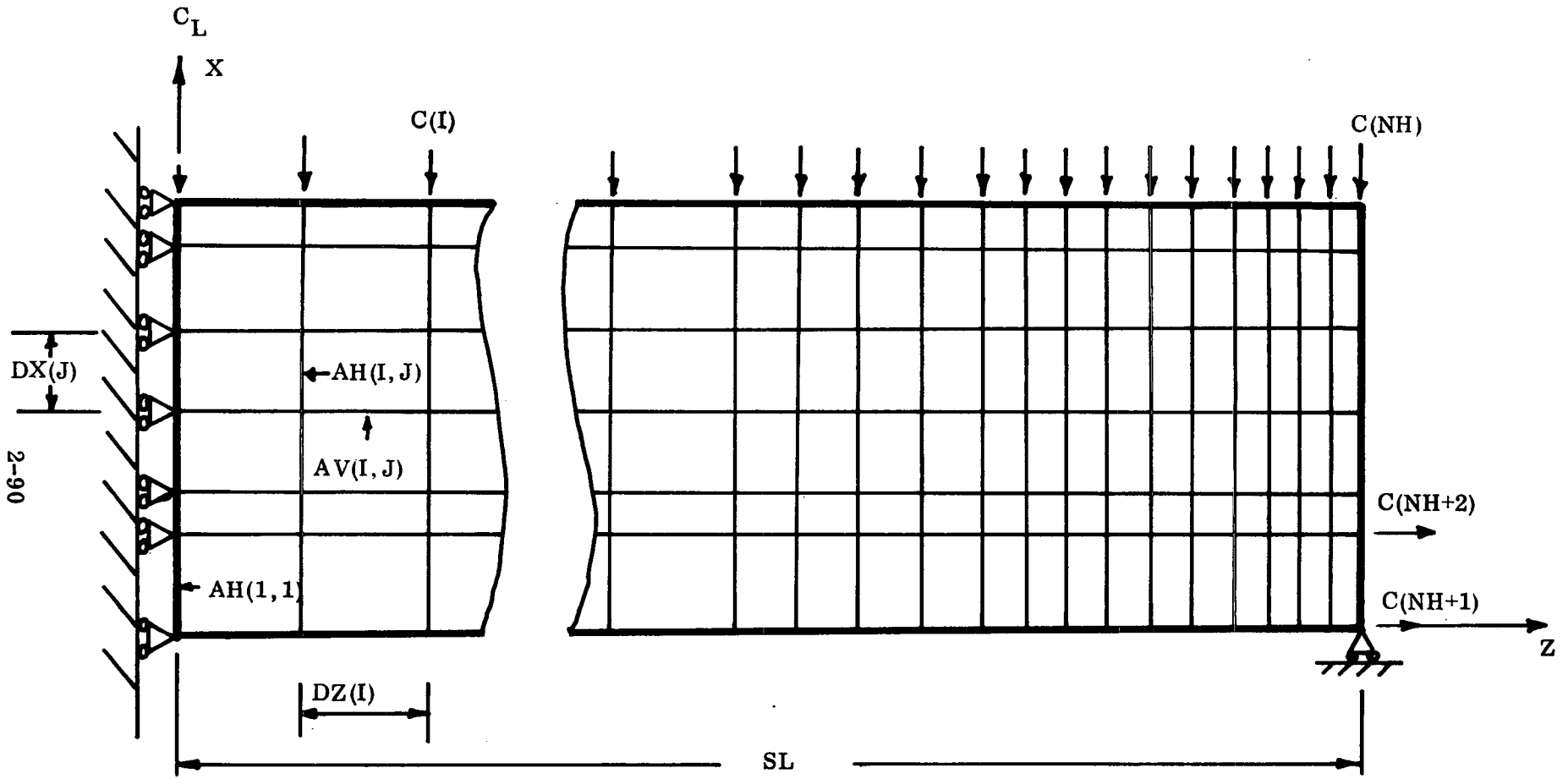

Figure 2-43. Mathematical Model

```
DZ(I) = SL/FLOAT (N1 + 4)
IF (I.GT.N1) DZ(I) = DZ(1)/2
IF (I.GT.N2) DZ(I) = DZ(1)/3
IF (I.GT.N3) DZ(I) = DZ(1)/4
```

Areas of "X" direction bars AH(I,J)

```
NH1 = NH-1
AH(1,J) = DZ(1)/2.
AH(I,J) = .5 * (DZ(I-1) + DZ(2))          I = 2, NH1 J = 1,7
AH(NH,J) - DZ(NH1)/2.
```

Areas of "Z" direction bars AV(I,J) I = 1, NH1

```
AV(I,1) = TF1
AV(I,2) = TF2
AV(I,3) = DX(6)
AV(I,4) = AV(I,5) = AV(I,6) = DX(3)
AV(I,7) = TC
```

The temperature dependent material properties required in the station are

```
EH(I,J) = Elastic Moduli of "X" direction bars
CH(I,J) = Temperature coefficient of "X" direction bars
EV(I,J) = Elastic moduli of "Z" direction bars
CV(I,J) = Temperature coefficient of "Z" direction bars
G(I,J)  = Moduli of rigidity of shear panels
```

Given the temperature distributions TX(I) and TZ(I), the instantaneous values of parameters are computed by linear interpolation from the input material properties at the reference temperature (T1(I)).

For the "X" direction bars representing the bond layer (EH(I,2)), a correction factor is applied to account for the fact that under normal loading lateral deformation of the relatively soft bond is restrained by the adjacent faces.

Assuming the lateral deformations are zero the correction factor is given by

$$\text{Factor} = \frac{(1 - VB)}{(1 + VB)\ (1 - 2VB)}$$

where VB = Poisson's ratio for the bond.

Stress Calculations

The output from program P2354 consists of the following stresses

FH(I, J) = Axial stresses in "X" direction bars
FV(I, J) = Axial stresses in "Z" direction bars
FS(I, J) = Shear stresses in panels

For the RSI, maximum principal stresses and maximum shear stresses (Figure 2-44) are derived as follows

$$FP(I,J) = (FV(I,J) + FH(I,J-1)/2. \pm \left[\left(\frac{FV(I,J) - FH(I,J-1)}{2} \right)^2 + FS(I,J-1)^2 \right]^{1/2}$$

$$FSM(I,J) = \left[\left(\frac{FV(I,J) - FH(I,J-1)}{2} \right)^2 + FS(I,J-1)^2 \right]^{1/2}$$

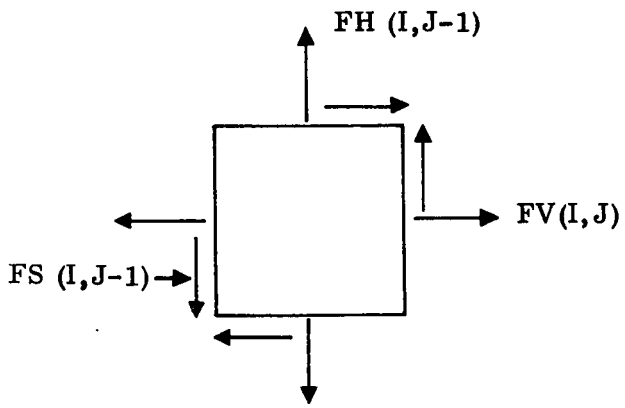

Figure 2-44. Elemental Volume

Due to the repetitive use of the stress analysis in the overall TPS optimization program it is considered that the sole use of the finite element program (P2354) would result in prohibitive computing time; hence, a basic analysis will be performed using the existing thermal stress and overall bending analysis routines adapted to the RSI panel. Upon completion of the trajectory and when the most critical trajectory points (minimum margin of safety) are determined, the stress analysis at the most critical points will be repeated using Program P2354 and the resulting stresses used to compute the final margins. A flow chart is given in Figure 2-45.

The failure modes considered, the corresponding margins of safety and the buckling equations used for the sandwich face sheets are given below.

Element	Modes Considered
Face Sheets	Yielding, ultimate tension, wrinkling, dimpling
Core	Ultimate shear
Bond	Ultimate shear and normal stress (peeling)
Insulation	Ultimate tension, compression, shear
Coating	Ultimate tension, compression

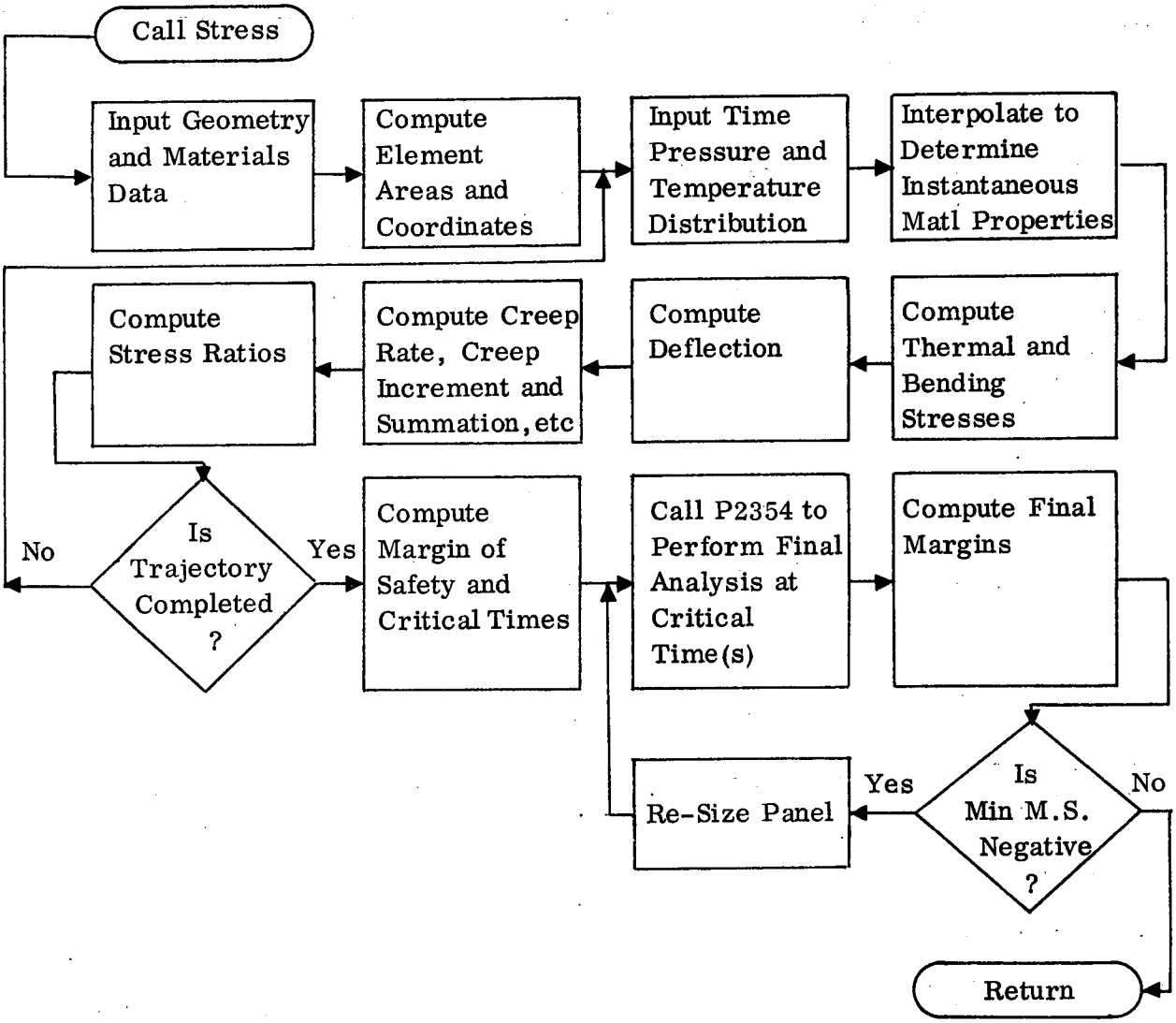

Figure 2-45. Flow Chart of RSI Analysis

Margins of Safety

Face Sheets

Yielding $MS = (FTY/F_{NET}) - 1$ Tension

$MS = (FCY/F_{NET}) - 1$ Compression

Ultimate Tension $MS = \dfrac{FTU}{F_{NET\ (UF)}} - 1$

Ultimate Compression $MS = \dfrac{FCR}{F_{NET\ (UF)}} - 1$

where FCR is given by the smaller of the critical wrinkling or dimpling buckling stresses.

Honeycomb Core

Shear $$MS = \frac{FSU}{FS\ (UF)} - 1$$

Normal Stress (Peeling) $$MS = \frac{F_{tu}}{F_n\ (UF)} - 1$$

Insulation (RSI)

Ultimate Tension or Compression $$MS = \frac{F_{tu}}{F_t\ (UF)} - 1 \qquad MS = \frac{F_{cu}}{F_c\ (UF)} - 1$$

Shear $$MS = \frac{F_{su}}{F_s\ (UF)} - 1$$

Coating

Ultimate Tension or Compression $$MS = \frac{F_{tu}}{F_t\ (UF)} - 1 \qquad MS = \frac{F_{cu}}{F_c\ (UF)} - 1$$

Honeycomb sandwich panel

Local buckling of face sheets

The sandwich panel face sheets are analyzed for two modes of local buckling under compression loads as follows:

a. Wrinkling. In this mode the face sheets buckle in a series of sinusoidal waves. The critical buckling stress is given by

$$\sigma_{wr} = 0.5\ (G_c\ E_{cz}\ \eta\ E_f)^{1/3}$$

where

G_c = modulus of rigidity of the core

E_{cz} = modulus of elasticity of the core

E_f = modulus of elasticity of face sheet

η plasticity factor = E_T/E

b. Intercell Buckling. In this mode the face sheet distorts in a pattern of dimples the size of the honeycomb cells.

The critical buckling stress is given by

$$\sigma_{cr} = 3.\eta E_f (t_f/d)^2$$

where

d = honeycomb cell diameter

t_f = thickness of face sheet

E_f and η as given for wrinkling

To evaluate the finite element model of Program P2354, a comparison was made with a published analysis of Lockheed, (Reference 10).

Verification of Finite Element Stress Analysis

Preliminary runs using Program P2354 have been made simulating the model used on page 3-3 of the reference as shown below

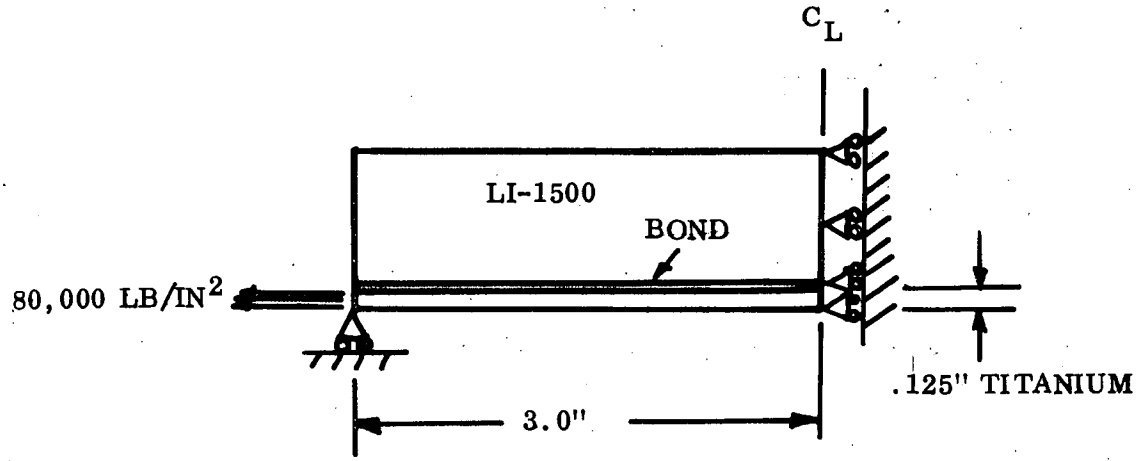

Simulation Model

The structural panel used in the model is represented by a solid 0.125 inch plate. Therefore, this plate must be idealized as a sandwich panel for Program P2354.

For combined bending and axial loading, the bending and axial stiffnesses must be represented correctly. In addition, the distance from the bond line to the panel centroid must be preserved in the idealized model.

The requirements are:

(1) $A_1 + A_2 = A_P$

(2) $A_2 (\bar{Y})^2 + A_1 (H-\bar{Y})^2 = I_P$

(3) $\frac{A_1 H}{A_1+A_2} = \frac{A_1 H}{A_P} = \bar{Y}$

This yields

$$H_2 = \frac{I_P}{A_P \bar{Y}} + \bar{Y}$$

$$A_1 = \frac{\bar{Y} \cdot A_P}{H_C}$$

$$A_2 = A_P (1 - \bar{Y}/H)$$

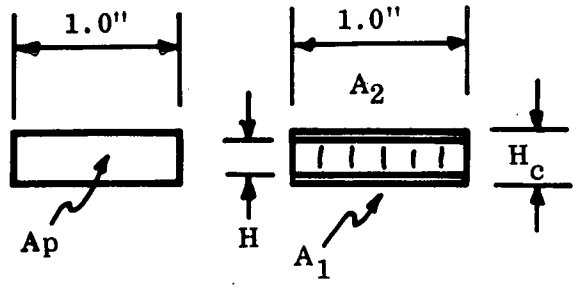

For 0.125 Plate

$$A_P = 0.125 \text{ in}^2 \qquad \bar{Y} = 0.0625 \text{ in}$$

$$H_C = \frac{(0.125^3/12)}{0.125 \times 0.0625} + 0.0625 = 0.08333 \text{ in}$$

$$A_1 = \frac{0.0625 \times 0.125}{0.08333} = 0.09375 \text{ in}$$

$$A_2 = 0.125 (1 - 0.0625/0.08333) = 0.03125 \text{ in}$$

The shear stiffness of the idealized honeycomb panel is represented by using an equivalent modulus of rigidity for the core.

$$G_e = \frac{G_P A_P}{H_c} = \frac{0.125}{0.0833} G_P$$

The overall agreement is good except for the bond normal stress (approximately 60% of Reference 10 values). This is considered due to the fact that the P2354 analysis did not consider lateral restraint of the soft bond layer (E = 300 psi) by adjacent faces.

Assuming lateral deformations are restrained, the effective modulus of elasticity is given by (Reference 37)

$$E_{ff} = \frac{E (1 - \gamma)}{(1 + \gamma) (1 - 2\gamma)}$$

Table 2-25. Comparison of Maximum Bond and RSI Stresses (Neglecting Correction to Bond Elastic Modulus Due to Lateral Restraints)

Case No.	Bond Thickness	Bond Stresses		RSI Stresses	
		Max. Shear	Max. Normal	Max. Shear(1)	Max. Principal
A1	0.032	40.1 (41)	26.4 (49)	40.1 (38.0)	122 (111)
A2	0.020	51.3 (51)	27.1 (60)	51.3 (42.0)	139 (125)
A4	0.015	59.0 (59)	45.1 (70)	59.0 (56.0)	147 (138)

Values in parentheses are from Reference 37.

(1) The maximum shear in the RSI occurs at the bond line and is equal to the bond shear stress.

Table 2-26. Comparison of Maximum Bond and RSI Stresses (With $E_{bond} = E_{eff}$ and $\gamma = 0.45$)

Case No.	Bond Thickness	Bond Stresses		RSI Stresses	
		Max. Shear	Max. Normal	Max. Shear(1)	Max. Principal
A1	0.032	41.2 (41)	41.6 (49)	41.2 (38)	124 (111)
A2	0.020	52.8 (51)	57.7 (60)	52.8 (42)	140 (125)
A4	0.015	60.8 (59)	69.2 (70)	60.8 (56)	148 (138)

With this correction a value of Poisson's ratio approximately equal to 0.45 must be assumed in order to match the panel bond stresses given by Reference 37. The effect on the other peak stresses is negligible.

where

E = bond modulus of elasticity

γ = Poisson's ratio

2.2.1.2 Carbon-Carbon Composites. The carbon-carbon leading edge was investigated for adaptation to the TPS sizing routine. Carbon and graphite composites are important because they possess excellent high temperature stability and retain structural integrity at temperatures above 4,000F. This latter property alone makes the carbon-graphite class of unique candidated TPS materials. To fully utilize the high temperature properties of carbon and graphite composites for reusable entry thermal protection systems, an impervious oxidation barrier must be provided for the material. Efforts have been made in the past few years to increase the oxidation resistance of carbon and graphite composites by the use of select fillers and coatings. These effects have been successful in providing improvements in oxidation protection. To provide the capability for multiple, long-time exposures to expected shuttle entry environments, advanced oxidation protection techniques are currently being developed.

Because of the problems encountered with laminated carbon-carbon composite material (limitations in design flexibility associated with the complex tooling, local reinforcements for attachments, and overall reliability) a 3-D reinforced carbon-carbon fluted core concept has been developed (Figure 2-46) as a lightweight, double faced, truss core structure that integrates an external heat shield cover panel with a support structure. The support can in turn be attached to a primary load carrying structure. The concept consists of a 3-D woven truss core fabric that is rigidized with high-carbon-yield resins, pyrolyzed, and then carbonized up to 4,000F in an inert atmosphere. A simulated shuttle vehicle leading edge demonstration article has been fabricated to demonstrate the feasibility of forming the truss core. The development of the oxidation inhibited carbon-carbon 3-D fluted core has been accomplished in a joint effort between the Convair Aerospace Division of General Dynamics and the Defense Products Division of HITCO.

The truss core configuration shown in Figure 2-46 was selected as the baseline concept for the TPS optimization studies for two reasons: the truss configuration is structurally very efficient, and experience in fabrication has shown it is easier to process than other concepts. The thicknesses and other dimensional variables are independent, allowing for considerable flexibility in design. However, it is emphasized here that almost any carbon-carbon configuration can be analyzed by the TPS sizing routine by using the appropriate equivalent properties; the analysis is not restricted to truss core.

Thermal Analysis

To treat the heat transfer as a two-dimensional problem, the panel is considered as three layers; an outer and an inner layer of carbon-carbon material with an "equivalent" material between them. The middle layer has the same mass as the truss core which it represents. This defines a density and specific heat of the equivalent material. The resistance to heat flow is given by an "apparent" thermal conductivity. The truss core apparent conductivity and other properties will be modified by geometry changes, and by the use of filler materials (for radiation barriers) in the gaps.

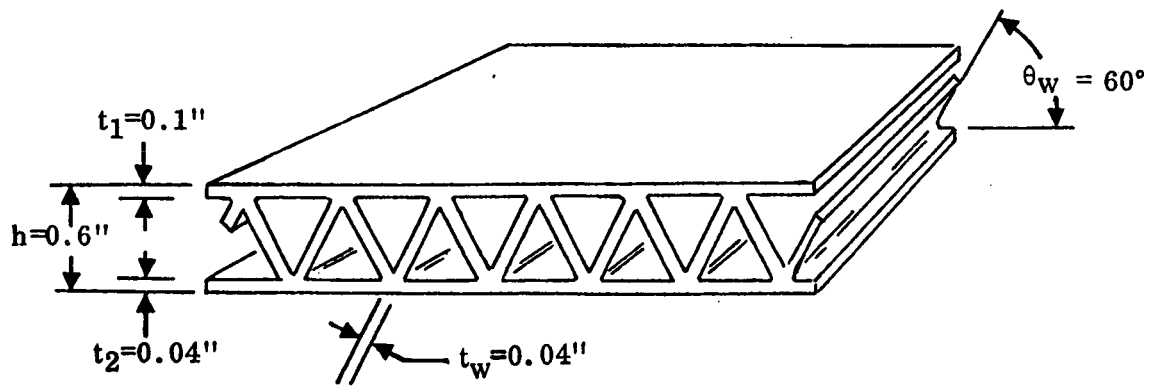

Figure 2-46. Baseline Carbon-Carbon Truss Core Configuration

The basic problems to be treated by the thermal analysis and insulation sizing are:

1. Compute temperatures of the panel, underlying insulation and internal structure: check that panel temperature is below the temperature constraint.

2. Increase thickness of insulation between panel and internal structure (if necessary) to reduce structural temperature to below the maximum allowable value.

The geometric representation of the outer surface airfoil contour is given in Figure 2-47, and the nodal representation of the panel for the conduction matrix is given in Figure 2-48.

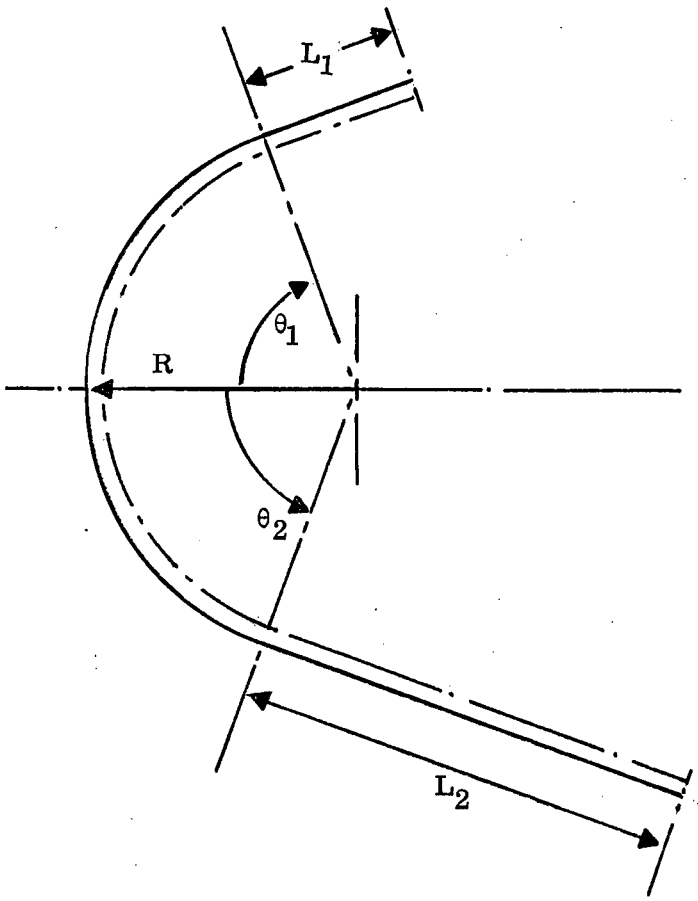

Figure 2-47. Leading Edge Outer Surface Contour Geometry

A thermal analysis has been made for an example configuration with geometry as given in Figure 2-49. This corresponds to the leading edge of an NACA 0012-64 airfoil which is taken as a typical wing section for a Space Shuttle orbiter.

Trajectory data were taken for a typical 30° angle of attack entry. The leading edge stagnation line heating was computed for a laminar swept cylinder using the method of Kemp and Riddell, and is shown for this trajectory in Figure 2-50. The off-stagnation-line heating was obtained from the distribution of Lees shown in Figure 2-51.

Figure 2-52 shows the temperature versus time of three outer panel nodes and the temperature response of the structural node achieving the highest temperature. These results illustrate the temperature gradients in the directions along and normal to the panel surface through to the internal structure. It is of interest to note that the results obtained from the TPS sizing routine and shown in Figure 2-52 using a calculation time interval of 0.5 second compared very closely with computations carried out using the General Dynamics Variable Boundary II Program (an implicit method of solution). The explicit solution of the sizing routine used about half of the computer time of the other program. In addition, close agreement was obtained with repeat runs using time steps up to 1.25

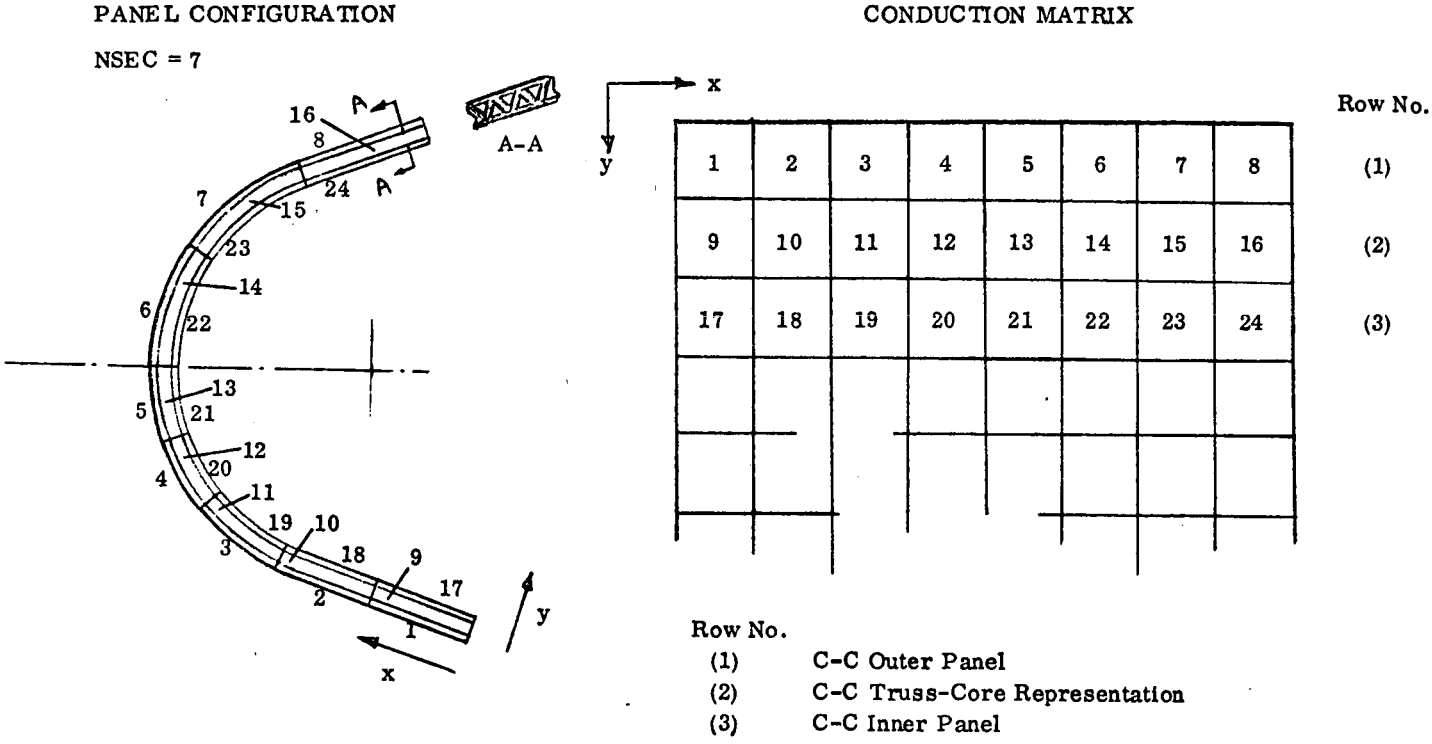

Figure 2-48. Carbon-Carbon Leading Edge Conduction Matrix

Carbon-Carbon Leading Edge Example

A. Outer Surface Contour Geometry

$R = 5.30$ in
$L_1 = 3.06$ in
$L_2 = 6.31$ in
$\theta_1 = 60°$
$\theta_2 = 60°$

B. Conduction Matrix

Dimension in Inches

Column No.	1	2	3	4	5	6	7	8
ΔX	3.25	3.06	1.85	1.85	1.85	2.77	2.77	3.06
ΔY_1 (C-C Outer Panel)	.10	.10	.10	.10	.10	.10	.10	.10
ΔY_2 (C-C Truss-Core)	.46	.46	.46	.46	.46	.46	.46	.46
ΔY_3 (C-C Inner Panel)	.04	.04	.04	.04	.04	.04	.04	.04
ΔY_4 (Dynaflex Insulation)	1.00	1.00	1.00	1.00	1.00	1.00	1.00	1.00
ΔY_5 (T_i Structure)	.25	.25	.25	.25	.25	.25	.25	.25

Figure 2-49. Dimensions for Carbon-Carbon Leading Edges Example

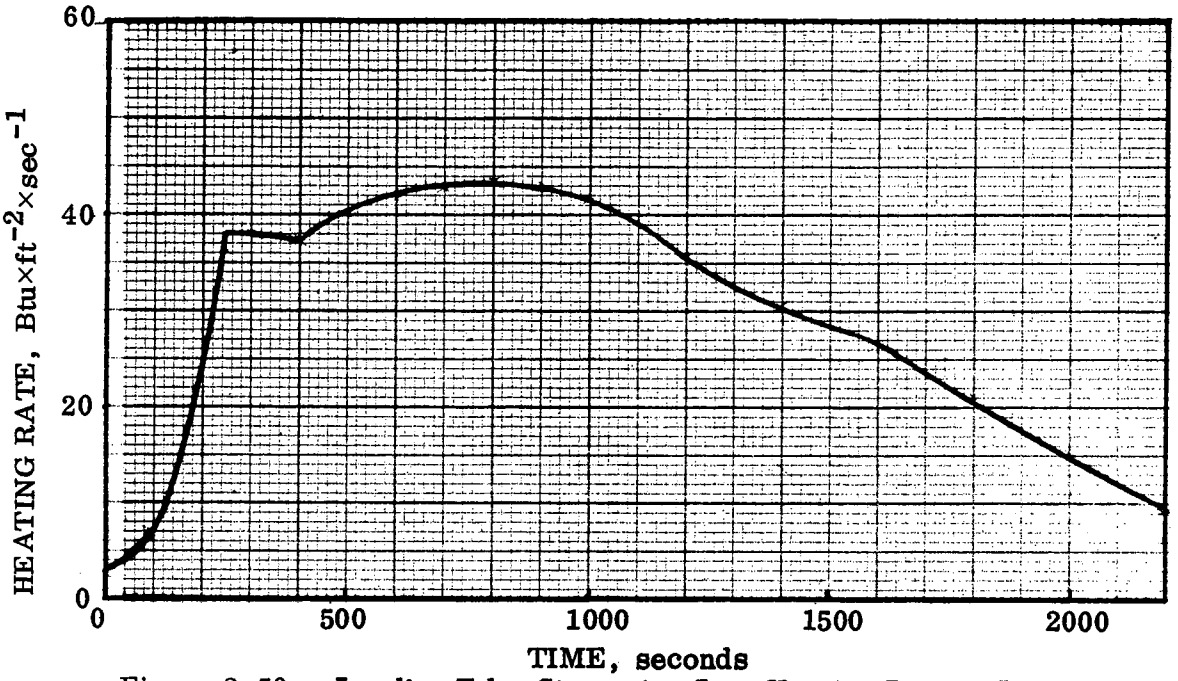

Figure 2-50. **Leading Edge Stagnation Line Heating During Entry**

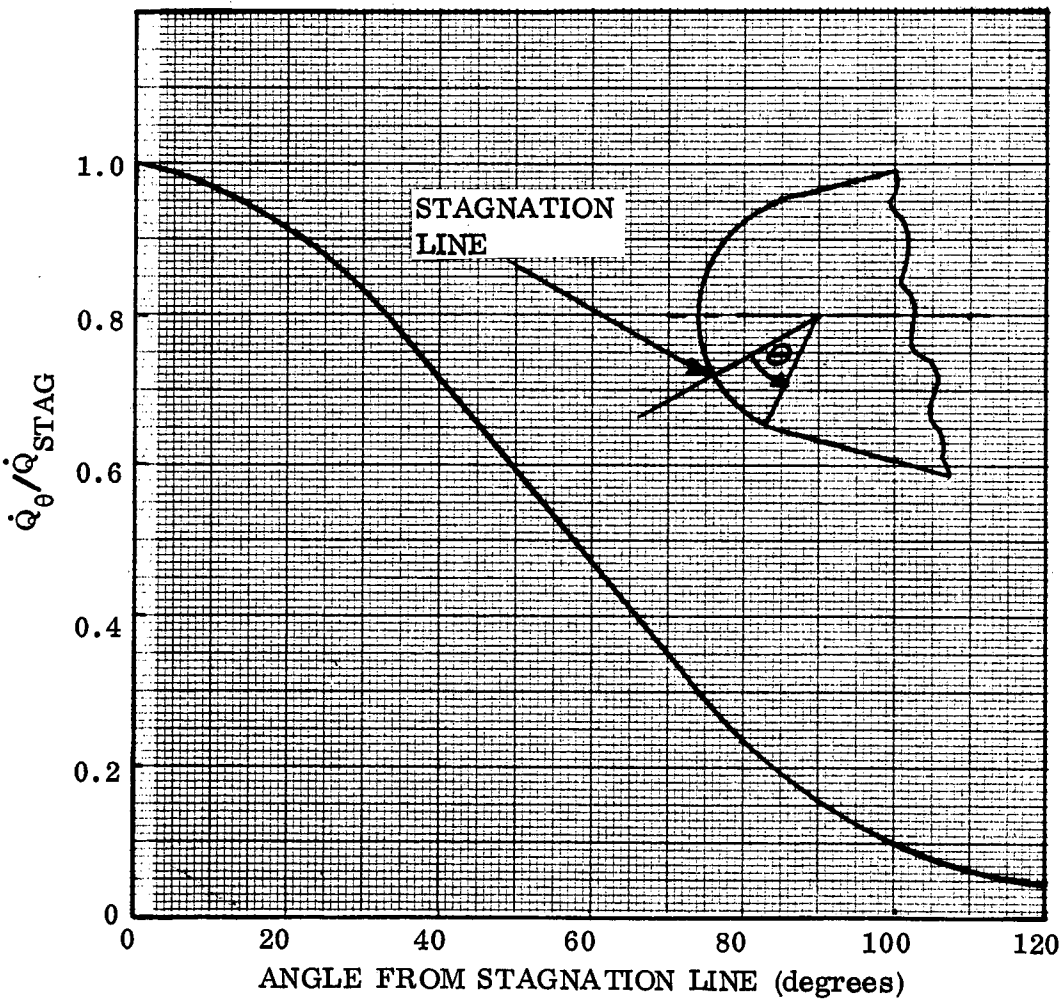

Figure 2-51. Off-Stagnation Line Heating

1 INCH THICK 10 PCF DYNAFLEX INSULATION

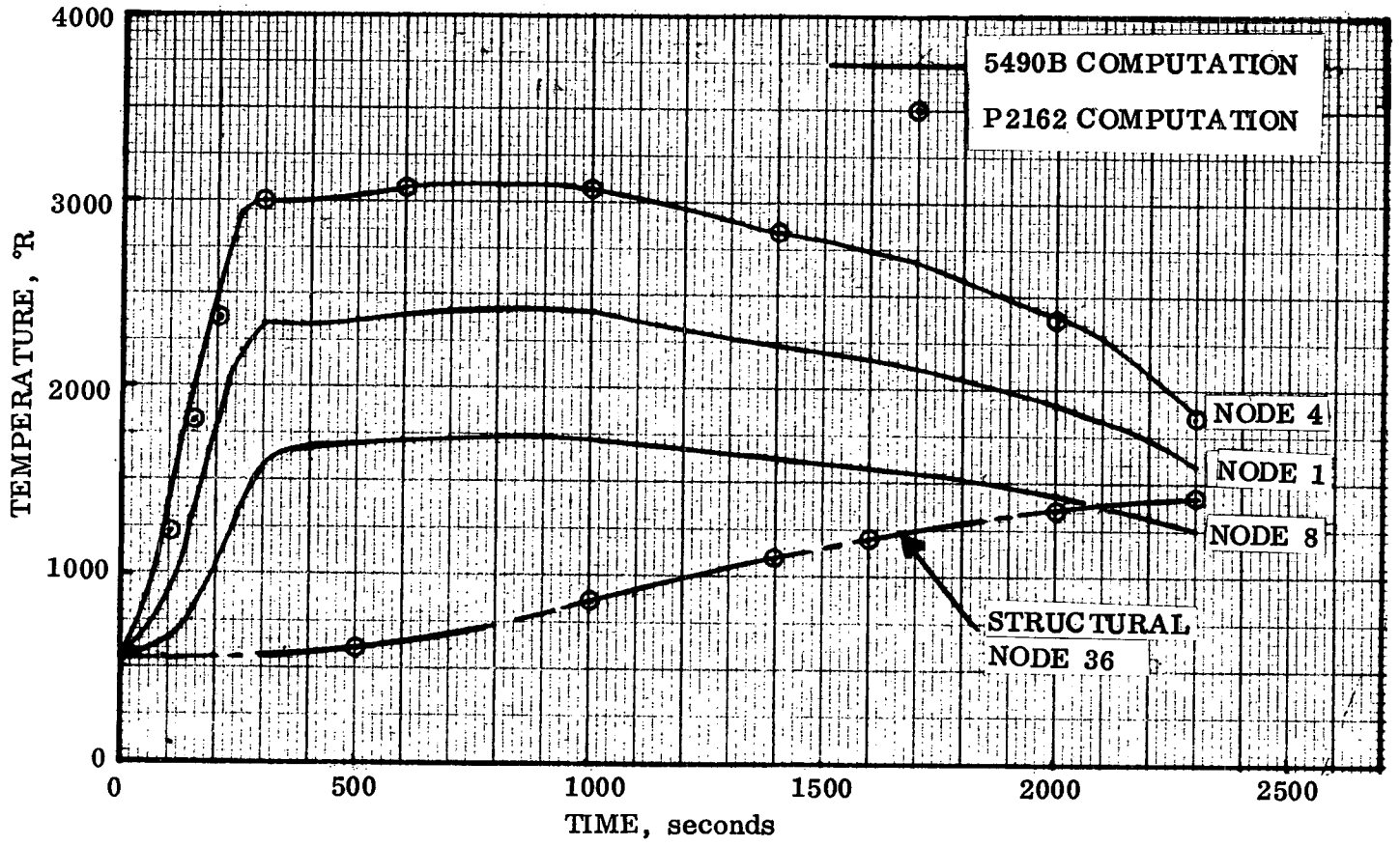

Figure 2-52. Reentry Temperature Response of Leading Edge

seconds; for an input calculation interval of 2.5 seconds, the solution diverged and the program automatically adjusted to 1.25 seconds.

The temperature response of the interior material normal to the stagnation line node (nodes 4, 12, 20, 28, 36) at various times during reentry is given in Figure 2-53. Figure 2-54 shows the effect on structure temperature of increasing the insulation thickness from 1 inch to 2 inches.

Stress Analysis

A stress model was also developed but never implemented to the computer program due to increased emphasis directed toward the charring ablator and RSI. It is included here for the sake of completeness.

A section of 60° truss core carbon-carbon leading edge at a given span location is sized for combined airloads and thermal loads. A single value of facesheet thickness and a single value of core truss thickness are calculated for a constant sandwich depth.

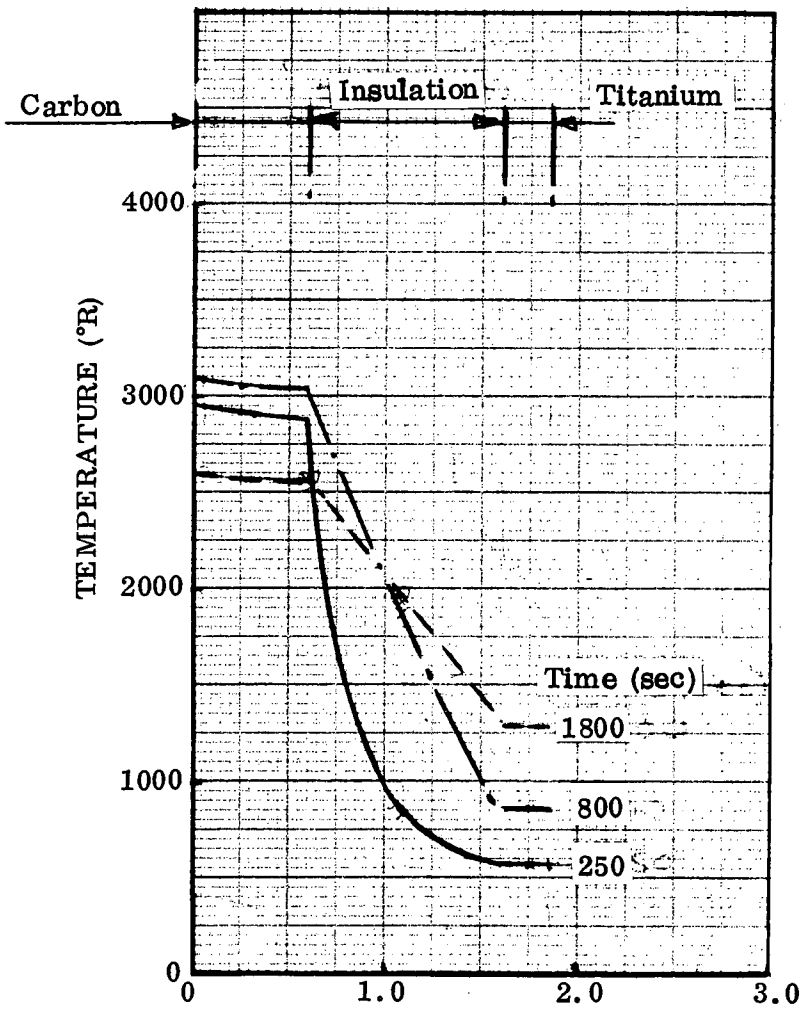

Figure 2-53. Temperature Response Normal to Surface Node 4

The shape of a chordwise section of leading edge is idealized to a constant radius section and two straight sections (Figure 2-55). Figure 2-56 illustrates the procedure. The model is then divided into a fixed number of elements: 5 elements for the curved section and 3 elements for each of the straight sections. Element length, centroid location, and angular orientation are calculated based on the input basic geometry. Upper and lower edges are assumed to be fully fixed, and the overall sandwich depth remains constant as input. Section properties for a unit spanwise width of leading edge are calculated based on an input estimate of facesheet thickness.

Airload pressures acting on each of the elements are calculated as part of the aerothermal environment for each load condition. The resulting normal loads are computed and resolved into horizontal and vertical components.

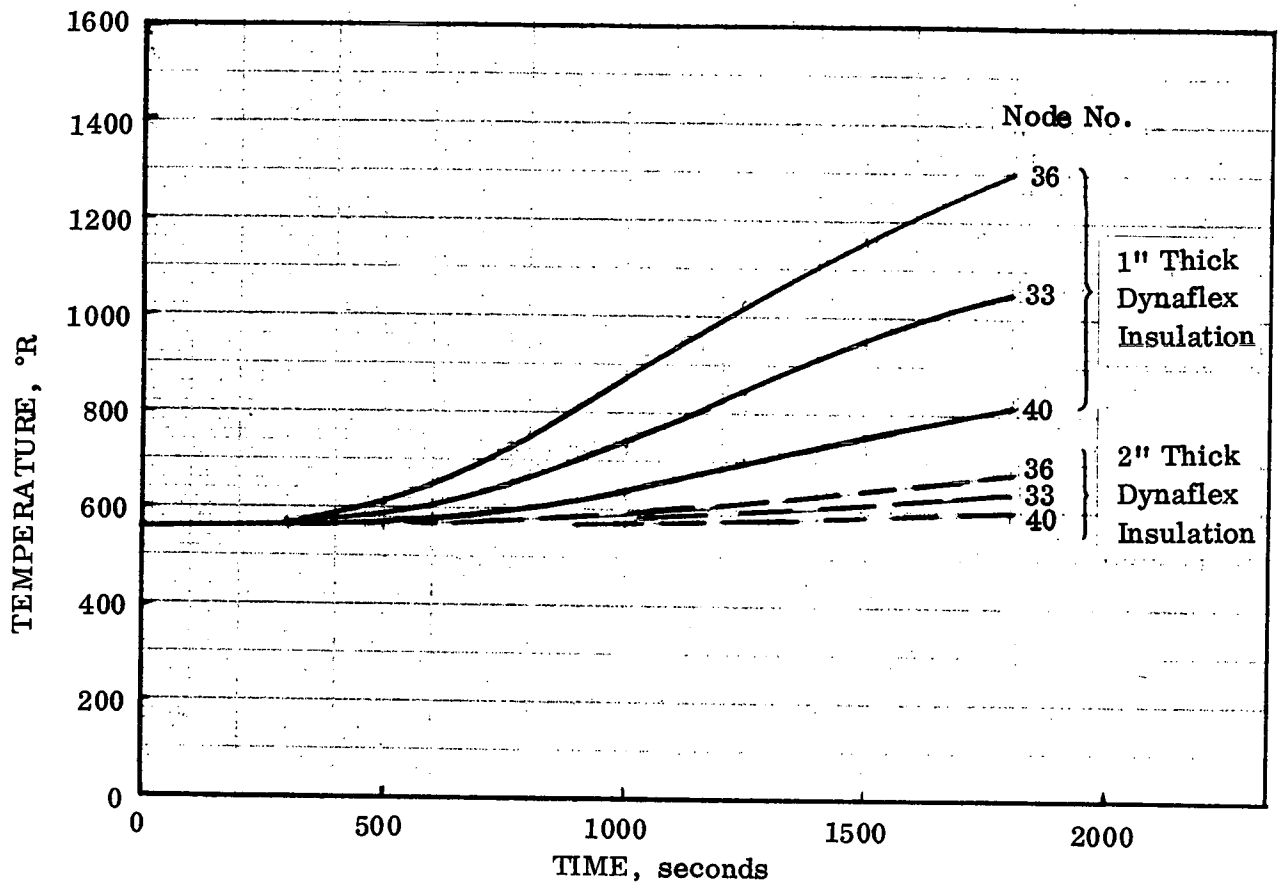

Figure 2-54. Structural Temperature Response

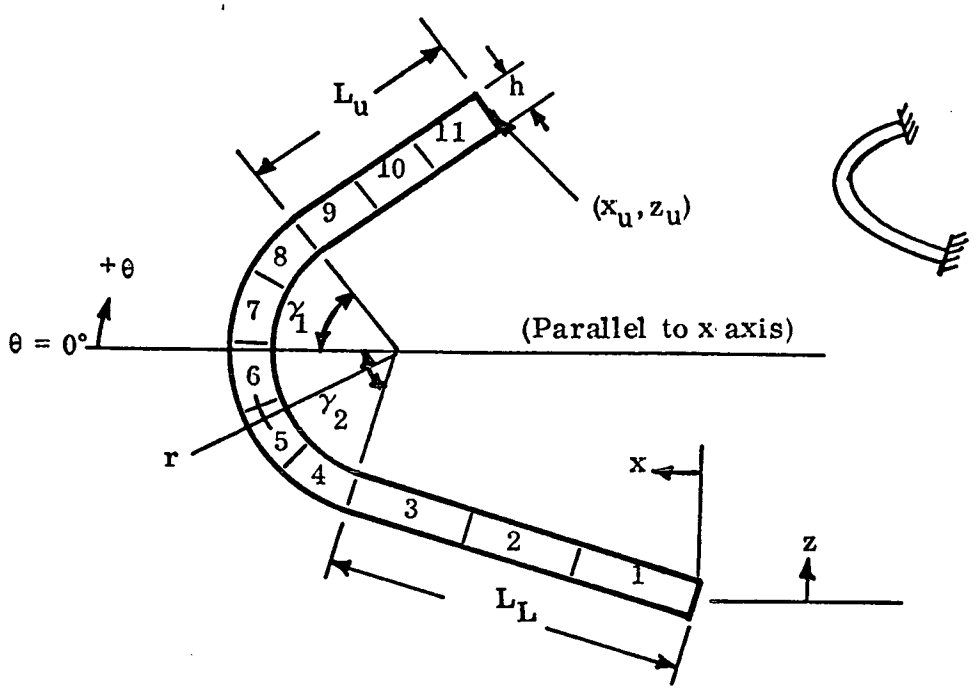

Figure 2-55. Schematic of Carbon-Carbon Stress Analysis Nodal Geometry

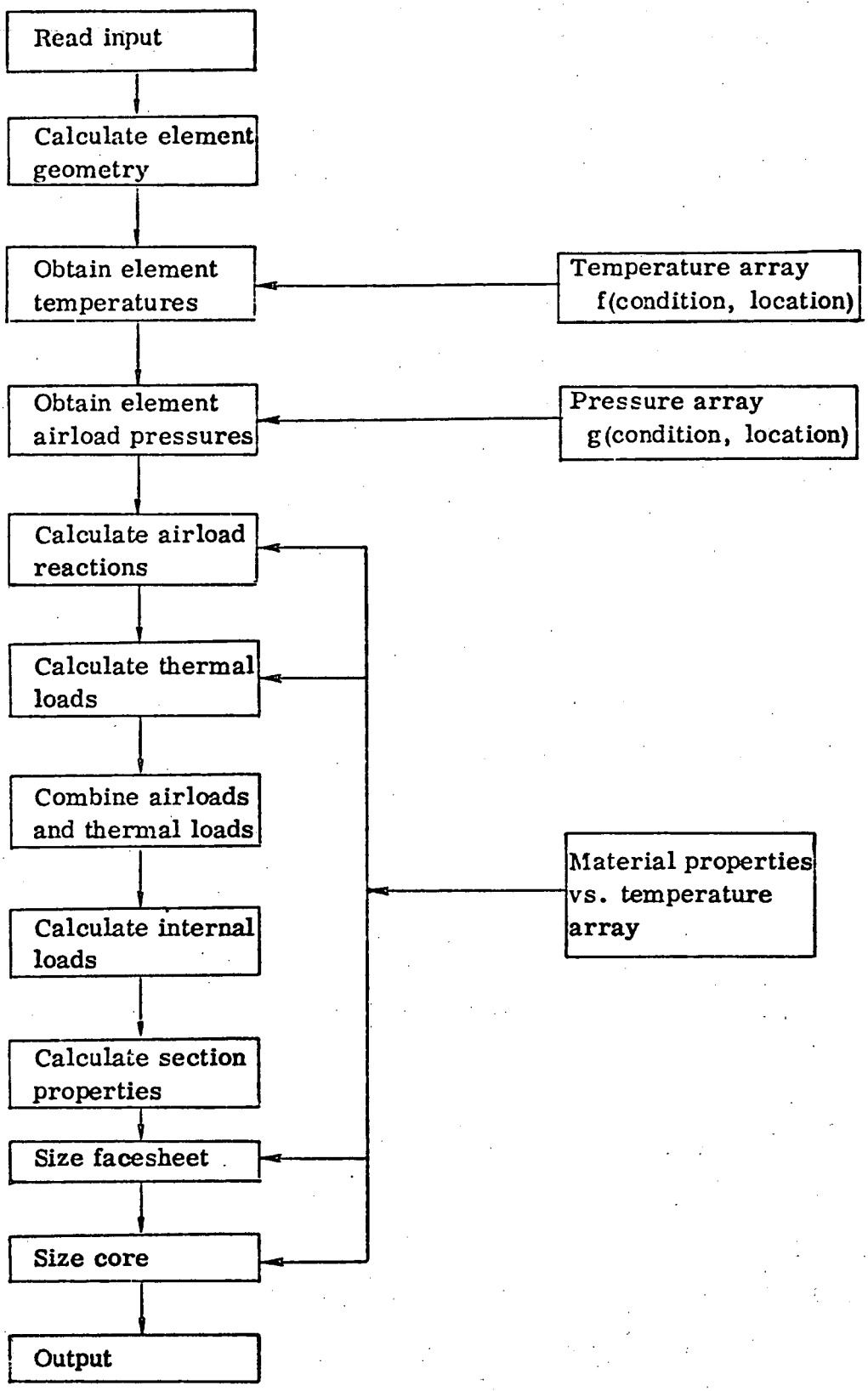

Figure 2-56. Stress Routine for Carbon-Carbon Leading Edge

Element temperature data, including inner and outer facesheet temperatures, is computed throughout the trajectory as part of the thermodynamic analysis. Temperature changes are found using an input stress-free temperature. Material properties are calculated from a table lookup as a function of temperature, and properties for a particular element are selected based on the temperature of the outer facesheet of the element.

The redundant fixed-end reactions due to airloads are found using the principles of statics and virtual forces. The reactions (forces: R_{xu}, R_{zu}, R_{xL}, and R_{zL}, and moments: M_{yu}, M_{yL}) at the upper and lower ends of the leading edge model are solved from six simultaneous equations

$$R_{xu} + R_{xL} + \sum_{i=1}^{i=11} P_{ix} = 0 \tag{2-83}$$

$$R_{zu} + R_{zL} + \sum_{i=1}^{i=11} P_{iz} = 0 \tag{2-84}$$

$$M_{yu} + M_{yL} + \sum_{i=1}^{i=11} (P_{iz}\,\chi_i - P_{ix}\,Z_i) = 0 \tag{2-85}$$

$$\sum_{i=1}^{i=11} \left(\left\{ M_{yL} + R_{xL} Z_i - R_{zL} \chi_i - \sum_{j=1}^{j=i-1} \left[P_{jx}(Z_i - Z_j) + P_{jz}(\chi_i - \chi_j) \right] \right\} \left\{ \frac{L_i}{E_i} \right\} \right) = 0 \tag{2-86}$$

$$\sum_{i=1}^{i=11} \left(\left\{ M_{yL} + R_{xL} Z_i - R_{zL} \chi_i - \sum_{j=1}^{j=i-1} \left[P_{jx}(Z_i - Z_j) + P_{jz}(\chi_i - \chi_j) \right] \right\} \left\{ \frac{Z_i L_i}{E_i} \right\} \right) = 0 \tag{2-87}$$

$$\sum_{i=1}^{i=11} \left(\left\{ M_{yL} + R_{xL} Z_i - R_{zL} \chi_i - \sum_{j=1}^{j=i-1} \left[P_{jx}(Z_i - Z_j) + P_{jz}(\chi_i - \chi_j) \right] \right\} \left\{ \frac{-\chi_i L_i}{E_i} \right\} \right) = 0 \tag{2-88}$$

Thermal loads are found by calculating the unrestrained thermal deflections and then applying the principle of virtual work.

$$\delta_{xu} = \sum_{i=1}^{i=11} \frac{-L_i\,\alpha_i\,(\Delta T_{Ai} + \Delta T_{Bi})}{2} \sin \theta_i \tag{2-89}$$

$$\delta_{zu} = \sum_{i=1}^{i=11} \frac{L_i \alpha_i (\Delta T_{Ai} + \Delta T_{Bi})}{2} \cos \theta_i \tag{2-90}$$

$$\phi_u = \sum_{i=1}^{i=11} \frac{L_i \alpha_i (\Delta T_{Ai} - \Delta T_{Bi})}{h} \tag{2-91}$$

Combining the airloads and thermal loads, the internal load distribution is obtained.

$$P_i = \left[(R_{xL} + R_{xLT}) \sin \theta_i - (R_{zL} + R_{zLT}) \cos \theta_i + \sum_{j=1}^{j=i-1} (P_{jx} \sin \theta_i - P_{jz} \cos \theta_i) \right] \tag{2-92}$$

$$M_i = \left[M_{yL} + M_{yLT} + (R_{xL} + R_{xLT}) Z_i - (R_{zL} + R_{zLT}) \chi_i + \sum_{j=1}^{j=i-1} (P_{jx} Z_i - P_{jz} \chi_i) \right] \tag{2-93}$$

$$V_i = \left[(R_{xL} + R_{xLT}) \cos \theta_i - (R_{zL} + R_{zLT}) \sin \theta_i + \sum_{j=1}^{j=i-1} (P_{jx} \cos \theta_i - P_{jz} \sin \theta_i) \right] \tag{2-94}$$

The facesheet thickness is sized for combined axial load and bending on the sandwich section. The core material is not included in the section property and sizing calculations for facesheet thickness. Thicknesses are sized for all elements and load conditions considering the following failure modes: tension, block compression and compression buckling. The largest value of skin thickness is selected as typical of the inner and outer facesheets for all the elements at the span location being considered.

For each load condition called during the trajectory, calculate

$$N_{1_i} = \frac{P_i}{2} + \frac{M_i}{0.884\, h} \tag{2-95}$$

$$N_{2_i} = \frac{P_i}{2} - \frac{M_i}{0.884\, h} \tag{2-96}$$

(strength)

$$t_{1_i} = \frac{N_{1_i}}{F_i} \qquad t_{2_i} = \frac{N_{2_i}}{F_i} \tag{2-97}$$

where

$$F_i = \begin{cases} F_{Tu_{11_i}} & \text{if N is (+)} \\ F_{eu_{11_i}} & \text{if N is (-)} \end{cases}$$

$F_{Tu_{11i}}$ and $F_{cu_{11i}}$ are based on T_{Ai}.

(buckling)

For all values of N_i which are negative, calculate

$$t_{3_i} = \left[\frac{0.380\, h^2\, |N_i|}{E_{11_i}} \right]^{1/3} \tag{2-98}$$

The thickness is then calculated as the largest of either t_{1_i}, t_{2_i}, or t_{3_i}.

The sheet thickness of the truss core diagonals is calculated considering shear and crushing due to bending. Thicknesses are sized for all elements and load conditions, and the largest value is selected as typical for all elements at the given span location.

For each load condition, calculate

Shear

$$t_{c1_i} = \frac{V_i}{2\, F_{su_i}} \tag{2-99}$$

Crushing

$$H = h - t_f \tag{2-100}$$

$$W_{c_i} = \frac{M_i}{H} \left[\frac{M_i}{E_{11_i}} + \frac{1}{r_i} \right] \tag{2-101}$$

For elements i = 4, 5, 6, 7, 8, set $r_i = r$

For elements i = 1, 2, 3, 9, 10, 11, set $r_i = 100$

$$t_{c2_i} = \frac{(h - 2t_f)\, W_{c_i}}{1.50\, F_{eu_{11_i}}} \tag{2-102}$$

The core thickness is then chosen as t_{c1i} or t_{c2i}, whichever is greater.

2.2.1.3 Passive Cooling Systems - Phase Change Material. The primary task performed during this investigation on the phase change material (PCM) system was the thermodynamic analysis of the phase change. No stress analysis was indicated or performed.

An analytical model has been developed for predicting the transient one-dimensional thermal performance of a thermal protection system utilizing a phase change material (PCM) in the backup structure. The heat protection system is considered to consist of either an ablating material or a reusable surface insulation (RSI) and a backup structure or substrate. The backup material is considered to consist of at least two face sheets with a PCM in between. Also, a honeycomb filler material (aluminum or titanium) can be used to contain and in some cases to improve the thermal conductivity of the PCM.

The computer subroutine used is a modified version of Curry's Charring Ablator Program described in Reference 3. This modified form of the program (P5570) can handle one ablating or non-ablating material (RSI) and a maximum of 6 backup materials including the bond. Conduction, radiation and/or convection are allowed between the materials except for the PCM; only conduction is allowed into and out of the PCM. In addition, the program specifies that there must be at least one material behind and one material before the PCM in the backup structure. The thermal properties of all materials in the backup structure are temperature dependent.

The basic governing differential equations for the charring ablator analysis, their implicit finite difference formulation, the program input and output, the FORTRAN program statements and nomenclature are presented in Reference 3. The present discussion contains the analytical expressions required to handle the latent heat of fusion or transition (i.e., for a solid/solid phase change material) of the PCM, calculation of the equivalent thermal properties of PCM and filler material and the changes required in the mathematical procedure to handle the known phase change temperature in the backup structure.

The set of algebraic equations resulting from the implicit finite difference formulation of the governing partial differential equations and boundary conditions is solved by the Gauss' elimination method specialized for a tridiagonal matrix.

Figure 2-57 is a schematic of the thermal protection system considered in this analysis. The ablating surface is used in conjunction with a backup structure which consists of three backup materials in the present analysis. It should be noted that the entire system may be composed of noncharring materials.

The backup structure may consist of up to six different materials (with or without air gaps) with a maximum of nine nodes per material. The PCM constitutes a special kind of backup material for which heat transfer in and out can only occur by conduction. The PCM itself must contain at least three nodes; if the program user wishes to simulate face sheets on the PCM, each of these too must contain a minimum of three nodes.

The heat balance equations for a typical node in the backup structure is given by the one-dimensional Fourier conduction (neglecting any heat generation term). Thus

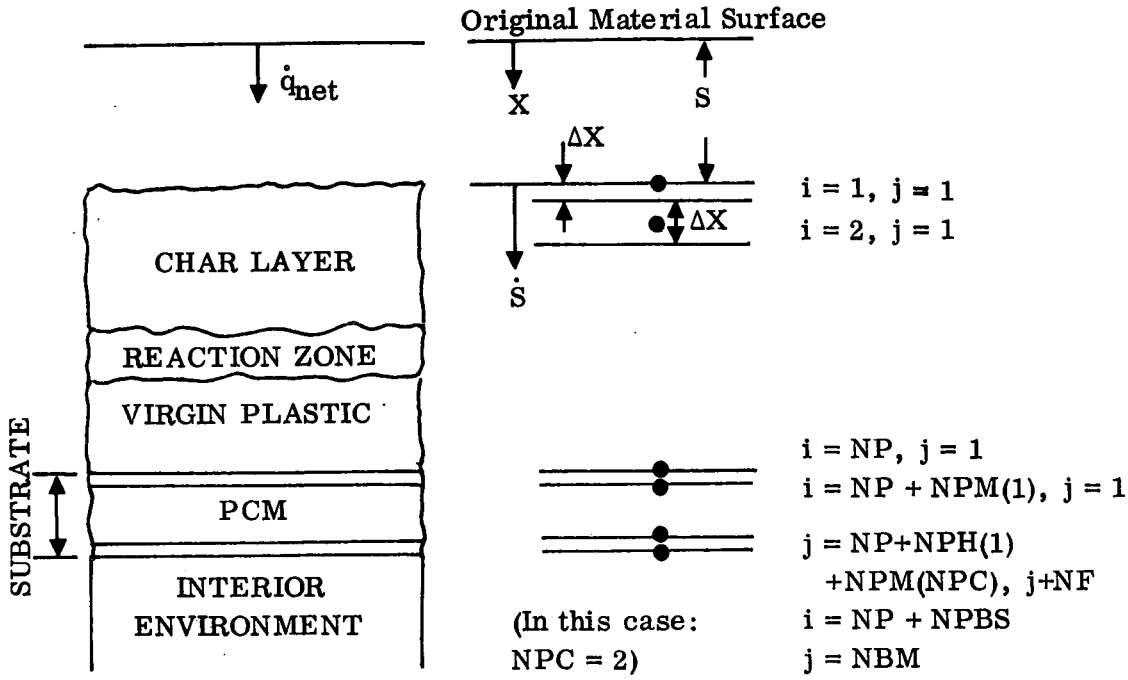

Figure 2-57. Schematic Diagram of Charring Ablator Thermal Protection System With PCM in the Backup Structure

$$\frac{\partial}{\partial x}\left[k\,\frac{\partial T}{\partial x}\right] = \rho\, C_p\,\frac{\partial T}{\partial \theta} \tag{2-103}$$

The implicit difference form of Equation 2-103 for the i^{th} node is

$$\frac{T'_{i-1} - T'_i}{\frac{\Delta x}{2k_{i-1}} + \frac{\Delta x}{2k_i}} - \frac{T'_i - T'_{i+1}}{\frac{\Delta x}{2k_i} + \frac{\Delta x}{2k_{i+1}}} = \rho\, C_p\,\frac{\Delta x\,(T'_i - T_i)}{\Delta \theta} \tag{2-104}$$

where the prime superscript denotes values at the end of the time step.

$$\Delta\theta = \theta' - \theta \tag{2-105}$$

Corresponding equations for each node in the system are solved simultaneously to calculate the temperature at each node.

Rearranging Equation 2-104 to put the unknown temperatures on the left hand side gives

$$\left[\frac{1}{\frac{\Delta x}{2k_{i-1}}+\frac{\Delta x}{2k_i}}\right] T'_{i-1} - \left[\frac{1}{\frac{\Delta x}{2k_{i-1}}+\frac{\Delta x}{2k_i}} + \frac{1}{\frac{\Delta x}{2k_i}+\frac{\Delta x}{2k_{i+1}}} + \frac{\rho_i C_{p_i} \Delta x}{\Delta\theta}\right] T'_i$$

$$+\left[\frac{1}{\frac{\Delta x}{2k_i}+\frac{\Delta x}{2k_{i+1}}}\right] T'_{i+1} = -\left[\frac{\rho_i C_{p_i} \Delta x}{\Delta\theta}\right] T_i \qquad (2\text{-}106)$$

which is of the form

$$A\, T'_{i-1} + B\, T'_i + C\, T'_{i+1} = D \qquad (2\text{-}107)$$

The computer program generates a tridiagonal matrix for the nodes of the system, e.g.,

$$\begin{aligned}
B_1 T_1 + C_1 T_2 &= D_1 \\
A_2 T_1 + B_2 T_2 + C_2 T_3 &= D_2 \\
A_3 T_2 + B_3 T_3 + C_3 T_4 &= D_3 \\
&\vdots \\
A_N T_{N-1} + B_N T_N &= D_N
\end{aligned} \qquad (2\text{-}108)$$

and solves the simultaneous equations.

Since the PCM is specified to consist of 3 nodes, the material is lumped into two half-nodes on each face and one complete interior node. The thermodynamic properties and latent heat of fusion or transition of the PCM materials can be obtained from References 38 and 13. The equivalent thermodynamic properties of the PCM and filler material is computed according to the method given in Reference 38. Thus

$$k_{eq} = k_{PCM} + (k_F - k_{PCM})\, F_{FR} \qquad (2\text{-}109)$$

$$C_{p_{eq}} = C_{p_{PCM}} + (C_{p_F} - C_{p_{PCM}})\, F_{FR} \qquad (2\text{-}110)$$

$$\rho_{eq} = \rho_{PCM} + (\rho_F - \rho_{PCM})\, F_{FR} \qquad (2\text{-}111)$$

where F_{FR} is the filler fraction given by

$$F_{FR} = A_F/A_T \qquad (2\text{-}112)$$

Inherent in these equations are the following assumptions: (1) the contact resistance between filler material and the face plates is negligible, and (2) three-dimensional heat

transfer effects are neglected, based on the assumption that the filler materials are so closely spaced that these effects are negligible. The errors introduced by these assumptions are discussed in Reference 13.

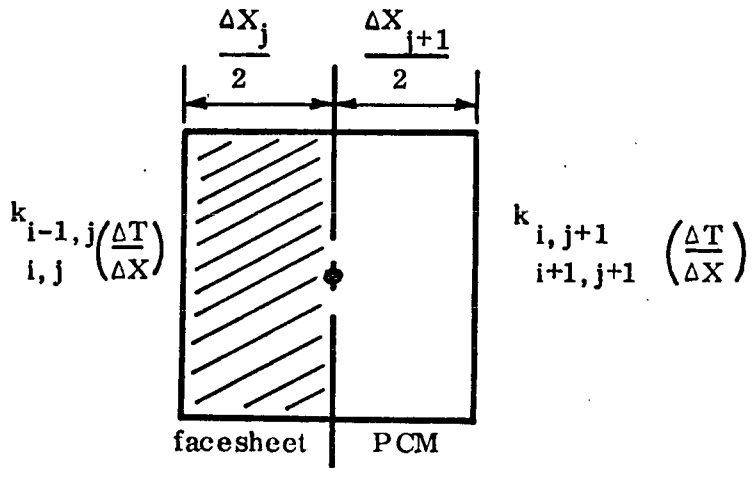

Figure 2-58. Nodal Schematic of PCM

When the temperature of each node in the PCM reaches the melt or transition temperature, it is assumed that the latent heat of fusion or transition (solid/solid phase change material) is absorbed by the individual nodes at constant temperature equal to the melt temperature.

The physical model for the last node of the front face sheet and first node in the backup structure is shown in Figure 2-58.

For this interface

$$T'_{i,j} = T'_{i,j+1} = T_{MELT} \tag{2-113}$$

where T_{MELT} is the melt temperature of the PCM.

The heat balance equation for this node during the phase-change process is

$$\frac{T'_{i-1,j} - T'_{i,j}}{\frac{\Delta x_j}{2k_{i-1,j}} + \frac{\Delta x_j}{2k_{i,j}}} - \frac{T'_{i,j+1} - T'_{i+1,j+1}}{\frac{\Delta x}{2k_{i,j+1}} + \frac{\Delta x}{2k_{i,j+1}}} = \frac{\Delta Q_{pc}}{\Delta\theta} \tag{2-114}$$

where i is the nodal index of the j^{th} material.

Rearranging Equation 2-114 and noting Equation 2-113 gives

$$\left[\frac{1}{\frac{\Delta x_j}{2k_{i=1,j}} + \frac{\Delta x_j}{2k_{i,j}}}\right] T'_{i-1,j} + \left[\frac{1}{\frac{\Delta x_{j+1}}{2k_{i,j+1}} + \frac{\Delta x_{j+1}}{2k_{i+1,j+1}}}\right] T'_{i+1,j+1} = \frac{\Delta Q_{pc}}{\Delta\theta}$$
$$+ \left[\frac{1}{\frac{\Delta x_j}{2k_{i-1,j}} + \frac{\Delta x_j}{2k_{i,j}}} + \frac{1}{\frac{\Delta x_{j+1}}{2k_{i,j+1}} + \frac{\Delta x_{j+1}}{2k_{i+1,j+1}}}\right] T_{MELT} \tag{2-115}$$

where ΔQ_{pc} is the heat fusion absorbed by the PCM material in the node during the time interval $\Delta\theta$. Equation 2-115 also applies for the last node of the PCM and the first node of the back face sheet. For the interior node of the PCM a similar analysis leads to

$$\left[\frac{1}{\frac{\Delta x_j}{2k_{i-1,j}}+\frac{\Delta x_j}{2k_{i,j}}}\right] T'_{i-1,j} + \left[\frac{1}{\frac{\Delta x_j}{2k_{i,j}}+\frac{\Delta x_j}{2k_{i+1,j}}}\right] T'_{i+1,j} = \frac{\Delta Q_{pc}}{\Delta\theta}$$

$$+\left[\frac{1}{\frac{\Delta x_j}{2k_{i-1,j}}+\frac{\Delta x_j}{2k_{i,j}}}+\frac{1}{\frac{\Delta x_j}{2k_{i,j}}+\frac{\Delta x_j}{2k_{i+1,j}}}\right] T_{MELT} \qquad (2\text{-}116)$$

Since the melt temperature is known, one column of coefficients A, B, C in the tri-diagonal matrix becomes zero when the PCM starts to melt. Typically, if $T_4 = T_{MELT}$, we have

$$\begin{aligned}
B_1 T_1 + C_1 T_2 &= D_1 \\
A_2 T_1 + B_2 T_2 + C_2 T_3 &= D_2 \\
A_3 T_2 + B_3 T_3 + 0 &= D_3 \\
\text{----------} & \\
A_4 T_3 + 0 + C_4 T_5 &= D_4 \qquad (2\text{-}117) \\
\text{----------} & \\
0 + B_5 T_5 + C_5 T_6 &= D_5 \\
\vdots \quad \vdots & \quad \vdots \\
A_N T_{N-1} + B_N T_N &= D_N
\end{aligned}$$

Since one column is all zeros, the overall matrix contains a singularity and this matrix cannot be solved the usual way. To overcome the problem, the matrix can be split into two matrices and the Gauss Elimination Method can then be applied to each submatrix. For the particular example shown in Equation 2-117, T_3 would be obtained from solution of the upper submatrix, T_5 from the lower submatrix and T_4 is already known.

2.2.2 ACTIVE COOLING SYSTEM - ABLATOR

2.2.2.1 Stress Analysis. No new stress analysis was performed for the ablator system. The substrate is sized to provide the total strength requirement of the ablator/substrate combination to satisfy the condition at the end of entry where the ablator has been theoretically consumed. The stress analysis already existing in the computer program is used for this.

2.2.2.2 Thermal Analysis. The thermodynamic analysis of the ablating TPS is performed by the one-dimensional, implicit computer code developed by Curry and described in detail in the technical note NASA TN D-3150 (Reference 3). The finite difference approximation to the energy equation is written in backward difference form to allow simultaneous solution of the temperature distribution at the new time step in terms of those at the previous time. The purpose of employing this technique is to overcome the difficulties of numerical instability since the method is stable for all time steps. In the original NASA computer code, heating rates were input using cold wall values uncorrected for heat blockage due to the addition of pyrolysis gases to the boundary layer. This cold wall rate is expressed as

$$q = h\,(\tilde{i}_o - i_{300}) \tag{2-118}$$

where the enthalpy $\tilde{i}_o$ is a fictional total enthalpy, the sum of the enthalpy of air at 300K and the freestream kinetic energy. The hot wall convective heating rate is then determined by multiplying the above expression by the fraction

$$\frac{\tilde{i}_o - i_w}{\tilde{i}_o - i_{300}} \tag{2-119}$$

where the term i_w is just the instantaneous wall enthalpy. Such a procedure assumes that the convective heating rate coefficient is only a weak function of temperature. Two additional options have been added during the course of these investigations. The first allows the input of hot wall heating rates thus bypassing the correction from cold wall values and the need to input vehicle velocity as a function of time. The second option is simply the use of hot wall aerodynamic heating rates predicted by the program itself.

In any case, the hot wall heating rates finally determined by the program must also be corrected for the blockage effect of both the exhausting pyrolysis gases and charring ablator as well as for radiation to deep space. The latter correction is simply effected by subtracting off the term $\sigma \epsilon T^4_w$. However, the blowing effect correction incorporated into the TPS sizing routine is different from that originally developed by Curry, and for this reason it will be described here in some detail.

The method for predicting blowing effectiveness published in NASA TN D-3150 is

$$\dot{q}_{block} = \eta\, \dot{m}_g\, (\tilde{i}_o - i_w) \tag{2-120}$$

where the driving potential is the difference between the fictional total enthalpy and the wall enthalpy. The heat blockage is also a function of the mass flow of the released pyrolysis gases and a coefficient η which has a wide range of possible values. Since the heat blockage term is subtracted from the incident heating rate, a high enough value of η can effect a negative net heating rate. Unfortunately, little information is available concerning realistic values of the blowing effectiveness coefficient as used in the context of Equation 2-120.

Therefore, another blowing effective relationship has been incorporated after a suggestion of Curry. The expression is

$$\frac{S_T}{S_{To}} = \frac{\xi}{e^{\xi} - 1} \tag{2-121}$$

where S_T is the Stanton number, the subscript "o" denotes the no-blowing case, and the parameter ξ is given by

$$\xi = f_{BLOW}\left[\frac{28.97}{\tilde{M}}\right]^{\beta} \rho_w v_w \frac{1}{S_{T_o}} \tag{2-122}$$

The parameters f_{BLOW} and β are given in the following table for laminar or turbulent flow.

	Laminar	Turbulent
f_{BLOW}	1.44	0.87
β	0.25	0.20

The term $\tilde{M}$ is the molecular weight of the mixture of pyrolysis gases and char release to the boundary layer, and the product $\rho_w v_w$ denotes the mass flow released.

An immediate advantage observed in the relationship of Equation 2-121 is that the ratio of Stanton numbers for the blowing and no blowing case now varies between zero and one, the former limit corresponding to massive blowing and the latter to the no blowing case.

In order to include the rigorous approach of the charring ablator code in describing ablator performance yet keep the computer program core size and operational speed within realistic limits, it was necessary to decrease the size of the ablation subroutines and eliminate a number of computations. Hence, the original scheme which allowed up to 50 nodes in the ablation material and 12 backup structure materials with 10 nodes each was reduced to one which limited the ablator to 10 nodes with six backup materials of up to 4 nodes each. In addition, a number of other options of the original program were also eliminated. These include the plot routines, the location of constant temperature lines as a function of time, the determination of temperatures at discrete points in the model to correlate ablator behavior with measured thermocouple data, and the input of a linear initial temperature distribution. This last capability is now limited to either a constant temperature distribution or specific input values for each node of the model.

Taken altogether, the computer code simplifications and reduction of array sizes resulted in a reduction in core size from 65.6K to 32.5K octal. Program accuracy or speed was unaffected by these changes. A number of cases were run over a 300 second trajectory to assess the effects of these changes. The resulting temperatures of the

surface node and the backup structures are shown in Figure 2-59. Little difference can be seen in the surface temperature for the three nodal spacings examined and the temperatures predicted for the backup structure are identical. The time at which the surface node disappears is the same for all cases investigated. The depth of surface recession is given in Figure 2-60. Again, little difference is seen between models. However, in Figure 2-61, the gas ablation rate (the rate at which pyrolysis gases are generated) varies markedly between the models when using the original blowing effectiveness model presented in NASA TN D-3150. The time increment of the computation was also varied in an attempt to stabilize the solution; the predicted gas ablation rate is not converging as either the nodal geometry or the time increment is decreased. The new blowing effectiveness equations were input to the main subroutine of the charring ablator program. The cases of the convergence study were rerun using the new method, but oscillations in the generation rate of pyrolysis gases and the net heating were still observed (Figures 2-62 and 2-63). Nevertheless, the temperature response of the ablator for the variation in the number of nodes (Figures 2-64 and 2-65) do not vary from each other catastrophically, especially in the backup material. Hence, the model of reduced size (e.g., a maximum of ten nodes in the ablator material) was adapted to P5490B.

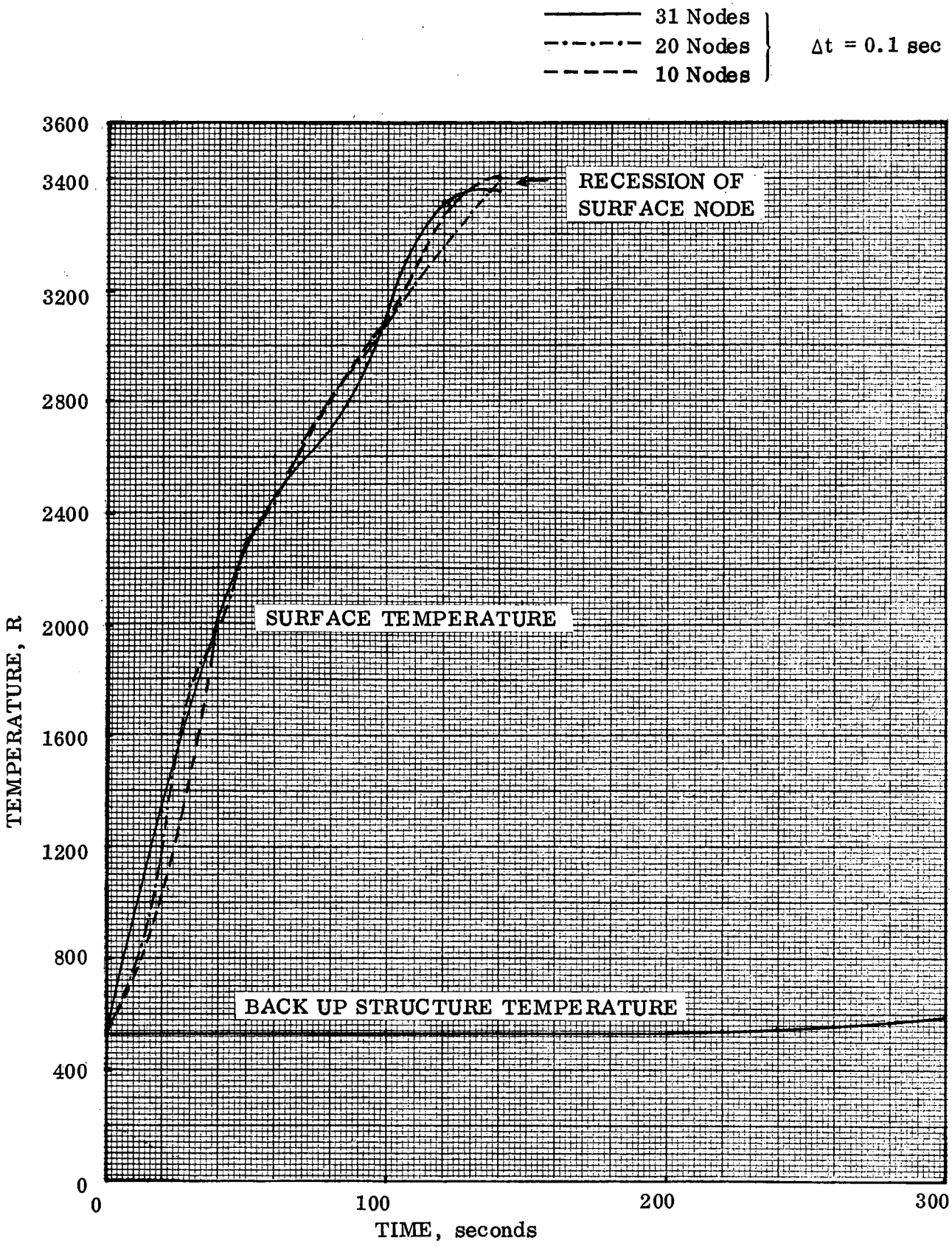

Figure 2-59. Convergence Study of Ablator Temperatures

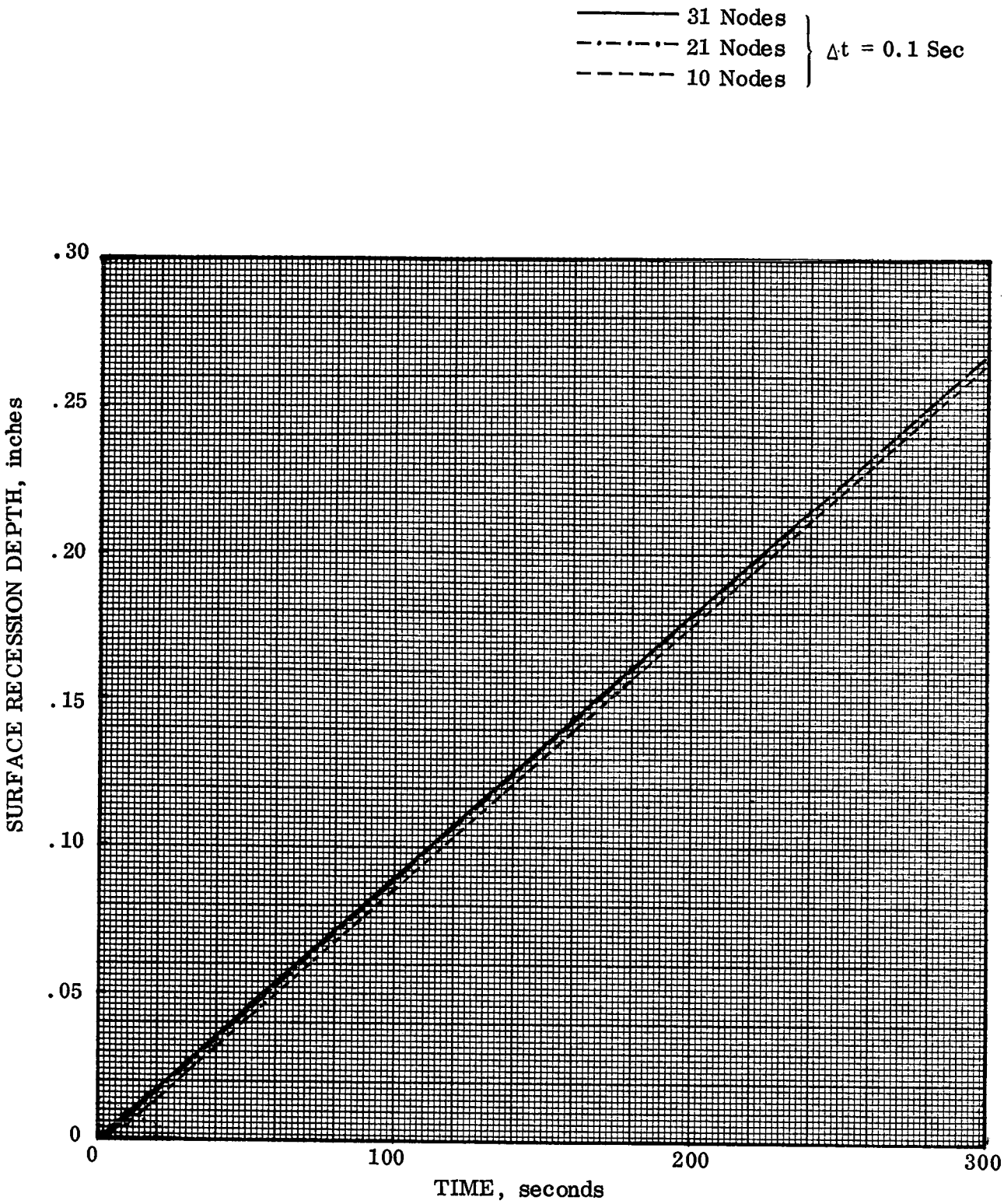

Figure 2-60. Convergence Study of Surface Recession Depth

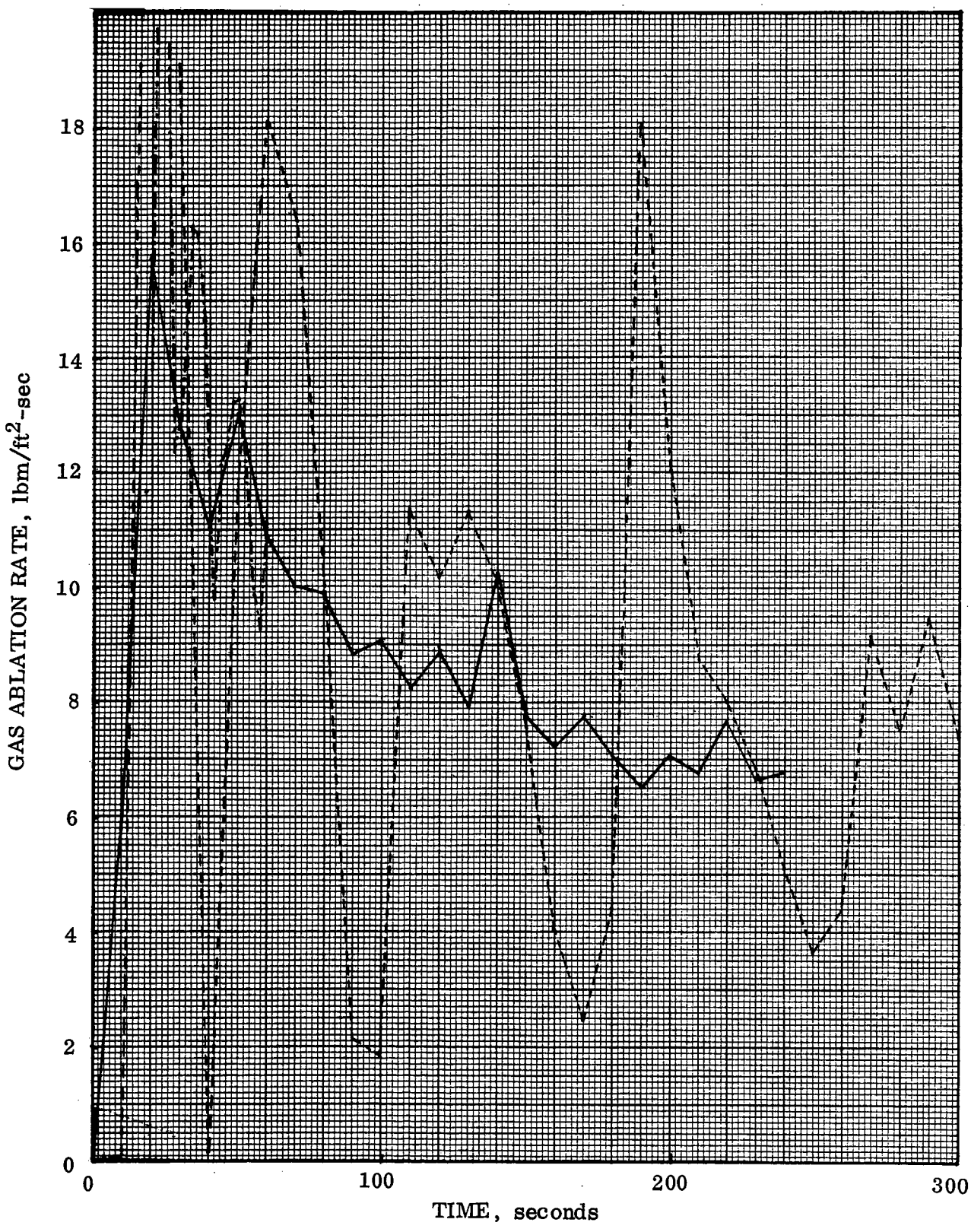

Figure 2-61. Convergence Study of Gas Ablation Rate

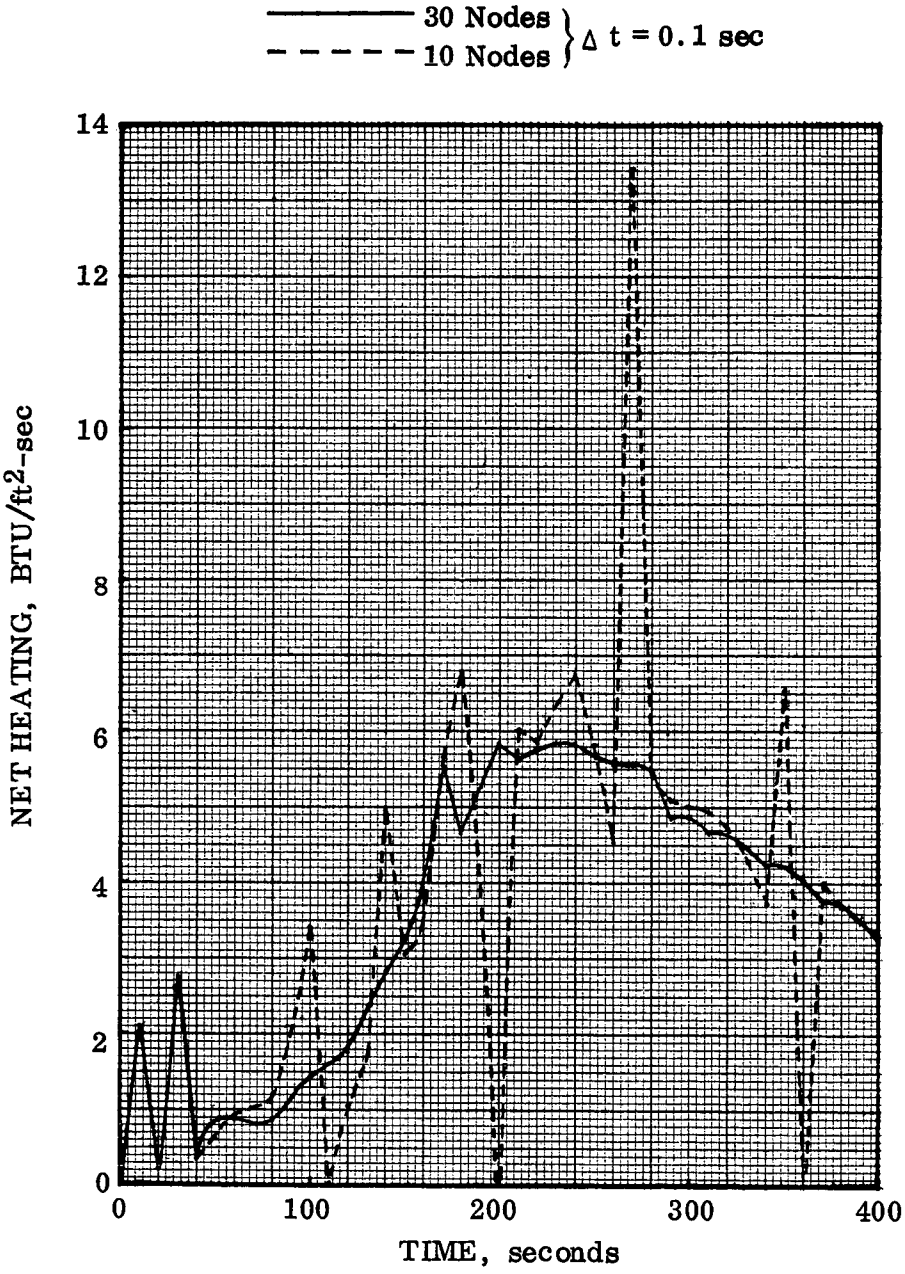

Figure 2-62. Convergence Study of Ablator Net Heating Rate for Laminar Blowing

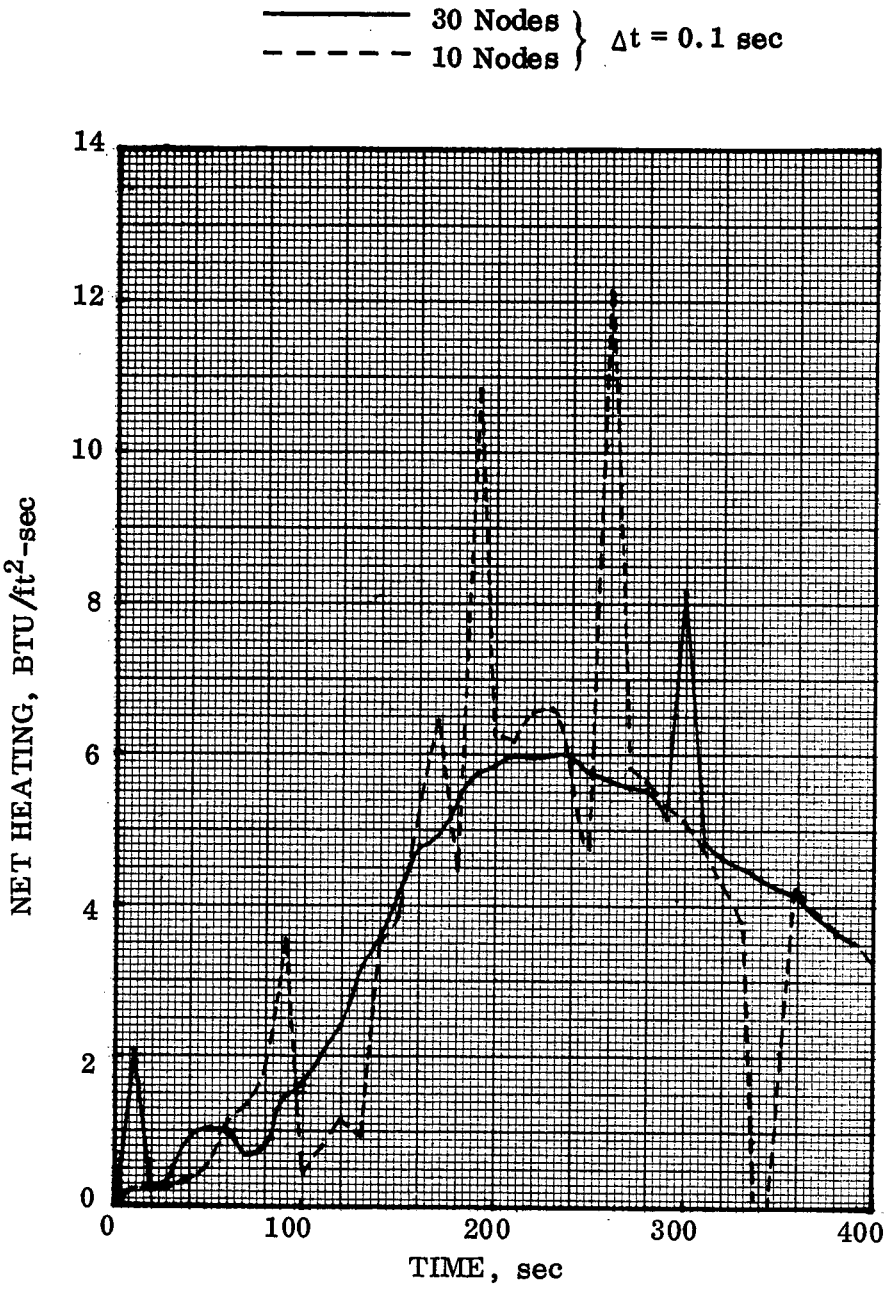

Figure 2-63. Convergence Study of Ablator Net Heating Rate for Turbulent Blowing

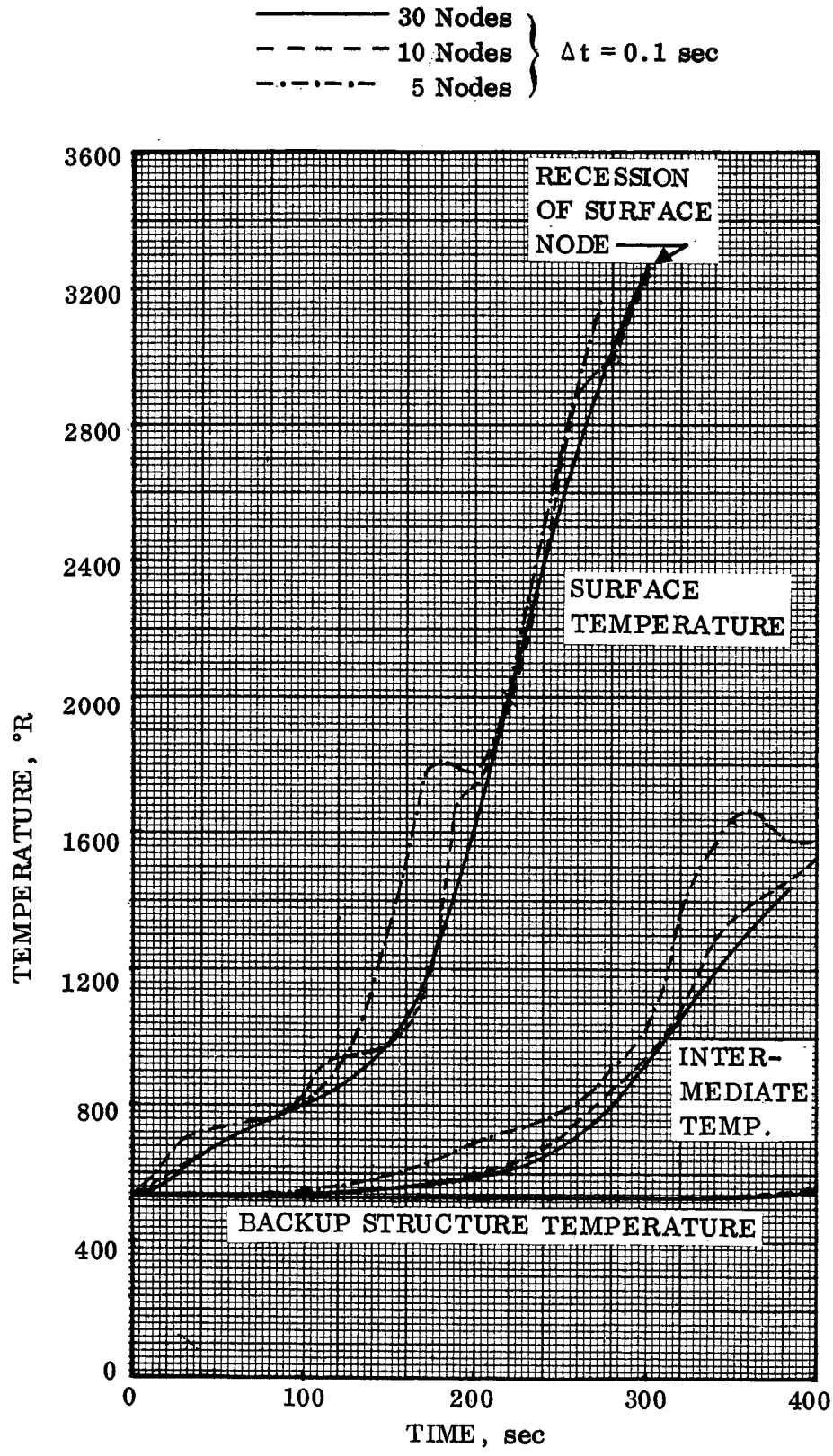

Figure 2-64. Convergence Study of Ablator Temperatures for Laminar Blowing

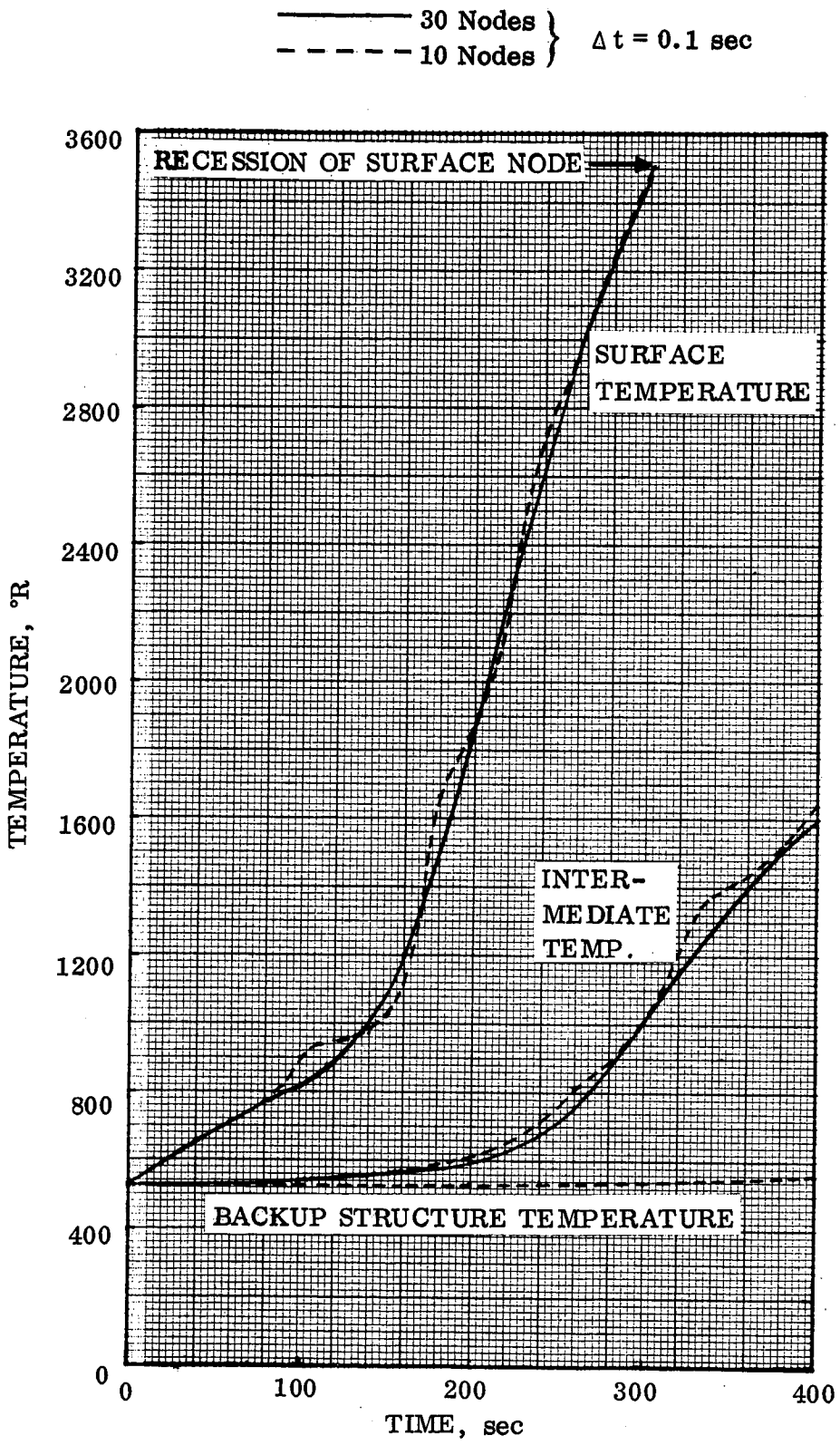

Figure 2-65. Convergence Study of Ablator Temperatures for Turbulent Blowing

SECTION 3

PROGRAM APPLICATIONS

3.1 SHORT TERM IMPROVEMENTS

During preliminary sensitivity and optimization runs on the metallic TPS cover panels, consideration was given to developing automatic methods to speed the overall assimilation of TPS design data and to ease the program user's task in generating this information. Sample cases were run varying panel and insulation thicknesses and panel sizes. The results of these studies included system performance parameters such as stress and temperatures, panel weight, manufacturing cost, and total program development cost. For a given panel material, configuration, and location on the vehicle, the principal contributor to system cost and weight is its size. The optimum system was chosen as the one with either minimum weight or cost. Usually, with a little foresight and/or experience on the program user's part, this minimum could be established with three sample cases, (i.e.,three test points). These points were then plotted or sketched quickly by hand, and if the minimum could not be seen, the concavity of the plotted results indicated at which end of the data (i.e., smaller or larger panel sizes) additional designs had to be run. Similar results were also experienced when sizing insulation or panel thicknesses to meet temperature or stress constraints. Experience at running the program indicated that it was far easier to determine the minimum insulation thickness for a prescribed temperature constraint simply by plotting the temperature of interest as a function of material thickness (Figure 3-1).

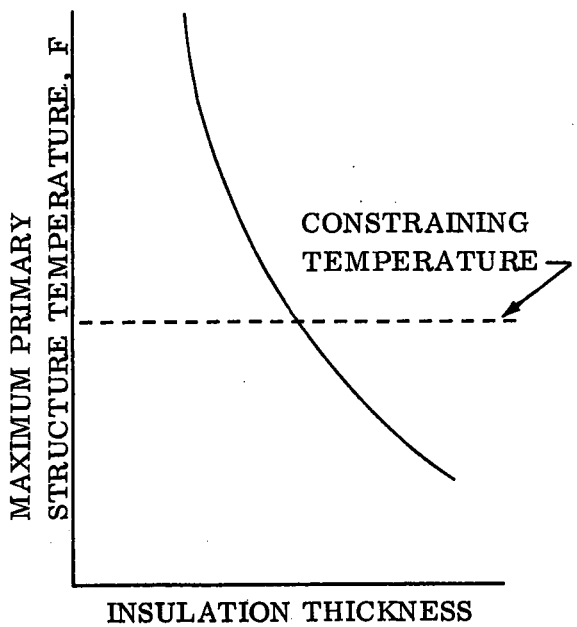

Figure 3-1. Example of Primary Structure Temperature Versus Insulation Thickness

Techniques which were considered to replace the manual decision-making process included automatic plotting of the results, curve fitting results and differentiating the resultant curve to ascertain the minimum, or adaptation of an iterative procedure to determine the minimum value of the driving parameter. The first of these methods, automatic plotting,was rejected because such procedures would limit the sizing routines to particular computing systems, but, more important, was the delay of up to 24 hours caused by waiting for results to be plotted and reproduced photostatically. Another alternative is also available, on most systems, use of a

cathode ray tube, but for the machine on which the routine was developed (the CDC 6400) core requirements of 40K octal for such a capability would require such drastic overlaying of the program as to make its use inefficient. In addition, there might be a tendency for the user to make rather rapid judgments in an effort to run the next point and size the system thus leading to errors in judgment and added machine time and cost. It is felt that a little contemplation in deciding upon additional test cases to be run should the initial values prove insufficient is a more efficient method than running a large number of cases to determine one optimum design.

The concept of curve fitting results to find the design point was also considered. For the case of determining the minimum insulation thickness to satisfy a given temperature constraint (Figure 3-1) the three data points must be curve fit, and the intersection of this curve and the constraint line found either graphically or numerically. To find an optimum panel size, Figure 3-2, the curve which fits the data must be differentiated to find its minimum. In either case, extrapolation of the results is dangerous at best

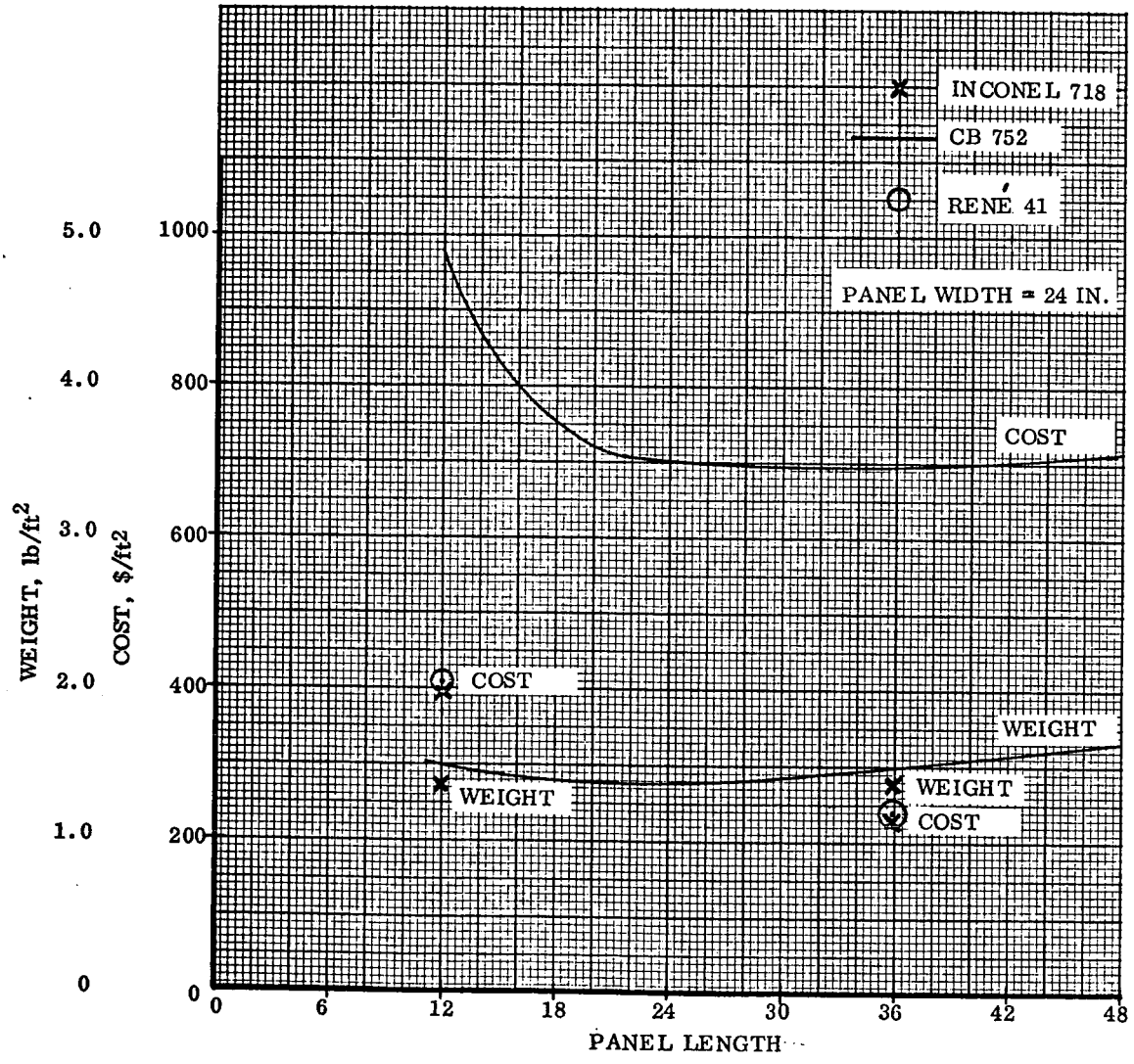

Figure 3-2. Metallic Optimization Study Results

if the solution is not bracketed. If convergence of the procedure is not successful, a great deal of machine time can be wasted getting additional data points.

An iterative procedure offers all the disadvantages of curve fitting or graphically representing data. The expense of running enough cases to establish the direction of the iterative procedure precludes economical use of the program.

Thus it was concluded that the most efficient manner to size the TPS was to take advantage of the man-machine interplay by allowing the program user to exercise his discretionary judgment in running point design.

3.2 FORMAL OPTIMIZATION PROCEDURES

As a result of studying methods to automatically size the TPS, it was concluded that a large number of cases would have to be run to allow the proper system evaluation by any formal optimization procedure. Since such methods prevented economical program use, this portion of the study effort was eliminated by mutual consent of the contractor and monitor.

3.3 OPTIMIZATION STUDIES

In the previous section, the investigation of formalized optimization procedures was discussed. It was concluded at the end of this study that the wide variety of parameters affecting the performance of the TPS precluded the use of anything but the simplest of procedures. The basic technique recommended at conclusion of the last contract study was to vary the panel thickness to adequately withstand both the mechanical and thermal stresses and to vary the insulation thickness to satisfy temperature constraints. All other variables such as panel size, configuration, materials, and the like were maintained at constant value. The sizing of the panel and insulation thicknesses to satisfy temperature and structural constraints was done automatically simply by adding to material thicknesses until the constraints were met. However, no check was made to see if the TPS was over design. The optimum panel configuration was determined simply by varying panel size and looking either for minimum weight or cost of the TPS. The technique has been made more straight-forward in the new computer code by requiring that the program user determine the proper panel thicknesses in a series of computer runs by plotting, for example, the constraining temperature as a function of insulation thickness. In this manner, all the information obtained on TPS performance for the off-design thicknesses could be obtained, and in addition, the exact thickness to meet the temperature constraint can be determined. Observation of the stress values and design factors for panel and supporting substrate configurations allow reaching similar design conclusions for the stress supporting parts of the TPS configuration.

For the case of the metallic panels, the thickness is still varied by increasing its previous value by a Newton-Raphson interpolation procedure to obtain all positive

values of the stress design factors. However, for the case of the RSI, although both discrete element and finite element stress analyses are performed, no automatic sizing is done - this is performed by the program user.

Optimization and sensitivity studies are performed by the user by varying panel size, material properties, and configuration (six different metallic panel cross-section geometries are provided) in a series of computer runs. The program sizes panel and insulation thicknesses. An optimum design is then identified as the one giving either minimum weight or cost as a function of the parameters being varied for the investigation. Sensitivity studies are performed by noting the change in system weight or cost due to the variation in some independent variable such as trajectory or heating prediction method for an optimum panel configuration.

Some typical results are available for an optimization study performed on the bottom centerline of the orbiter vehicle for an integrally stiffened panel composed of coated Columbium, René 41, and Inconel 718. The panel is insulated with 6 pound per cubic foot Dynaflex. An underlaying aluminum tank constrained the system to a maximum temperature of 300° F here. The weight and manufacturing cost evaluated for a configuration that is 24 inches wide and of varying length is given in Figure 3-2. Cost of the coated Columbium panel comes out at approximately $700 per square foot and is relatively insensitive to panel length above a minimum value of approximately 20 inches. For smaller panel lengths, the cost of the supporting structure becomes excessive and drives the total system cost up. The two additional materials (Inconel 718 and René 41) indicated the same flat weight curve and relatively lower costs. Again, costs increase rapidly at the smaller panel sizes. The optimum value for both materials is a little over $200 per sq ft.

3.4 SENSITIVITY STUDIES

The prediction techniques used to design the TPS always have a degree of uncertainty caused by anything from the scatter of data used to correlate heat transfer prediction methods to the experimental error introduced while determining material properties. The system designer must account for these effects by either providing a margin of safety to allow for these contingencies or by limiting or refining mission constraints to avoid catastrophic failure due to the increased loads that may occur. The experience of previous TPS design work indicates that the compounded conservatism introduced by simply adding the margins required to provide system safety can lead to significant weight and performance penalties of the vehicle. To combat these penalties in both the weight and cost of the TPS, two tasks must be performed: (1) the penalties due to the performance prediction uncertainties must be established, and (2) a rational method of combining these penalties must be established since many of the uncertainties and associated penalties are not independent. It is the purpose of a sensitivity study to establish the penalties in system weight and cost due the uncertainties in system design.

Design uncertainties in the TPS itself can be separated into three categories: the environment, physical properties of the system itself, and operational and system characteristics. A partial list of these effects is given in Table 3-1. Parametric data gathered by establishing the weight and cost penalties due to variations in these uncertainties will establish the system sensitivities to these changes.

Table 3-1. TPS Uncertainty Factors

Environment
Laminar heating
Onset of transition to turbulent flow
Onset of fully developed turbulent flow
Turbulent heating
Separated flow heating
Local flow conditions
Trajectory dispersions
Roughness effects
Vehicle aerodynamic attitude
Local aerodynamic pressure loading
Venting pressure
Physical Properties
Material properties, (including conductivity, density, specific heat, surface emissivity, etc)
Material temperature limitations
Mechanical properties
Operations and System Characteristics
Reentry trajectory corridor
Attitude control system interactions
Related systems and structure thermal limits
Manufacturing, assembly and fabrication limitations
Reuse constraints
Inspection requirements
Initial structural temperatures

SECTION 4

CONCLUSIONS AND RECOMMENDATIONS

1. The computer program developed under this contract provides the user with a powerful tool to determine the minimum weight/cost TPS for a given application from a variety of alternate TPS concepts and alternate materials for a given concept.

2. An extensive parametric study should be performed on the current space shuttle vehicle to define the TPS concept, or combination of different concepts used at different locations on the vehicle which will yield the lowest cost TPS.

3. Formal optimization procedures, utilizing automated iterative loops with their attendant curve fitting or extrapolation routines do not appear to be compatible with the requirements for a computer program with an acceptable cost. Both the cost of performing the program verification (assuming one is developed), and then the operating cost when applied to a problem appear to be excessive when compared with a man-in-the-loop procedure.

SECTION 5

REFERENCES

1. Whitehead, K. D., "Computational Techniques for Design Optimization of Thermal Protection Systems for the Space Shuttle Vehicle: Volume I - Final Report," Convair Aerospace Div. of General Dynamics Report GDCA-DDB71-005, Sept., 1971.

2. Whitehead, K. D., "Computational Techniques for Design Optimization of Thermal Protection Systems for the Space Shuttle Vehicle: Volume II - User's Manual," Convair Aerospace Div. of General Dynamics Report GDCA-DDB71-005, Sept., 1971.

3. Curry, Donald M., "An Analysis of a Charring Ablator Thermal Protection System," NASA TND-3150, December 1965.

4. Black, W. E., "Radiative Thermal Protection System Development for Manned Reentry Spacecraft," GDC-ERR-1272, General Dynamics, Convair, Feb. 1969.

5. Lemley, Clark E., "Design Criteria for the Prediction and Prevention of Panel Flutter," Vol. 1, AFFDL Technical Report AFFDL-TR-67-140, August 1968.

6. Hess, R. W., "Preliminary Results of an Experimental Study of the Effects of Compressive Stress on Panel Flutter," NASA Langley Working Paper LWP-177, January 1966.

7. Kordes, E. E., Tuovila, W. J., and Guy, L. D., "Flutter Research on Skin Panels," NASA Technical Note D-451, September 1960.

8. "Space Shuttle Thermal Protection System Metallic Materials Data Book," GESP-561, General Electric, Cincinnati, Ohio.

9. Rusert, E. L., "Quarterly Technical Progress Report for Reusable Surface Insulation Thermal Protection Development for Shuttle," McDonnell Douglas Astronautics Co., St. Louis, Mo., MDC-E0488, 11 November 1971.

10. Kural, M., "Structural Analysis Methods and Preliminary Results on LI-1500/Bond/Substructure Composites," Report No. A984004, Lockheed Missiles and Space Co., Sunnyvale, Ca., 30 December 1970.

11. Michalak, R. J., "Mid-Term Report for Reusable Surface Insulation Thermal Protection System Program," GE-EYP009, 10 November 1971, General Electric Co., Philadelphia, Penn.

12. While, D. M., "Development of a Thermal Protection System for the Wing of a Space Shuttle Vehicle," Phase II Final Report, VMSC Report No. T143-5R-00124, 30 April 1972.

13. Hale, D. V., et al, "Phase Change Materials Handbook," NASA-CR-61363, Lockheed Missiles and Space Co., Huntsville, Alabama, Sept. 1971.

14. Scullen, R. S., "A Description of the Revised Aerodynamic/Structural Heating and Radiation Equilibrium Temperature Computer Program 3020," Convair Aerospace Div. of General Dynamics Report GDC-ERR-1336, December 1968.

15. Whitehead, K. D., "Computer Program 3020 Revision," Convair Aerospace Division of General Dynamics Report GDC-ERR-1416, December 1969.

16. Dunavant, J. C., "Thermal Panel Report to the Aerothermodynamic/Configurations Working Group Heat Transfer Methodology for Space Shuttle Studies," Sept. 1971.

17. Livett, R. K. and Schadt, G. H., "Aerodynamic Heating Using the Real Properties of Air Behind Shock Waves," Convair Aerospace Engineering Department Report No. ZR-658-024, December 1958.

18. Romig, M. F., "On the Estimation of Compressible Heat Transfer for High Temperature Air," Convair Aerospace Scientific Research Laboratory Memorandum, June 1958.

19. Bertram, M. H., and Henderson, A., Jr., "Recent Hypersonic Studies of Wings and Bodies," ARS Journal, pp 1129-1139, August 1961.

20. Lewis, C. H. and Burgess, E. G. III, "Empirical Equations for the Thermodynamic Properties of Air and Nitrogen to 15,000°K," Arnold Engineering Development Center, AEDC-TR-63-138, July 1963.

21. Eckert, E. R. G., "Survey of Heat Transfer at High Speeds," WADC Technical Report 54-70, 1954.

22. Hansen, C. F., "Approximations for the Thermodynamic and Transport Properties of High Temperature Air," NASA Technical Report R-50, 1959.

23. Schlichting, H., Boundary Layer Theory, McGraw-Hill, New York, 1960.

24. Spalding, D. B. and Chi, S. W., "The Drag of a Compressible Turbulent Boundary Layer on a Smooth Flat Plate With and Without Heat Transfer," Journal of Fluid Mechanics, Vol. 18, Part I, pp 117-143, January 1964.

25. Komar, J. J., "Improved Turbulent Skin-Friction Coefficient Predictions Utilizing the Spalding-Chi Method," Douglas Aircraft Co. Report DAC-59801, Nov. 1966.

26. Bertram, M. H., and Neal, Luther, Jr., "Recent Experiments in Hypersonic Turbulent Boundary Layers," NASA TMX-56335, Presented at the AGARD Specialists' Meeting on Recent Developments in Boundary Layer Research by the Third Dynamics Panel of AGARD, Naples, May 10-14, 1965.

27. Young, C. H., "Investigation of Aerodynamic Heat Transfer to Complex Configurations at Hypersonic Speed," Convair Aerospace Div. of General Dynamics Report GDC-ERR-1677, June 1972.

28. Masek, R. V., "Boundary Layer Transition on Lifting Entry Vehicle Configurations at High Angle of Attack," NASA TMX-52876, Vol. I, 1970.

29. Masaki, M., and Yakura, J., "Transitional Boundary Layer Considerations for the Heating Analyses of Lifting Reentry Vehicles," AIAA Paper No. 68-1155, AIAA Entry Vehicle Systems and Technology Meeting, Williamsburg, Va., December 3-5, 1968.

30. Fay, J. A. and Riddell, F. R., "Stagnation Point Heat Transfer in Dissociated Air," J. Aero. Sci., Vol. 25, pp 73-85, February 1958.

31. Beckwith, I. E., and Gallagher, J. J., "Local Heat Transfer and Recovery Temperatures on a Yawed Cylinder at a Mach Number of 4.15 and High Reynolds Numbers," NASA TR R-104, 1961.

32. Bushnell, D. M., "Effects of Shock-Wave Impingement and Other Factors on Leading-Edge Heat Transfer," NASA TN D-4543, 1968.

33. Lees, L., "Laminar Heat Transfer Over Blunt-Nosed Bodies at Hypersonic Flight Speeds," Jet Propulsion, Vol. 26, pp 259-269, April 1956.

34. Bertram, M. H. and Everhart, P. E., "An Experimental Study of the Pressure and Heat-Transfer Distribution on a 70° Sweep Slab Data Wing in Hypersonic Flow," NASA TR R-153, 1963.

35. Hansen, C. F., and Heims, S. P., "A Review of the Thermodynamic, Transport, and Chemical Reaction Rate Properties of High-Temperature Air," NACA TN 4359, July 1958.

36. Brown, E. H., "The Energy Theorem of Structural Analysis," Engineering, P340 et seq, 18 March 1955.

37. Kaminsky, E. L., Gluck, R., Kaplan, S., and Offenhartz, E., "Structural Requirements for Manned Spacecraft Heat Shield Materials Exposed to Environments Ranging From Deep Space Through Parabolic Earth Engry," AIAA Fifth Annual Structures and Materials Conference, Palm Spring, Ca., April 1-3, 1964.

38. "Long Life High Reliability Thermal Control Systems Study Data Handbook," Space Systems Organization, General Electric Co., Philadelphia, Penn., December 1971.

39. Covington, P. C. and Oglesby, S., Jr., "Measurements of the Thermal Properties of Various Aircraft Structure Materials," WADC TR 57-10. SRI AD 131 032, 1957.

40. Haskins, J. F., "Thermal Conductivity of Plastic Foams From -423°F to 75°F," Report MRG-242, Convair Astronautics, 25 July 1961.

41. Gray, V. H., Gelder, T. F., Cochran, R. P. and Goodykoontz, J. H., "Bonded and Sealed External Insulations for Liquid-Hydrogen-Fueled Rocket Tanks During Atmospheric Flights," Lewis Research Center, NASA TN D-476, October 1960.

42. Urey, Harry Bradford, Jr., "Determination of the Thermal Conductivity of an Aluminum Honeycomb Sandwich Panel," AD 108 261, 1956.